Sequential and coupled inversion of time-lapse borehole GPR measurements for vadose zone model parameterization

Dissertation

zur

Erlangung des Doktorgrades (Dr. rer. nat.)

der

Mathematisch-Naturwissenschaftlichen Fakultät

der

Rheinischen Friedrich-Wilhelms-Universität Bonn

vorgelegt von

Yi Yu

Aus

Hunan, China

Bonn, 06. 2021

Angefertigt mit Genehmigung der Mathematisch-Naturwissenschaftlichen Fakultät der
Rheinischen Friedrich-Wilhelms-Universität Bonn

1. Gutachter: Prof. Dr. Harry Vereecken
2. Gutachter: Prof. Dr. Andreas Kemna
Tag der Promotion: 06.12.2021
Erscheinungsjahr: 2022

ABSTRACT

A profound understanding of the infiltration dynamics into the vadose zone is crucial to our capacity to link surface and subsurface processes for the description of the hydrologic cycle. A key to establish reliable models describing the infiltration process is the knowledge of the soil hydraulic parameters. A promising approach to estimate soil hydraulic parameters is inverse modeling based on dynamic changes in soil water content (SWC). In this context, ground penetrating radar (GPR) has been recognized as a powerful geophysical technique in vadose zone hydrogeophysics, because SWC is strongly related to the soil bulk permittivity that can be precisely determined by GPR. The aim of this thesis is to investigate the feasibility of using time-lapse GPR measurements obtained during infiltration events for vadose zone characterization with a special focus on the estimation of soil hydraulic parameters.

A prerequisite for estimating soil hydraulic parameters based on GPR measurements obtained during infiltration events is that the GPR measurements should reliably reflect the transient SWC dynamics during and after infiltration events. To verify this, a 4-day infiltration experiment was performed at the rhizotron facility in Selhausen, Germany. SWC information at 0.2, 0.4, 0.6, 0.8, and 1.2 m depths were obtained by zero-offset profiling (ZOP) measurements from horizontal borehole GPR. Unfortunately, SWC information for the top 0.1 m of soil obtained by ZOP measurements was not reliable due to the strong interference between direct and refracted waves. To solve this problem, surface GPR measurements were additionally conducted. Dispersive guided waves were observed in the 500 MHz surface GPR data because the infiltration event generated electromagnetic waveguides in the top soil layer. This allowed to obtain SWC information of the top 0.1 m soil layer through dispersion analysis of the dispersive surface GPR data. By combining surface and horizontal borehole GPR measurements, the vertical SWC profiles (0 - 1.2 m) and dynamics were successfully represented during and after infiltration events. Additionally, it was found that the GPR-derived SWC corresponded well with independently measured SWC estimates obtained with time domain reflectometry (TDR) and the known amount of water applied in the infiltration events.

In a next step, the performance of sequential and coupled inversion strategies for estimating hydraulic parameters from horizontal borehole GPR measurements during infiltration events was investigated. For this, a synthetic modelling study was performed first. The sequential inversion was based on measured SWC profiles obtained from the GPR travel times of the direct wave based on the straight-wave approximation and modelled SWC profiles obtained with HYDRUS-

1D. Due to interpretation errors near the infiltration front and the soil surface associated with the straight-wave approximation, the sequential inversion scheme inaccurately estimated the soil hydraulic parameters in the synthetic modelling study. On the other hand, the coupled inversion scheme relied on the measured GPR travel time information and the simulated GPR travel times obtained by coupling HYDRUS-1D with a forward model describing GPR wave propagation (gprMax3D). As the interpretation errors from the straight-wave approximation were avoided, the coupled inversion scheme obtained accurate estimates of the soil hydraulic parameters in the synthetic modelling study. The coupled inversion approach was also applied to the actual horizontal borehole GPR measurements obtained during the 4-day infiltration experiment at the rhizotron facility, where it also provided plausible estimates of the hydraulic parameters.

Finally, a synthetic modelling study was conducted to evaluate the potential advantages and shortcomings of coupled full waveform inversion (CFWI) of horizontal borehole GPR measurements for estimating soil hydraulic parameters and layer thickness for a 2-layer soil profile. Here, CFWI uses the full GPR waveform instead of the first arrival time, which is expected to provide additional information for parameter estimation. The results of the CFWI were compared to the coupled inversion of GPR travel times, as well as sequential inversion using SWCs from GPR travel times. A workflow of the CFWI was proposed and an efficient synthetic infiltration experiment was designed. The results for the synthetic experiment showed that CFWI allowed to accurately estimate layer thickness for a 2-layered soil profile in addition to the soil hydraulic parameters, because CFWI used additional information contained in reflected waves from the layer boundary. Moreover, the hydraulic parameter estimates from the coupled inversion of travel times exhibited a slight deviation from the true values and a relatively larger uncertainty in the hydraulic conductivity and retention functions. In contrast, the soil hydraulic parameters estimated by CFWI showed considerably smaller uncertainty and better matched with the known water retention and hydraulic conductivity curves. However, there are still several remaining challenges for the application of CFWI to measured GPR data. First, an effective approach for source wavelet estimation from measured ZOP data needs to be developed. Second, a sophisticated hydrological model combining the simulations of water flow and solute transport needs to be considered for CFWI to better estimate the electrical conductivity distributions during the infiltration process. Finally, the accuracy and especially the efficiency of the current GPR forward modelling method needs to be improved to enable CFWI for actual GPR data.

In conclusion, the combined use of surface and horizontal borehole GPR measurements was able to provide accurate information on the spatiotemporal SWC variation induced by infiltration. This

allowed the use of sequential and coupled inversion approaches to obtain estimates of soil hydraulic parameters. It was found that coupled inversion outperforms sequential inversion for the estimation of the soil hydraulic parameter from time-lapse horizontal borehole GPR data if strong SWC gradients occurred during the infiltration events. In addition, it was shown that CFWI has several additional advantages over the coupled inversion of GPR travel time data, and thus could become a promising approach for characterizing soil hydraulic properties at the field scale after resolving several remaining challenges.

ZUSAMMENFASSUNG

Ein tiefgreifendes Verständnis über die Infiltrationsdynamik in der ungesättigten Zone ist ausschlaggebend um ober- und unterirdische Prozesse miteinander zu verknüpfen und somit die Prozesse des hydrologischen Kreislaufs zu beschreiben. Ein Schlüssel bei der Erstellung zuverlässiger Modelle zur Beschreibung von Infiltrationsprozessen, ist die Kenntnis der bodenhydraulischen Parameter. Ein vielversprechender Ansatz zur Bestimmung der bodenhydraulischen Parameter ist die inverse Modellierung, die auf dynamischen Änderungen des Bodenwassergehalts (SWC) basiert. In diesem Zusammenhang wird Bodenradar (GPR) als eine vielversprechende geophysikalische Methode in der Hydrogeophysik der ungesättigten Zone angesehen, da der SWC stark mit der dielektrischen Permittivität des Bodens zusammenhängt, die mit GPR präzise bestimmt werden kann. Das Ziel dieser Arbeit ist es, die Anwendbarkeit von GPR während Infiltrationsereignissen und die Charakterisierung der ungesättigten Zone zu testen. Ein besonderer Fokus liegt hierbei auf der Abschätzung der bodenhydraulischen Parameter.

Eine Voraussetzung für die Bestimmung bodenhydraulischer Parameter anhand von GPR-Messungen während Infiltrationsereignissen, ist die korrekte Darstellung der instationären SWC-Dynamik während und nach der Infiltrationsereignisse. Um dieses zu überprüfen, wurde ein viertägiges Infiltrationsexperiment auf der Rhizotron-Anlage in Selhausen, Deutschland, durchgeführt. SWC-Informationen in 0,2, 0,4, 0,6, 0,8 und 1,2 m Tiefe wurden durch Zero-Offset-Profiling (ZOP)-Messungen in horizontalen Bohrlöchern gewonnen. Leider waren die SWC Informationen, die durch die ZOP-Messungen in den obersten 0,1 m des Bodens aufgenommen wurden, aufgrund der starken Interferenz zwischen direkten und gebrochenen elektromagnetischen Wellen nicht zuverlässig. Um dieses Problem zu lösen, wurden zusätzliche Oberflächen-GPR-Messungen durchgeführt. Dispers geführte Wellen wurden anhand der 500 MHz Oberflächen-GPR-Daten beobachtet, da das Infiltrationsereignis elektromagnetische Wellenleiter in der obersten Bodenschicht generierten. Dies ermöglichte es, durch eine Dispersionsanalyse der Oberflächen-GPR-Daten SWC Informationen über die oberste 0,1 m mächtige Bodenschicht zu erhalten. Durch die Kombination von Oberflächen- und horizontalen Bohrloch-GPR-Messungen konnten die vertikalen SWC-Profile (0 - 1,2 m) und die Dynamik während und nach den Infiltrationsereignissen erfolgreich abgebildet werden. Darüber hinaus wurde festgestellt, dass die von GPR abgeleiteten SWC gut mit unabhängig gemessenen SWC Schätzungen übereinstimmten, die mit Zeitbereichsreflektometrie (TDR) und der bekannten Wassermenge, die bei den Infiltrationsereignissen aufgebracht wurde, ermittelt wurden.

Im nächsten Schritt wurde die Leistungsfähigkeit von sequentiellen und gekoppelten

Inversionsstrategien zur Abschätzung der hydraulischen Parameter aus horizontalen Bohrloch-GPR-Messungen während Infiltrationsereignissen untersucht. Hierfür wurde zunächst eine synthetische Modellstudie durchgeführt. Die sequentielle Inversion basierte dabei auf gemessenen SWC Profilen, die aus den GPR-Laufzeiten der direkten Welle basierend auf der Geradwellenapproximation gewonnen wurden, und modellierten SWC-Profilen die mit HYDRUS-1D generiert wurden. Aufgrund von Interpretationsfehlern in der Nähe der Infiltrationsfront und der Bodenoberfläche im Zusammenhang mit der Geradwellenapproximation schätzte das sequentielle Inversionsschema die bodenhydraulischen Parameter in der synthetischen Modellstudie ungenau. Andererseits stützte sich das gekoppelte Inversionsschema auf die gemessenen GPR-Laufzeitinformationen und die simulierten GPR-Laufzeiten, die durch die Kopplung mit HYDRUS-1D zur Beschreibung der GPR-Wellenausbreitung (gprMax3D) generiert wurden. Da dadurch die Interpretationsfehler aus der Geradwellenapproximation vermieden wurden, zeigte das gekoppelte Inversionsschema genauere Schätzungen der bodenhydraulischen Parameter in der synthetischen Modellstudie. Der gekoppelte Inversionsansatz wurde auch auf die tatsächlichen horizontalen Bohrloch-GPR-Messungen angewandt. die während des viertägigen Infiltrationsexperiments auf der Rhizotron-Anlage gewonnen wurden, wo dieser Ansatz ebenfalls zu plausible Schätzungen der hydraulischen Parameter führte.

Schließlich wurde eine synthetische Modellstudie durchgeführt, um die potenziellen Vor- und Nachteile der gekoppelten Volle-Wellenform-Inversion (CFWI) von horizontalen Bohrloch-GPR-Messungen zur Schätzung der bodenhydraulischen Parameter und der Schichtdicke für ein zweischichtiges Bodenprofil zu bewerten. Hierbei verwendet die CFWI die vollständige GPR-Wellenform anstelle lediglich der ersten Ankunftszeit, was zusätzliche Informationen für die Parameterschätzung liefern sollte. Die Ergebnisse der CFWI wurden mit der gekoppelten Inversion von GPR-Laufzeiten sowie der sequentiellen Inversion mit SWCs aus GPR-Laufzeiten verglichen. Ein Arbeitsablauf der CFWI wurde vorgeschlagen und ein effizientes synthetisches Infiltrationsexperiment entworfen. Die Ergebnisse für das synthetische Experiment zeigten, dass CFWI zusätzlich zu den bodenhydraulischen Parametern eine genaue Schätzung der Schichtdicke für ein zweischichtiges Bodenprofil ermöglichte, da die CFWI zusätzliche Informationen verwendete, die in reflektierten Wellen von der Schichtgrenze enthalten waren. Darüber hinaus wiesen die hydraulischen Parameterschätzungen aus der gekoppelten Inversion der Laufzeiten eine leichte Abweichung von den wahren Werten und eine verhältnismäßig höhere Unsicherheit bei den hydraulischen Leitfähigkeits- und Retentionskurven auf. Im Gegensatz dazu zeigten die durch CFWI geschätzten bodenhydraulischen Parameter eine wesentlich geringere Unsicherheit

und stimmten besser mit den bekannten Wasserretentions- und hydraulischen Leitfähigkeitskurven überein. Allerdings gibt es noch einige verbleibende Herausforderungen für die Anwendung von CFWI für gemessene GPR-Daten. Erstens muss ein effektiver Ansatz für die Bestimmung des Quellsignals aus gemessenen ZOP-Daten entwickelt werden. Zweitens muss ein anspruchsvolles hydrologisches Modell, das die Simulationen des Wasser- und des Stofftransports kombiniert für CFWI in Betracht gezogen werden, um die Verteilungen der elektrischen Leitfähigkeit während des Infiltrationsprozesses besser abzuschätzen. Schließlich muss die Genauigkeit und insbesondere die Effizienz der aktuellen GPR-Vorwärtsmodellierungsmethode verbessert werden, um CFWI für aktuelle GPR-Daten zu ermöglichen.

Zusammenfassend lässt sich sagen, dass die kombinierte Verwendung von Oberflächen- und horizontalen Bohrloch-GPR-Messungen in der Lage war, genaue Informationen über die raumzeitliche SWC-Variation zu bestimmen, die durch Infiltration induziert wird. Dies ermöglichte die Verwendung von sequentiellen und gekoppelten Inversionsansätzen, um Schätzungen der bodenhydraulischen Parameter zu erhalten. Es wurde festgestellt, dass die gekoppelte Inversion die sequenzielle Inversion für die Schätzung der bodenhydraulischen Parameter aus horizontalen Bohrloch-GPR-Daten im Zeitraffer übertrifft, wenn starke SWC-Gradienten während der Infiltrationsereignisse auftraten. Darüber hinaus wurde gezeigt, dass CFWI mehrere zusätzliche Vorteile gegenüber der gekoppelten Inversion von GPR-Laufzeitdaten hat und somit, nach dem Lösen einige verbleibende Herausforderungen, ein vielversprechender Ansatz für die Charakterisierung der bodenhydraulischen Eigenschaften auf der Feldskala werden könnte

CONTENT

LIST OF FIGURES

LIST OF TABLES

LIST OF ACRONYMS

CCE	Competitive complex evolution algorithm
CFWI	Coupled full waveform inversion
CMP	Common midpoint
COP	Common offset profiling
CRIM	Complex refractive index model
CRNP	Cosmic-ray neutron probe
DC	Direct current
DREAM	Differential evolution adaptive metropolis algorithm
EM	Electromagnetic
EMI	Electromagnetic induction
ERT	Electrical resistivity tomography
FDTD	Finite-difference time-domain method
FWI	Full waveform inversion
GPR	Ground penetrating radar
HMO	Hyperbolic move-out
JSC	Jülich Supercomputing Centre
LMO	Linear move-out
MOG	Multi-offset gathers
MvG	Mualem - van Genuchten model
NIC	Neumann Institute for Computing
PML	Perfectly matched layers
REV	Representative elementary volume
RMSE	Root-mean-square error
SCE-UA	Shuffled complex revolution algorithm
SWC	Soil water content
TE	Transverse electric mode
TDR	Time domain reflectometry
TDT	Time domain transmission sensors
WARR	Wide angle reflection and refraction
ZOP	Zero-offset profiling

LIST OF SYMBOLS

A	Correlation matrix	/
c	Speed of light in vacuum	m ns^{-1}
C_m	Cost function for dispersion analysis	m ns^{-1}
C_v	Covariance matrix	/
$C_{MVG}(E)$	Cost function for coupled full waveform inversion	V m^{-1}
$C_{MVG}(t)$	Cost function for coupled inversion of travel time	ns
$C_{MVG}(\theta)$	Cost function for sequential inversion	cm^3 cm^{-3}
E^{mod}	Simulated waveform	V m^{-1}
E^{obs}	Measured waveform	V m^{-1}
e	Natural logarithm	-
d	Distance between the two boreholes	m
f	Center frequency of the antenna	MHz
h	Pressure head	cm
h_t	Layer thickness	m
I	Electric current density	A m^{-2}
J	Jacobian matrix	/
K_r	Hydraulic conductivity	cm min^{-1}
K_s	Saturated hydraulic conductivity	cm min^{-1}
k_a	Tortuosity constant	-
l	Empirical pore-connectivity parameter	-
m	Empirical model parameter related to n	-
m^{est}	Estimated hydraulic parameters	/
m^{inv}	Parameters for the inversion	/
m_a	Cementation exponent	-
m_f	Mode of the guided wave	-
N	Multivariate normal distribution	/
n	Pore-size distribution index	-
n_a	Saturation exponent	-
n_e	Number of the electric field points	-
n_f	Number of picked frequency points	-
n_m	Number of GPR measurements	-
R^2	Coefficient of determination	-

R_x	Receiver	/
S	Sink term	$cm^3\ cm^{-3} min^{-1}$
S_e	Effective saturation	-
S_d	Distance between transmitter and receiver	m
s_v^2	Error variance matrix	/
T	Time	min or h
T_p	Temperature	°C
T_s	Excitation moment	ns
T_x	Transmitter	/
T_0	Time-zero offset	ns
TE_0	Fundamental mode	/
TE_1	First higher mode	/
TE_2	Second higher mode	/
t	Travel time	ns
t^{mod}	Simulated first arrival time	ns
t^{obs}	Measured first arrival time	ns
v	Velocity	$m\ ns^{-1}$
v_{data}	Measured phase velocity of the guided wave	$m\ ns^{-1}$
v_{Gw}	Velocity of the ground wave	$m\ ns^{-1}$
v_{model}	Theoretical phase velocity of the guided wave	$m\ ns^{-1}$
Z_G	Sampling depth of the ground wave	m
z	Positive upward spatial coordinate	cm
α	Related to the inverse of the air-entry pressure	cm^{-1}
ΔE	Noise level of waveform data	$V\ m^{-1}$
Δt	Noise level of travel time data	ns
$\Delta\theta$	Noise level of soil water content data	$cm^3\ cm^{-3}$
ε	Bulk dielectric permittivity	-
ε_1	Dielectric pemittivity of the wet layer	-
ε_2	Dielectric pemittivity of the underlying material	-
ε^{mod}	Simulated dielectric permittivity	-
ε^{obs}	Observed dielectric permittivity	-
ε_s	Dielectric permittivity of soil particles	-
ε_w	Dielectric permittivity of water	-
θ	Volumetric soil water content	$cm^3\ cm^{-3}$

θ^{obs}	Obtained water content	$cm^3\ cm^{-3}$
θ^{mod}	Simulated soil water content	$cm^3\ cm^{-3}$
θ_m	Fundamental equation of modal theory	rad
θ_r	Residual soil water content	$cm^3\ cm^{-3}$
θ_s	Saturated soil water content	$cm^3\ cm^{-3}$
λ	Characteristic length	m
σ	Soil electrical conductivity	$S\ m^{-1}$
σ^{mod}	Simulated electrical conductivity	$S\ m^{-1}$
σ_w	Water electrical conductivity	$S\ m^{-1}$
Φ	Porosity	$cm^3\ cm^{-3}$

CHAPTER 1 GENERAL INTRODUCTION

1.1 Research background

Water is one of the most important natural resources for the survival and development of human civilization. Although there is a large amount of water on Earth, only ~2.5% is fresh water (Oki and Kanae, 2006) that can be cheaply and directly used in our daily life for drinking, sanitation, and production purposes. Ground water makes up 30% of total fresh water or 95% of unfrozen fresh water (Gleick, 1993), which implies that it plays a central part in enabling human adaptation and maintaining ecosystems (Taylor et al., 2013). The vadose zone is the unsaturated portion that lies between the land surface and the ground water table. It controls the exchange and distribution of water and energy flux at the land surface (Vereecken et al., 2008). With the rapidly growing global population, the sustainable use of ground water resources has become a critical issue (Singh, 2014), and therefore, scientifically-based management of ground water resources and effective remediation of ground water contamination are increasingly demanded. To achieve these goals, a key point is to estimate the soil hydraulic parameters of the vadose zone, which can be used to inform state-of-the-art hydrological models for simulating water flow and contaminant transport for the areas of interest (Jhorar et al., 2009; Singh, 2010; Zhu et al., 2013).

Soil hydraulic properties can be determined by various laboratory methods (e.g., Hsieh et al., 1981; Neuzil et al., 1981; Tamari et al., 1993), which are in general tedious and time-consuming. Additionally, hydraulic properties estimated from laboratory methods typically represent a relatively small volume, which may poorly represent the soil characteristics at the field scale (Kool et al., 1987) because the variation of natural soil conditions (e.g., soil texture and structure, bulk density, or soil organic carbon content) generates considerable spatiotemporal variability of the soil hydraulic properties. This scale effect can be further illustrated by using the concept of the representative elementary volume (REV) (Bear, 1972; Chen and Wagenet, 1992). Hereby, the REV indicates a volume that is representative to a certain extent if the soil state does not vary substantially with a change of scale (Wessel-Bothe and Weihermüller, 2020). Possible relations between a soil property and the characteristic length are shown in Fig. 1.1. For a continuous hierarchy and in the transition zones of a discrete hierarchy, soil properties obtained from laboratory methods and point sensors that have small REV will be not representative for the next larger scale (e.g., the field scale). Moreover, it is likely that sample preparation and the operation of the laboratory experiment introduce additional uncertainty in the hydraulic parameters

(Sonnleitner et al., 2003). Hence, field-scale estimation of soil hydraulic properties is preferred for establishing a realistic hydrological model.

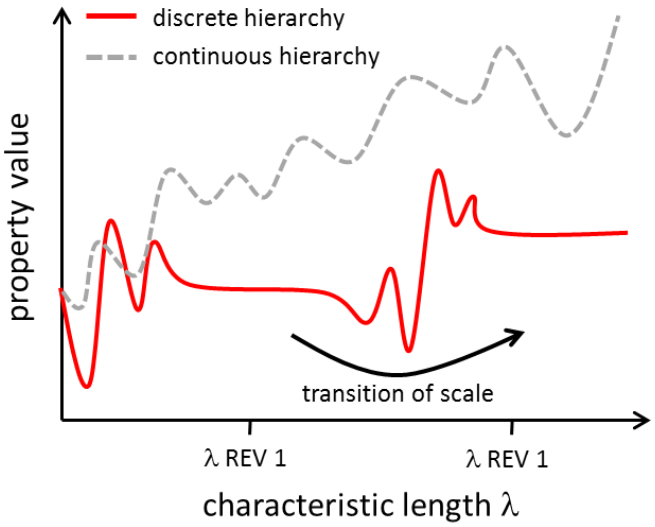

Fig. 1.1 The dependency of a soil property on characteristic length for two different types of spatial heterogeneity (adapted from Zurmühl (1994)).

For the estimation of the saturated hydraulic conductivity of soil, infiltration experiments performed by ring infiltrometers (single ring and double ring) (e.g., Bagarello and Sgroi, 2004; Fatehnia et al., 2016; Lai and Ren, 2007; Verbist et al., 2010; Youngs, 1987) and tension-disc infiltrometers (e.g., Angulo-Jaramillo et al., 2000; Šimůnek et al., 1998) have been widely used, since the infiltration rate of water into the soils is strongly related to the soil hydraulic conductivity. Generally, single ring infiltrometers can efficiently measure the saturated hydraulic conductivity (e.g., Di Prima, 2016; Prieksat et al., 1992). Due to the lateral water flow below the ring, the rate of infiltrated water determined using a single ring overestimates the saturated hydraulic conductivity (Wessel-Bothe and Weihermüller, 2020). Sophisticated modelling approaches are needed to obtain more accurate estimates of the saturated hydraulic conductivity from such experiments (e.g., Verbist et al., 2013). To prevent lateral water flow, double ring infiltrometers were introduced and recognized as an economical technique for conducting soil infiltration experiments. A disadvantage of both single ring and double ring infiltrometers is that the saturated hydraulic conductivity in soils having macropores (e.g., wormholes and cracks) may be overestimated (Yolcubal et al., 2004), because a large amount of ponded water may infiltrate through these macropores. Tension-disc infiltrometers measure both unsaturated and (near-)saturated hydraulic conductivity at a negative pressure. Compared to ring infiltrometers, tension-disc infiltrometers require less water and cause less disturbance of the soil surface while

avoiding the influence of macropores (Yolcubal et al., 2004). A challenge with tension-disc infiltrometer measurements is the need for a completely flat surface. This can be solved by using contact materials between the soil surface and the infiltrometer (e.g., Reynolds and Zebchuk, 1996). On the other hand, such a contact layer may introduce flow impedance effects and therefore result in the underestimation of the hydraulic conductivity, especially at high infiltration rates (Reynolds et al., 2000).

Classical infiltration experiments are useful to estimate the saturated hydraulic conductivity or the unsaturated hydraulic conductivity at a predefined pressure head. Nevertheless, they cannot provide information about the soil water retention characteristics (e.g., the pore-size distribution). To estimate water retention characteristics, either soil matric potential or soil water content (SWC) measurements can be used in combination with an inversion scheme (e.g., Ritter et al., 2003; Šimůnek and van Genuchten, 1996). SWC measurements have several advantages over soil matric potential measurements to estimate soil hydraulic parameters (Vereecken et al., 2008). First of all, SWC measurements are commonly non-or/minimally invasive and can be conducted at different scale with high temporal and spatial resolution, while soil matric potential can only be measured at the point-scale. In addition, soil matric potential is not easy to measure accurately and the measurement range and/or resolution over the entire pressure head range is limited. Therefore, SWC measurements are often preferred for characterizing soil hydraulic properties (e.g., Angulo-Jaramillo et al., 1996; Malicki et al., 1992).

1.2 SWC determination with point sensors

Conventional SWC measurements are performed with point sensors, such as the neutron probe (Chanasyk and Naeth, 1996), time domain reflectometry (TDR) (Topp et al., 1980), capacitance sensors (Dean et al., 1987), or time domain transmission sensors (TDT) (Blonquist Jr. et al., 2005). The neutron probe is a classical nuclear technique that estimates the SWC by measuring the thermal or slow neutron density (Schmugge et al., 1980). With access tubes, SWC can be determined as a function of depth. TDR determines the relative dielectric permittivity of the soil from the propagation velocity of an electromagnetic wave determined from the travel time along a sensor with a known length. Using the strong relationship between bulk permittivity and SWC (e.g., Topp et al., 1980; Roth et al., 1990), TDR allows accurate SWC measurements. In addition, TDR allows to measure SWC and bulk electrical conductivity simultaneously (e.g., Dalton et al., 1984; Noborio, 2001; Yu and Drnevich, 2004; Zegelin et al., 1989). As cheaper alternatives to TDR, capacitance and TDT sensors measure SWC with lower accuracy. TDR, capacitance and TDT sensors have been widely utilized in hydrology and soil science for flexible measurements

of SWC, such as monitoring of liquid movements (e.g., Cataldo et al., 2007; Paltineanu and Starr, 2000; Topp and Davis, 1981) and revealing SWC variation during the infiltration (e.g., Blonquist Jr. et al., 2006; Greco, 2006). Moreover, SWC sensors have been used to build sensor networks for long-term SWC measurements at the field scale (e.g., Bogena et al., 2007; Bogena et al., 2010; Qu et al., 2013; Weihermüller et al., 2013). A key disadvantage of all point sensors, and especially of most capacitance and TDT sensors is the relatively small sensing volume that results in poor spatial representativeness.

1.3 SWC determination with geophysical methods

In the last decades, geophysical techniques, such as electrical resistivity tomography (ERT), ground penetrating radar (GPR), electromagnetic induction (EMI), and the cosmic-ray neutron probe (CRNP) have been rapidly developed and widely used for SWC determination. ERT and EMI provide the apparent electrical conductivity of the subsurface, which is a weighted average of the soil bulk electrical conductivity with depth (Corwin and Scudiero, 2020). Since the soil bulk conductivity depends on SWC (e.g., Archie, 1942; Rhoades et al., 1976), apparent electrical conductivity measurements from ERT or EMI can potentially be used to estimate SWC. In particular, ERT is a well-established technique to monitor 2D/3D SWC dynamics with a high resolution (e.g., Beff et al., 2013; Brunet et al., 2010, Jouen et al., 2008; Kemna et al., 2002). Another advantage of ERT is the relatively large investigation depth (0 ~ 10 m) (e.g., Chambers et al., 2014). EMI has advantages with respect to mobility and efficiency, and allows rapid SWC estimation of larger areas up to a scale of ~ 1 km^2 (e.g., Altdorff et al., 2017). Unfortunately, ERT and EMI are also sensitive to several other confounding factors such as clay content and pore water salinity (Klotzsche et al., 2019a), which makes SWC estimation complicated. CRNP is a novel technique that estimates SWC by measuring the fast neutron flux near the soil surface, using the fact that the count of near-surface fast neutrons is negatively correlated with SWC (Zreda et al., 2008). The most attractive advantage of CRNP is the relatively large measurement volume. The horizontal footprint of CRNP is related to the air density and has an approximate radius of 130 – 240 m at sea level (Köhli et al., 2015). A clear disadvantage of CRNP is that the method is not only sensitive to the water contained in the soil but to all hydrogen in the footprint (e.g., lattice water, atmospheric water vapor, snow cover, and water in and on vegetation) (Zreda et al., 2012). In addition, a further critical point is that the measurement depth of CRNP is strongly related to SWC (Zreda et al., 2008). For wet soils, the measurement depth is shallow and limited to ~0.12 m (Franz et al., 2013).

GPR is a non-invasive method that uses high frequency (10 ~ 2500 MHz) electromagnetic (EM) waves to investigate soils and deeper geological features (Daniels, 2005). To conduct GPR measurements, EM signals are emitted by transmitter antenna and are then propagating through the subsurface and will be finally received by receiver antenna as a function of time. After processing these signals, the bulk dielectric permittivity ε (-) (related to the velocity of EM waves) and soil electrical conductivity σ (S m^{-1}) (related to the attenuation of the EM wave) can be estimated. A major advantage of GPR compared to ERT and EMI is the strong relationship soil bulk permittivity and SWC that is relatively independent of confounding factors (Huisman et al., 2003a; Klotzsche et al., 2018; Liu et al., 2019). Furthermore, GPR also has a good mobility and allows rapid investigations of larger scales with profiles up to 1000 m length (e.g., Mahmoudzadeh Ardekani, 2013). With the help of borehole tubes, GPR can measure the SWC at deep depths with a very high resolution (e.g., Alumbaugh et al., 2002). Therefore, GPR is a popular technique for providing high-resolution subsurface characterization and addressing water-related problems at different scales (e.g., Cao et al., 2020; Grote et al., 2010; Lambot et al., 2004). The most common GPR measurement strategies include surface GPR, off-ground GPR, and borehole GPR, which will be reviewed in the following section.

1.4 SWC determination with GPR

1.4.1 SWC determination with surface GPR

Surface GPR is the most widely-used GPR configuration. In this configuration, the transmitter and receiver antennas (e.g., Beres Jr. and Haeni, 1991; Kaufmann et al., 2020) are in full contact with the soil surface. To perform a successful surface GPR survey, a compromise between resolution and depth penetration should be found, because the resolution of the GPR improves with increasing antenna center frequency but high frequency GPR signals exhibit stronger attenuation, and thus, have limited penetration depth, especially in high-conductivity soils (Huisman et al., 2003a). Therefore, it is important to have at least a rough knowledge of the soil texture at the measurement location to properly select the GPR antennas to be used.

Surface GPR waves propagate along different paths in the soil. In order to determine the velocity and attenuation of these waves, several data acquisition strategies can be employed (Davis and Annan, 1989), such as common offset profiling (COP) (Fig. 1.2a), wide angle reflection and refraction (WARR) (Fig. 1.2b), and common midpoint (CMP) (Fig. 1.2c) measurements. COP measurements are carried out by moving the transmitter and receiver with a fixed spacing. Data processing approaches developed for seismic data, such as the semblance method for velocity

analysis (Yilmaz, 2001) and migration (e.g., Fisher et al., 1992) can also be used for GPR. For COP data, many GPR data analysis programs provide workflows to interactively extract GPR wave velocity by manually fitting a hyperbola to the hyperbolic reflection of scattering objects (Fig. 1.2d). COP measurements are commonly used for mapping soil layering (e.g, Dal Bo et al., 2019) or detecting buried targets (e.g, Liu et al., 2018; Porsani et al., 2012). However, they are not widely used for SWC determination because the calculation of the radar velocity to obtain the dielectric permittivity for SWC estimation requires the presence of scattering objects or knowledge of the layer depth (Huisman et al., 2003a).

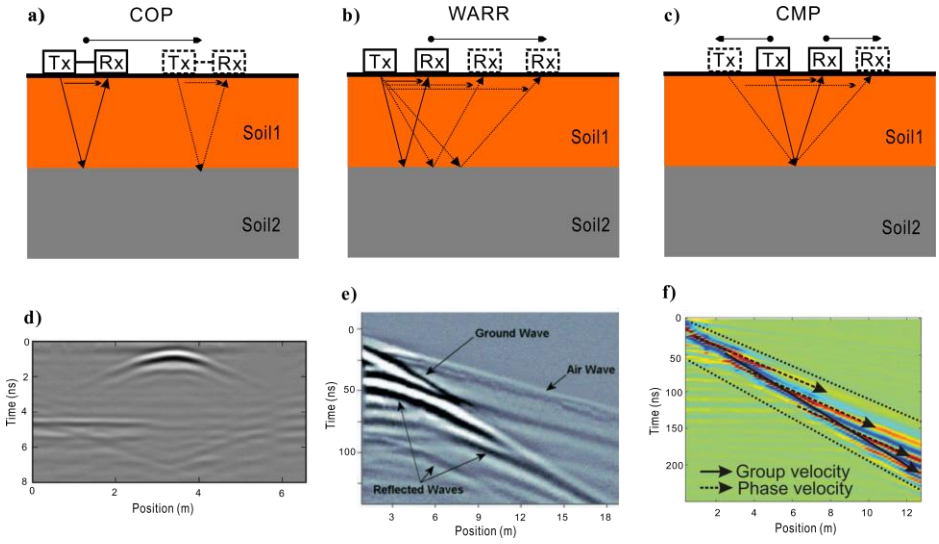

Fig. 1.2 Schematic illustration of (a) common offset profiling (COP), (b) wide angle reflection and refraction (WARR), and (c) common midpoint (CMP) measurements. (d) Typical measured COP data for pipe detection. The hyperbola indicates the reflection of a steel pipe (modified version from Wiwatrojanagul et al., 2017). (e) Typical measured CMP data showing different types of GPR waves (modified version from Huisman et al., 2003a). (f) Typical measured CMP data showing dispersion characteristics associated with guided waves (adapted from van der Kruk et al., 2009a).

WARR measurements are conducted by fixing the transmitter at one position and moving the receiver with fixed steps. In CMP measurements, the transmitter and receiver antennas are moved simultaneously with a fixed spacing in different direction, while keeping a common mid-point. The air wave, ground wave, and reflected wave are typical wave paths that can easily be identified in WARR and CMP data (Fig. 1.2e). The air wave propagates directly from transmitter to the receiver through the air. It can thus be recognized as a straight line in WARR and CMP data with a slope that is equal to the speed of light (0.3 m ns^{-1}). Given the known travel time, the air wave

is commonly employed to determine the beginning of the effective signal (zero time) for GPR data (Grote et al., 2005). SWC can be accurately estimated from WARR/CMP measurements by using the velocity of ground waves, reflected waves, and guided waves. The ground wave directly travels from transmitter to receiver through the shallow subsurface, and thus, shows potential to obtain SWC of the shallow subsurface. Huisman et al. (2001) investigated the use of the ground wave for SWC determination. In this case, 25 WARR measurements were conducted and the SWC was estimated from the velocity of the ground waves and compared to SWC estimates obtained with TDR. It was found that the accuracy of SWC determination from GPR ground waves ($\pm$ 0.03 cm^3 cm^{-3}) was comparable with that of the TDR measurements. As the ground wave can be easily recognized in CMP/WARR data even in the absence of soil layering, the ground wave method has been widely used to estimate and map shallow SWC (e.g., Algeo et al., 2016; Huisman et al., 2002; van Overmeeren et al.,1997; Weihermüller et al., 2007). However, a major disadvantage of the ground wave method is that the sampling volume of the estimated SWC cannot be precisely obtained, because the penetrating depth of the ground wave can only be estimated empirically (e.g., Grote et al., 2010, van Overmeeren et al., 1997).

As an alternative, SWC can also be estimated from the velocity of reflected waves if a reflecting soil layer exists in the subsurface. The reflected wave in CMP/WARR data is hyperbolic-shaped (Fig. 1.2e). The velocity of reflected waves in CMP/WARR data can be obtained by semblance analysis or fitting a hyperbola. Reflected waves provide estimates of the average SWC to the depth of the reflecting layer (e.g., Lunt et al., 2005; Mangel et al., 2012; Mangel et al., 2020). For soils with multiple reflecting layers (e.g., Grote et al., 2005), the SWC of each layer can be estimated from the interval velocity of the different layers obtained by solving Dix's equation (Dix, 1955). As in the case of COP measurements, SWC determination from reflected waves relies on the presence of reflectors in the subsurface, which are likely to vary over time and across space. Therefore, the measurement resolution of the reflection method cannot be controlled. Moreover, the reflected wave has a relatively weak amplitude compared to other waves, and thus, is more sensitive to noise and interference from other waves.

In situations where the subsurface shows pronounced layering, such as ice overlying unfrozen soil (e.g., Arcone, 1984), a guided wave can be generated in a waveguide layer. In particular, this commonly occurs if the layer thickness is similar or smaller than the radar wavelength (van der Kruk et al., 2006a). As in the case of Rayleigh or Love waves in seismic data, guided waves obtained by GPR are characterized by dispersion due to differences between the group and phase velocities (Fig. 1.2f). In this case, traditional ground wave and reflection methods cannot be

employed for SWC determination. Instead, waveguide properties such as the permittivity of waveguide layer, permittivity below this layer, and the waveguide thickness can be estimated by inverting the phase velocity of the guided wave (dispersion analysis) (e.g., Mangel et al., 2015;van der Kruk et al., 2009b; van der Kruk et al., 2010). A specific case for the application of dispersion analysis is to monitor water dynamics during infiltration (Cassiani et al., 2009; Mangel et al., 2017), since this is commonly associated with a transition from wet to dry soil that can serve as the waveguide boundary. Although, guided waves allow to estimate SWC within the waveguide as well as the thickness of the waveguide, the SWC estimates below the waveguide are rather inaccurate, especially when the waveguide layer shows strong vertical heterogeneity (Strobbia and Cassiani, 2007) or in the case of noisy GPR data (Bikowski et al., 2012).

1.4.2 SWC determination with off-ground GPR

Off-ground GPR is measured by using one or more antennas at a given height above the ground surface. The antennas are commonly mounted on a vehicle (e.g., Lambot et al., 2004), drone (Wu et al., 2019), or helicopter (Bradford et al., 2010) to provide mobility. Both monostatic and bistatic radar systems can be employed for off-ground GPR data collection (e.g., Rutishauser et al., 2016). In the first off-ground GPR applications, a time-domain approach to estimate SWC from the reflection coefficient of the ground surface was used (e.g., Redman et al., 2002; Serbin and Or, 2005). However, this approach assumes that the soil material is uniform and lossless (Lambot et al., 2006a; Leng and Al-Qadi, 2014), and thus may lead to inaccurate SWC determination if the soil surface is not smooth or if SWC varies with depth (Huisman et al., 2003a). Lambot et al. (2004) proposed a new integrated frequency-domain approach based on the use of an ultrawide band stepped frequency continuous wave radar combined with a dielectric filled transverse electric and magnetic horn antenna and full waveform inversion. This method can be employed for estimating a depth dependent SWC profile (Lambot et al., 2006a) and is suitable for mapping SWC distribution at larger scales. Nevertheless, this method is still prone to the influence of surface roughness, which can be theoretically corrected (e.g., Jonard et al., 2012) if the roughness is known from independent measurements or if independent SWC are available to estimate the correction term. For both time-domain and full waveform inversion approaches to interpret off-ground GPR measurements, the signal (backscatter) is impacted by the vegetation, which also has to be accounted for (e.g., Mahmoudzadeh Ardekani et al., 2016).

1.4.3 SWC determination with borehole GPR

Off-ground and surface GPR are less suitable for obtaining SWC information from deep soil

horizons (Klotzsche et al., 2018) because strong reflectors (e.g., soil – air interface or bedrock) and highly conductive soil (e.g., clay or saline soils) impede the transmission of radar energy. A feasible approach to overcome this limitation is to measure GPR in vertical or horizontal boreholes (borehole GPR). Generally, borehole GPR measurements can be conducted by using zero-offset profiling (ZOP) or multi-offset gathers (MOG). In the case of ZOP measurements (Fig. 1.3a), the transmitter and receiver are moved simultaneously with the same step size in two different boreholes to obtain 1D profile information between the boreholes. Classically, velocity estimates and thus the SWC obtained with ZOP measurements is based on the straight-wave approximation. After determining the first arrival time of the direct wave propagating between the boreholes, depth-dependent velocity estimates can be obtained using the known borehole distance. ZOP measurements are promising for monitoring SWC within the subsurface, but the coexistence of multiple travel paths can result in inaccurate SWC estimates (Rucker and Ferré, 2004a). For example, interference of the critically refracted air wave and the direct wave occurs at shallow borehole depths (Klotzsche et al., 2019a). Several recent studies have used ZOP GPR measurements between horizontal boreholes to monitor seasonal depth-dependent SWC variations (Cai et al., 2016; Klotzsche et al., 2019a). Due to the good control on vertical resolution and the improved field representativeness, this type of set up can provide detailed information to reveal the spatial and temporal variation of SWC.

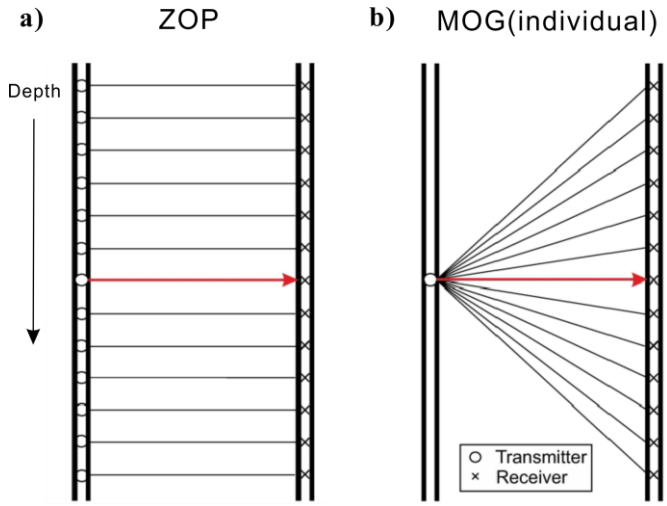

Fig. 1.3 Schematic diagrams for (a) ZOP and (b) MOG measurements (adapted from Klotzsche et al., 2019b).

MOG measurements (Fig. 1.3b) have been used to obtain a 2D SWC distribution between the boreholes (e.g., Binley et al., 2001). MOG measurements are conducted by fixing the transmitter in a borehole at different depths, while moving the receiver down or up with a constant spacing

in other boreholes. The traditional procedure for inverting MOG data is based on geometrical ray theory (Peterson, 2001). MOG measurements can map 2D or even 3D SWC distribution with a high resolution but are associated with long acquisition times. Therefore, MOG measurements are promising for imaging steady-state water distributions but are less suitable for monitoring dynamic SWC variations caused by e.g., rapid infiltration.

With the increase of computation power, GPR data processing strategies have advanced in the past decade. In particular, the development of the full waveform inversion (FWI) has allowed improved interpretation of both surface and borehole GPR measurements. Instead of only extracting the velocity information from GPR data, as in the case of traditional ray-based methods, FWI takes the entire GPR waveform into consideration. Hence, it theoretically allows the mapping of the SWC distribution in the subsurface with a higher resolution (Klotzsche et al., 2018). For surface and off-ground GPR, FWI approaches are mainly reported to characterize layered soils (e.g., Busch et al., 2012; Lambot and Andre, 2014; Minet et al., 2011). For vertical borehole GPR, FWI has become a well-established technique to obtain high resolution subsurface images (e.g., Gueting et al., 2017; Klotzsche et al., 2014; Meles et al., 2010). In the case of horizontal borehole GPR measurement, only a few studies with FWI have been reported. A preliminary study is presented by Klotzsche et al. (2016) about using FWI to obtain ε and σ for a 2-layer soil profile with horizontal borehole GPR data.

1.5 Hydrological model parameterization

1.5.1 Unsaturated water flow in porous media

Reliable predictions of water flow in the vadose zone are the prerequisite for water resources management and effective contaminant remediation. The 1D unsaturated water flow in porous media can be described by the Richards equation:

$$\frac{\partial \theta(h)}{\partial T} = \frac{\partial}{\partial z}\left[K_r(h)\left(\frac{\partial h}{\partial z} + 1\right)\right] - S \tag{1.1}$$

where $\theta(h)$ is the water retention function that describes the relationship between the volumetric SWC (θ) ($cm^3\,cm^{-3}$) and the pressure head (h) (cm) , T is time (min), z represents the positive upward spatial coordinate (cm), and K_r is the hydraulic conductivity ($cm\,min^{-1}$) as a function of h. The sink term S ($cm^3\,cm^{-3}\,min^{-1}$) is the volume of water removed from a unit volume of soil due to root water uptake. The soil water retention function ($\theta(h)$) and the hydraulic conductivity function ($K_r(h)$) are crucial properties to assess soil water fluxes (Vereecken et al., 2008). These

two functions are often parameterized by using the Mualem - van Genuchten (MvG) model (Mualem, 1976; van Genuchten, 1980) as:

$$\theta(h) = \begin{cases} \theta_r + \frac{\theta_s - \theta_r}{(1+|\alpha h|^n)^m} & , h < 0 \\ \theta_s & , h \geq 0 \end{cases} \quad (1.2)$$

$$K_r(h) = K_s S_e^l [1 - (1 - S_e^{1/m})^m]^2 \quad (1.3)$$

$$S_e = \frac{\theta - \theta_r}{\theta_s - \theta_r} \quad (1.4)$$

where, θ_r and θ_s are the residual and saturated SWC ($cm^3\ cm^{-3}$), respectively. α (cm^{-1}) is related to the inverse of the air-entry pressure. n (-) is the pore-size distribution index, and m (-) is related to n by $m = 1 - \frac{1}{n}$. l (-) is the empirical pore-connectivity parameter (tortuosity) commonly set to 0.5 (van Genuchten, 1980) but can also be estimated for individual soils (Schaap and Leij, 2000), K_s ($cm\ min^{-1}$) is the saturated hydraulic conductivity and S_e (-) is the effective saturation.

HYDRUS-1D (Šimůnek et al., 2008) is a widely used finite-element model to numerically simulate water flow in the vadose zone. Since HYDRUS-1D is in the public domain and can be downloaded freely, it has been widely employed in a range of agriculture applications (Šimůnek et al., 2016), including studying root water uptake process (e.g., Cai et al., 2018a) and modelling contaminant transport (e.g., Wehrhan et al., 2007). HYDRUS-1D has also been used in combination with geophysical data in order to determine the MvG parameters (e.g., Busch et al., 2013; Moghadas et al., 2013) using different inversion strategies.

1.5.2 Inversion strategies for combining hydrological models and geophysical data

Since geophysical measurements cannot directly provide SWC information, sequential (uncoupled) inversion and coupled inversion approaches have been used for hydrological model parameterization with geophysical data (Hinnell et al., 2010; Huisman et al., 2010). Sequential inversion generally consists of three steps. First, geophysical data (e.g., GPR data) are inverted to obtain the geophysical properties (e.g., ε and σ) throughout the subsurface of the region of interest. Next, a petrophysical relationship (e.g., Topp et al., 1980) is adopted to obtain the spatiotemporal distribution of hydrologic states (e.g., SWC) from measured geophysical properties. Finally, the obtained hydrologic states are used to parameterize a hydrological model by inverse modelling. Sequential inversion is an efficient approach that can directly use geophysical data to parameterize hydrological models. Many studies have used a sequential inversion approach to estimate hydraulic parameters from GPR data (e.g., Cassiani et al., 2009; Chen et al., 2004; Looms et al.,

2008a). However, a major disadvantage of the sequential inversion approach is that the interpretation errors that occur during the data processing and the uncertainties related to parameter resolution and uniqueness are propagated into the hydraulic parameter estimation through the petrophysical relation. Due to the propagation of such interpretation errors, sequential inversion is likely to provide erroneous hydraulic parameters.

To improve hydrologic model parameter estimation, coupled inversion has been proposed. In this approach, the output of the hydrological model (e.g., SWC) is used to obtain the simulated geophysical data (e.g., GPR travel times or waveforms). Hence, the measured geophysical data do not have to be processed to obtain the SWC and the optimization is directly carried out between measured and simulated geophysical data. Coupled inversion thus avoids the propagation of interpretation errors and parameter uncertainty related to the data resolution. However, it requires a good hydrological model conceptualization and is associated with significantly higher computational costs. In the last decade, coupled inversion of GPR data has increasingly been used to parameterize hydrological models (e.g., Jadoon et al., 2012; Jonard et al., 2015). An early example for the estimation of field-scale hydraulic parameters through coupled inversion of GPR data was presented by Kowalsky et al. (2005). In this case, a heterogeneous distribution of hydraulic conductivity was estimated using coupled inversion of time-lapse borehole GPR data. In conclusion, coupled inversion is expected to be a more reliable approach for estimating soil hydraulic parameters from geophysical data compared to the more widely used sequential inversion approach.

It is anticipated that a combination of full waveform and coupled inversion will further increase the information content of GPR measurements, and thus reduce uncertainty in the estimated hydraulic parameters. However, there are only a few studies that combined coupled and full waveform inversion (CFWI) for hydrological parameterization. Lambot et al. (2009) used coupled FWI of time-lapse off-ground GPR data to estimate the soil hydraulic parameters during an infiltration experiment. Li et al. (2020) presented a series of synthetic modelling studies that showed how coupled FWI of time-lapse seismic data can be used to obtain the 2D distribution of the saturated hydraulic conductivity. In future studies, CFWI needs to get more attentions and the advantages of CFWI need to be recognized by more synthetic or actual case studies.

1.6 Objectives and outline

The overall aim of this thesis is to investigate the use of GPR for vadose zone characterization with a particular focus on the determination of soil hydraulic properties from time-lapse GPR data measured during infiltration events. Especially, I intend to use this thesis to explore the advantages of coupled inversion since the coupled inversion approach is still not well recognized and widely used. To achieve this overall aim, the thesis is divided in three parts that have their own specific aim.

The first part (Chapter 2) aims to evaluate the feasibility of using surface and horizontal borehole GPR data to reveal the transient dynamics of soil water distribution during an infiltration experiment conducted at a minirhizotron facility in Selhausen, Germany. In particular, SWC variations at 0.2, 0.4, 0.6, 0.8, and 1.2 m depth are estimated using ZOP measurements with horizontal borehole GPR. In addition, dispersion analysis of guided waves is employed to determine the SWC for the top 0.1 m soil. By combining the complementary borehole and surface GPR data, representative vertical SWC profiles (0 –1.2 m depth) are obtained before, during, and after the infiltration events. Finally, the SWC profiles obtained by GPR will be compared with the known water storage changes during the infiltration experiment. A good correspondence would indicate that the measured GPR data are useful for characterizing the properties of the vadose zone.

The second part (Chapter 3) aims to compare the performance of sequential and coupled inversion strategies for estimating hydraulic parameters from horizontal borehole GPR travel time data. In a first step, the differences between sequential and coupled inversion for GPR travel times will be systematically studied using a synthetic infiltration event based on the actual experiment introduced in Chapter 2. Synthetic SWC data and GPR data will be obtained and the correlations between different pairs of hydraulic parameters will be revealed based on the synthetic data. Next, sequential and coupled inversion will be applied to the synthetic data and their results will be compared to determine which inversion scheme is more suitable for inverting measured GPR data. Finally, an appropriate inversion approach will be used to invert the actual GPR measurements, and the inversely estimated soil hydraulic properties will be compared with independent hydraulic parameters estimated by other methods to assess the reliability of the inversion. In addition, the uncertainty of the inverted soil hydraulic parameters will be quantified.

The third part (Chapter 4) aims to investigate potential benefits and shortcomings of a coupled

full-waveform inversion (CFWI) for estimating soil hydraulic parameters and layer thickness for a 2-layer profile using synthetic horizontal borehole GPR data. For this, synthetic SWC, GPR travel time and waveform data will be obtained and the correlations between the layer thickness and hydraulic parameters will be analyzed for the inversions with different types of data. Next, CFWI will be performed with synthetic data to estimate the hydraulic parameters and layer thickness for a 2-layer model. The estimated parameters and their uncertainty will be compared with those obtained from the standard coupled inversion of GPR travel time data. Finally, the limitations of CFWI will be discussed and solutions to improve the CFWI will be proposed.

The conclusions of this thesis as well as the prospects for future research will be summarized in Chapter 5.

CHAPTER 2 MEASURING VERTICAL SOIL WATER CONTENT PROFILES BY COMBINING HORIZONTAL BOREHOLE AND DISPERSIVE SURFACE GROUND PENETRATING RADAR DATA[1]

Abstract

To investigate transient dynamics of soil water redistribution during infiltration, horizontal borehole and surface ground penetrating radar (GPR) measurements were conducted during a 4-day infiltration experiment at the rhizontron facility in Selhausen, Germany. Zero-offset GPR profiling (ZOP) in horizontal boreholes was used to obtain soil water content (SWC) information at specific depths (0.2, 0.4, 0.6, 0.8, and 1.2 m). However, horizontal borehole GPR measurements do not provide accurate SWC estimates of the top soil (0 – 0.1 m depth) because of interference between direct and critically refracted waves. Therefore, surface GPR data were additionally acquired to estimate SWC of the top soil. Due to the generation of electromagnetic waveguides in the top soil caused by infiltration, a strong dispersion in the GPR data was observed in 500 MHz surface GPR data. A dispersion inversion was thus performed with these surface GPR data to obtain SWC information for the top 0.1 m of the soil. By combining the complementary borehole and surface GPR data, vertical SWC profiles were obtained, which were used to investigate vertical soil water redistribution. Reasonable consistency was found between the GPR results and independent SWC data derived from time domain reflectometry (TDR) measurements. Because of the improved spatial representativeness of the GPR measurements, the SWC profiles obtained by GPR better matched the known water storage changes during the infiltration experiment. It was concluded that the combined use of borehole and surface GPR data convincingly revealed spatiotemporal SWC variation during infiltration. In addition, this setup allowed a better quantification of water storage, which is a prerequisite for future applications, where for example the soil hydraulic properties will be estimated from GPR data.

[1] Adapted from Yu, Y., Klotzsche, A., Weihermüller, L., Huisman, J.A., Vanderborght, J., Vereecken, H., van der Kruk, J., 2020. Measuring vertical soil water content profiles by combining horizontal borehole and dispersive surface ground penetrating radar data. Near Surf. Geophys. 18(3): 275-294. doi:10.1002/nsg.12099.

2.1 Introduction

Characterizing soil water content (SWC) dynamics in unsaturated soil is important for a range of applications, including monitoring of pollutant transport (e.g., Binley et al., 2001), investigating root and plant growth processes (e.g., Cai et al., 2018b), and estimating subsurface hydrogeological properties (e.g., Knight, 2001). GPR is a popular hydrogeophysical method to investigate SWC dynamics because of its potentially high spatial resolution (Binley et al., 2015; Huisman et al., 2003b; Slob et al., 2010) and the direct relationship between SWC and dielectric permittivity, which in turn determines the propagation of electromagnetic waves between GPR antennas. Over the last years, GPR has been widely used for investigating spatial SWC variability, monitoring SWC variations, and estimating soil hydraulic properties (e.g., Allroggen et al., 2015; Busch et al., 2013; Galagedara et al., 2002; Huisman et al., 2001; Huisman et al., 2002; Iwasaki et al., 2016; Jadoon et al., 2012; Jaumann and Roth, 2018; Klotzsche et al., 2018; Pan et al., 2012; Redman et al., 2000; Steelman et al., 2012; van Overmeeren et al., 1997).

GPR measurements can be conducted by using antennas placed at the surface or in boreholes. Surface GPR measurements have been used to obtain high-resolution SWC information using different acquisition strategies. A range of studies have shown that the ground wave that travels directly from the transmitter to the receiver through the top soil has potential for spatial mapping of SWC (Galagedara et al., 2005a; Huisman et al., 2003a; Weihermüller et al., 2007). Due to the unclear penetration depth of the ground wave (Galagedara, et al., 2005b; Grote et al., 2010), it is, however, not possible to determine vertical SWC profiles from this type of GPR measurements. Multi-offset reflection methods have also been used to estimate SWC in both field-scale (Lunt et al., 2005) and lab-scale studies on SWC dynamics (Mangel et al., 2012). However, the energy of reflected waves is often relatively weak and can thus be easily distorted by other radiated energy, which may lead to biased SWC estimates, especially in the case of heterogeneous permittivity distributions commonly associated with infiltration events. In addition, there is only limited control on the vertical resolution of SWC measurements obtained with the reflection method, because it depends on the position of the reflectors in the soil (Huisman et al., 2003a). Therefore, conventional ground wave and reflection methods are not well suited to obtain high-resolution vertical SWC profiles by using GPR.

Borehole GPR can provide high resolution geophysical information of the shallow subsurface, and this approach has been used to characterize soil properties for many years (e.g., Dafflon et al., 2011; Doetsch et al., 2010; Holliger et al., 2001; Klotzsche et al., 2013; Yang et al., 2013). Zero-

offset profiling (ZOP) is a widely-used acquisition strategy for borehole GPR measurements (e.g., Rejiba et al., 2011), in which the transmitting and receiving antenna are moved simultaneously with a fixed step size in two different boreholes. Standard ray-based analysis methods can then be used to obtain a 1D velocity profile between the two boreholes. Recently, several time-lapse plot-scale studies focused on SWC variation using horizontal borehole GPR measurements at specific depths, which ensures a good control on the vertical resolution of the obtained SWC profile information (Cai et al., 2016; Klotzsche et al., 2019a). These studies mainly investigated seasonal SWC variations for different soils, surface treatments and the influence of plant types. It was found that the horizontal borehole GPR measurements did not provide accurate information close to the soil surface (0 – 10 cm) because of interference between the critically refracted air wave and the direct wave (Klotzsche et al., 2019a). This is obviously problematic when investigating infiltration processes, because the top soil is the most dynamic area with the strongest SWC changes. One possibility to overcome this limitation is to combine horizontal borehole and surface GPR measurements.

It has been observed that increased near-surface SWC associated with infiltration leads to low-velocity waveguides (van der Kruk et al., 2006a). In such waveguides, total reflection of the GPR waves occurs on the boundary between the wet and dry soil, which generates a guided wave through the constructive interference of the critical reflections and the ground wave causing late-arrival high-amplitude events in the data (Arcone et al., 2003). Such guided waves show a pronounced dispersion in multi-offset surface GPR data, and thus a frequency-dependent velocity where phase velocities are different from the group velocity (van der Kruk et al., 2009a). Dedicated analysis methods are required to obtain relevant information from guided waves. In a first step, a phase velocity spectrum is calculated (Park et al., 1998) and the strongest energy in the spectrum is used to determine the phase velocity of different frequencies. With this frequency-dependent phase velocity, single-layer (van der Kruk et al., 2006a), multi-layer (van der Kruk et al., 2010), or piece-wise linear models (Mangel et al., 2015) can be used to determine waveguide properties (e.g., permittivity, layer thickness) using model inversion. For example, single-layer waveguide inversion has been used to obtain the average dielectric permittivity and thickness of the waveguide during infiltration (Cassiani et al., 2009, Rossi et al., 2015). Using a piece-wise linear model in the waveguide inversion, it is also possible to obtain a continuous and smooth SWC profile that may be more appropriate to describe the actual vertical distribution of SWC during and after infiltration events (Mangel et al., 2017).

Until now, no study has been conducted that combines surface GPR with horizontal borehole GPR to study soil water content changes. Therefore, the aim of this chapter is to evaluate the accuracy and consistency of combined surface and horizontal borehole GPR results obtained during a dynamic infiltration experiment. In order to achieve this aim, transient SWC changes up to a depth of 1.2 m were monitored during a well-controlled infiltration experiment using ZOP surveys in horizontal boreholes. In addition, surface GPR measurements were conducted to characterize infiltration-induced waveguides in order to obtain SWC of the upper 0.1 m of soil. As a reference for the GPR results, Time domain reflectometry (TDR) measurements were recorded at the same depths of the horizontal boreholes during the infiltration experiment. To assess the accuracy of the GPR and TDR results, the measured increase in water storage of these two methods was compared with the known irrigation amount used in the infiltration experiment.

2.2 Method and material

2.2.1 Infiltration experiment

The infiltration experiment was performed at the upper terrace minirhizotron facility in Selhausen, Germany (Cai et al., 2016; Kelter et al., 2018). The facility is divided into three plots (3 × 7 m) with different water treatments (natural rain, rain-out shelter, and irrigated). Horizontal rhizotubes and soil sensors can be accessed via an access trench on one side of the facility (Fig. 2.1). Rhizotubes of 7 m length were installed at 0.1, 0.2. 0.4, 0.6, 0.8, and 1.2 m depths across the field with a horizontal offset of 0.1 m between tubes at different depth levels (see Fig. 2.1b and 2.1d). Here, it has to be noted, that the installation of the boreholes was done after excavating the entire plot up to a depth of 1.5 m as undisturbed installation of the boreholes using a drilling device into the stony native soil was not feasible. After excavation, the soil was refilled layer-wise and the boreholes (and other sensors) were installed during this backfilling. After completion of the facility, horizontal borehole GPR measurement could be carried out from the access trench by putting transmitter and receiver antennas into two neighboring (rhizo-) tubes at the same depth (Fig. 2.1b).

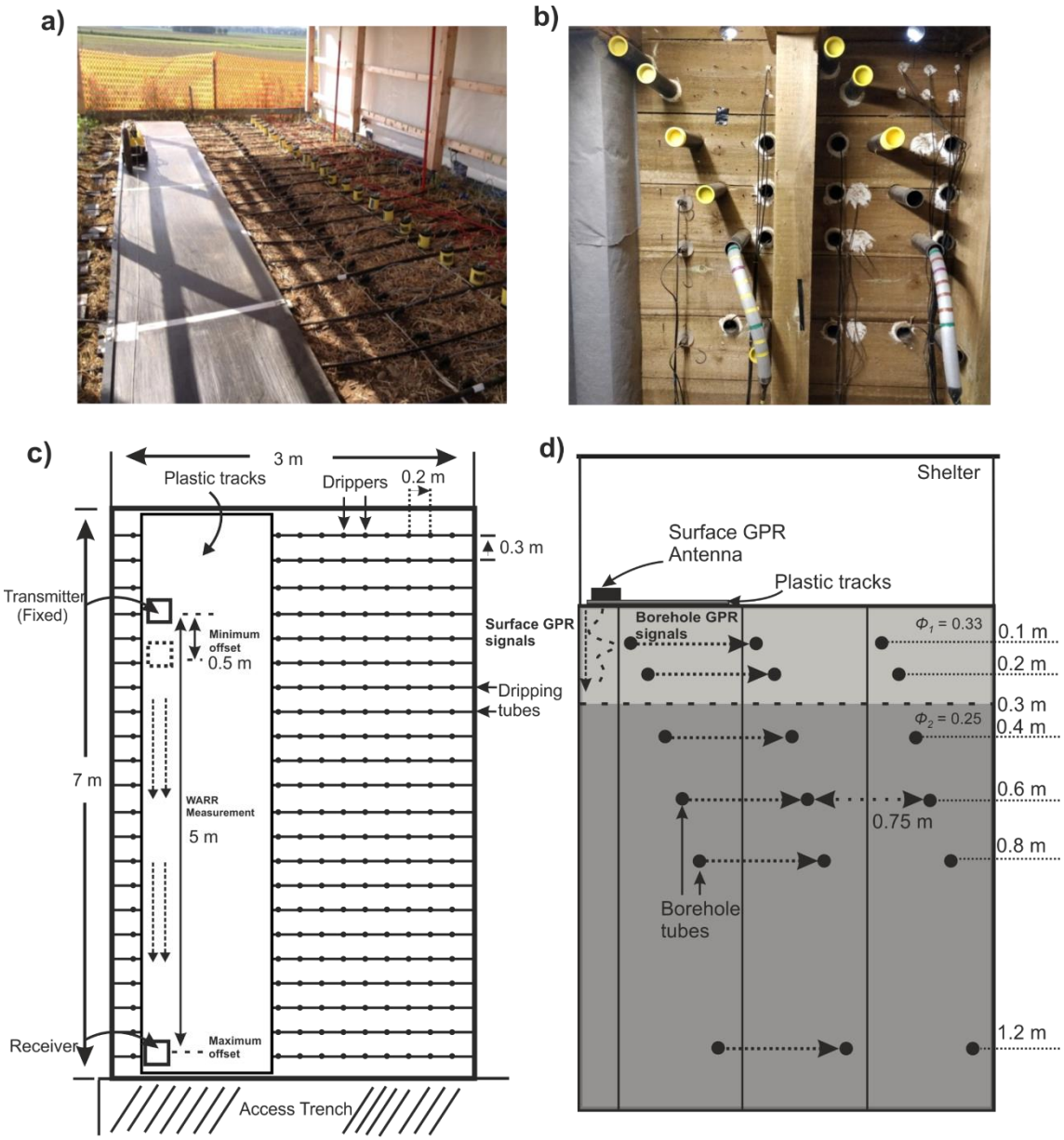

Fig. 2.1 (a) Photo of the set-up of the infiltration experiment (surface), and (b) horizontal boreholes used for GPR measurements and location of the TDR sensors. (c) Schematic setup of the drip irrigation system at the soil surface and (d) sketch of the entire acquisition set-up with surface GPR and horizontal borehole tubes.

TDR measurements were made hourly by using a TDR100 system connected to a CR3000 data logger (both Campbell Scientific, Logan, USA) and the 50C81-SDM multiplexer as described by Weihermüller et al. (2013). Custom-made three-rod TDR sensors with a rod length of 200 mm and a spacing of 26 mm were installed 0.75 m away from the facility wall into the soil at the same depths as the tubes used for GPR measurements. Stones and gravel larger than 60 mm were removed around the location of the TDR sensors during installation. For more details on the

construction of the minirhizotron facility and the installed sensors, I refer to Cai et al. (2016).

The infiltration experiment was conducted in the sheltered plot (Fig. 2.1a) using a drip irrigation system (Fig. 2.1c). The plot was completely sheltered several weeks before the start of the experiment to ensure dry initial soil conditions. The distance between two neighboring dripping tubes was 0.30 m and the distance between the drippers was 0.20 m. To ensure irrigation at a constant rate, water was first poured into an underground water tank and then pumped out from that to supply the drip irrigation system. The water volume was recorded by a flow meter between the water pump and the drip irrigation system.

Five infiltration events were performed between the 30th of September 2013 and the 3rd of October 2013 (Table 2.1). Horizontal borehole and surface GPR measurements were taken using a PulseEKKO system (Sensors & Software, Canada) during the first 4 days of the infiltration experiment. For the borehole measurements, 200 MHz dipole antennas were used and for the surface measurements unshielded 100 and 200 MHz as well as shielded 500 MHz antennas were used.

Table 2.1 Overview of infiltration events during the infiltration experiment

Date	Start time	End time	Water volume ($L\ m^{-2}$)	T_p (°C)	σ_w ($S\ m^{-1}$)
30/09/2013	14:54	16:24	28.4	17.0	0.0513
01/10/2013	12:24	13:54	27.3	17.0	0.0513
02/10/2013	12:45	14:15	28.0	16.0	0.0500
03/10/2013	12:24	13:54	26.1	14.4	0.0488
03/10/2013	14:28	15:58	27.0	14.4	0.0488

Although the saturated hydraulic conductivity (K_s = 0.057 cm min^{-1}; Cai et al., 2018a) of the topsoil is much larger than the average irrigation rate (0.03 cm min^{-1}), ponding at the soil surface was observed on the first day of the experiment. Ponding was not observed anymore during the following infiltration events. Before, during, and after the daily infiltration events, ZOP GPR measurements were performed in the horizontal borehole pairs. As the SWC is assumed to increase mainly at shallow depths at the beginning of each consecutive infiltration event, only the horizontal boreholes at 0.2 and 0.4 m depth were measured during the infiltration event to ensure that all measurements could be performed within the irrigation interval. After the irrigation stopped, the deeper boreholes were also measured. Additionally, more than 140 wide angle reflection and refraction (WARR) measurements were obtained with surface GPR during the infiltration experiment (see Fig. 2.1c for setup).

2.2.2 Horizontal borehole GPR data acquisition and processing

For the ZOP measurements, I followed the same acquisition, processing and analysis strategies as presented in Klotzsche et al. (2019a). To conduct the ZOP survey, the transmitter (T_x) and receiver (R_x) antenna were first pushed to the end of the horizontal boreholes (7 m) at the same depth. Then, both antennas were pulled simultaneously in 0.05 m steps towards the access trench wall up to a minimum distance of 1.5 m to the wall. Using the recorded travel time t (ns) and the known distance between the two boreholes (d = 0.75 m), the velocity of the radar wave v (m ns^{-1}) can be determined using:

$$v = \frac{d}{t - T_0} \tag{2.1}$$

where, T_0 (ns) is the so-called time-zero offset (Fig. 2.2a). Different with the case for surface GPR measurements, the determination of T_0 is difficult for borehole GPR measurements because no air wave is present, Therefore, T_0 was determined from multi-offset measurements with the borehole antennas in air (hereafter referred to as calibration WARR measurements). An accurate determination of T_0 is important because the pulse onset time can drift during the GPR survey and relatively small changes in T_0 can easily introduce substantial velocity changes and thus erroneous SWC estimates (Peterson, 2001), in particular in the case of the small borehole separations used here. In order to determine T_0, the following procedure was used. In a first step, the first maximum and zero-crossing of each trace in the calibration WARR measurement (inset of Fig. 2.2b) is determined automatically. Then, a constant time difference between the actually needed first arrival time and first zero-crossing is determined for a certain number of traces by manual time picking. This constant time offset is different for the calibration measurement and the ZOP data due to the different center frequencies. The first arrival of each GPR trace is then obtained by subtracting the constant time difference from the zero-crossing times for all traces. Finally, T_0 is determined as the intercept of a line with a fixed slope (1/0.3 m ns^{-1}) fitted to the first arrival times.

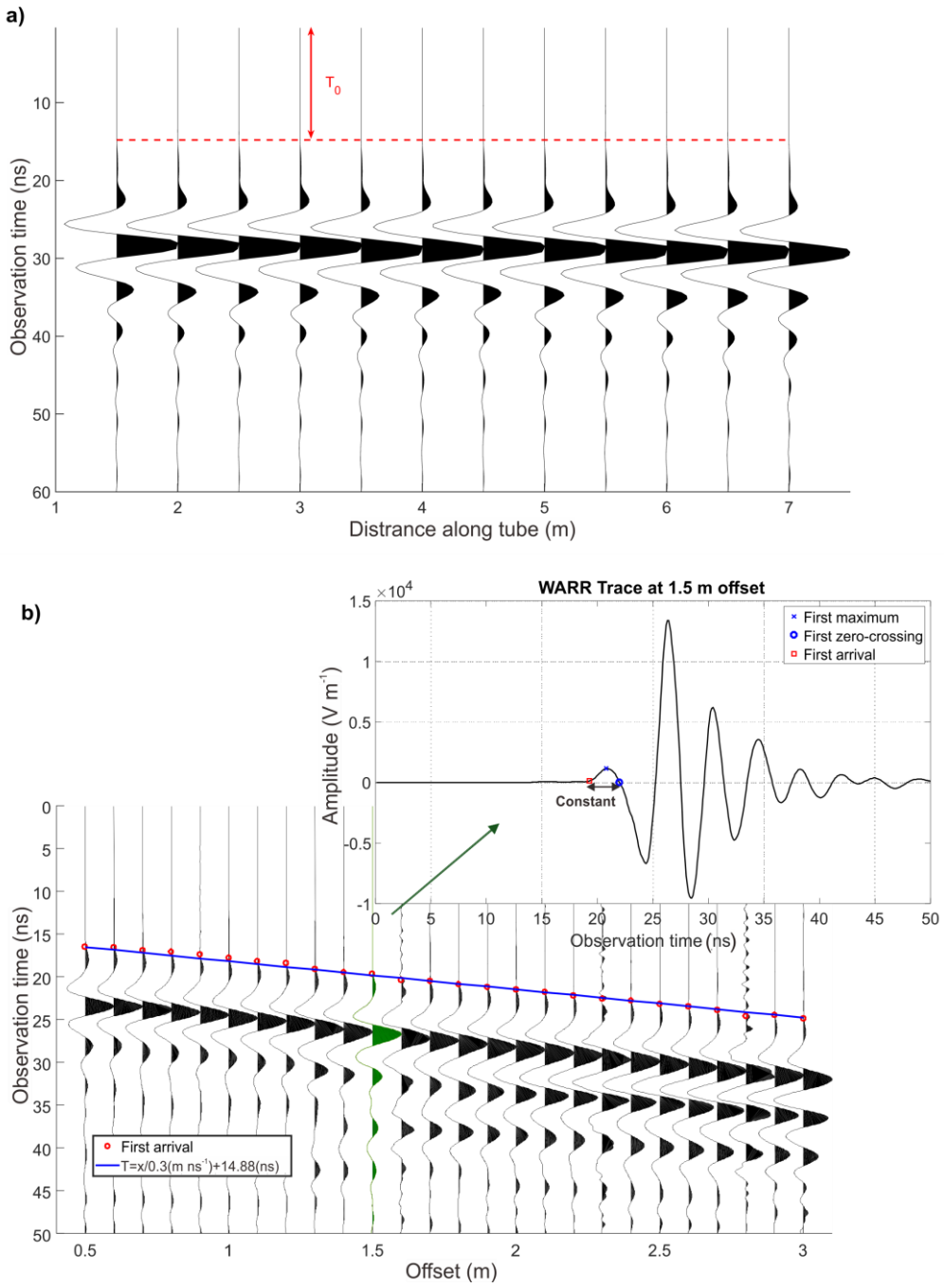

Fig. 2.2 (a) Typical 200 MHz ZOP data for horizontal borehole GPR. The appropriate T_0 is determined from a WARR measurement in air. (b) Illustration of T_0 estimation from a WARR measurement with 200 MHz antenna. The first arrival time of all traces are indicated by red dots. T_0 is the intercept of the regression line for the first arrival of the air wave as a function of antenna offset (blue line). The inset illustrates the determination of the time difference between the first arrival (red dot) and the first zero-crossing (blue dot).

In order to account for drifts in T_0, calibration WARR measurements were made regularly in between ZOP measurements. Drift in T_0 as a function of time was observed and the most appropriate value for T_0 at the time of each ZOP measurement was determined by linear interpolation between calibration measurements. After the determination of v for each ZOP measurement using Eq. 2.1, the measured dielectric permittivity ε^{obs} (-) at different depths was obtained by:

$$\varepsilon^{obs} = \left(\frac{c}{v}\right)^2 \tag{2.2}$$

where c is the speed of light in vacuum (0.3 m ns^{-1}).

2.2.3 Surface GPR data acquisition and processing

Surface GPR measurements were made on a plastic track to prevent contact between the antenna and the irrigation water as well as to protect the soil from being damaged by the operators of the surface GPR system. The offset range of the surface WARR measurement was from 0.5 to 5.0 m (see Table 2.2 for acquisition parameters). Firstly, the T_0 of the data surface GPR data is calibrated as the intercept of a line that determined by a fixed slope (1/0.3 m ns^{-1}) and the picked first arrival time of air wave at 0.5 m offset. A combined linear move-out (LMO) and hyperbolic move-out (HMO) semblance analysis approach (Dal Bo et al., 2019) was used to analyze the 100 and 200 MHz data. These GPR measurements did not show velocity dispersion associated with infiltration because the wavelength at these frequencies is much larger than the thickness of the wetted top soil layer. The velocity of the direct ground wave was extracted by LMO. HMO was used to estimate the velocity of the reflected wave. An empirical function (Grote et al., 2003; van Overmeeren et al., 1997) was employed to estimate the sampling depth Z_G (m) of the ground wave:

$$Z_G = \frac{1}{2}\sqrt{\frac{v_{Gw}S_d}{f}} \tag{2.3}$$

where, v_{Gw} (m ns^{-1}) is the velocity of the ground wave, S_d (m) is the distance between transmitter and receiver, and f (MHz) is the center frequency of the antenna. Based on this relationship, it can be seen that sampling depth decreases with increasing frequency and SWC (Grote et al., 2010).

Table 2.2 Overview of data acquisition of surface GPR

Frequency (MHz)	Sampling interval (m)	Time window (ns)	Sampling rate (ns)	Stack (-)
100	0.05	100	0.4	32
200	0.05	200	0.4	32
500	0.01	50	0.2	32

After the first infiltration event, the WARR measurements made with the 500 MHz antenna showed dispersive waves. The following procedure was used to process these dispersive data. In a first step, the air wave was muted and the guided wave (Fig. 2.3a) was selected to generate a phase-velocity spectrum (Fig. 2.3c, 2.3d). Next, the phase velocity for different frequencies $v_{data}(f_i)$ (m ns^{-1}) was obtained by picking the maximum energy for each frequency in the phase velocity spectrum (black line, Fig. 2.3d). The center frequency of the measured data (350 MHz, Fig. 2.3b) is commonly less than that of the GPR antenna (500 MHz) and it can be observed from the amplitude spectrum (Fig. 2.3b) that the effective bandwidth is approximately between 200 and 700 MHz when using a threshold of 15% of the maximum amplitude. This bandwidth is used in the following analysis of the frequency-dependent phase velocity.

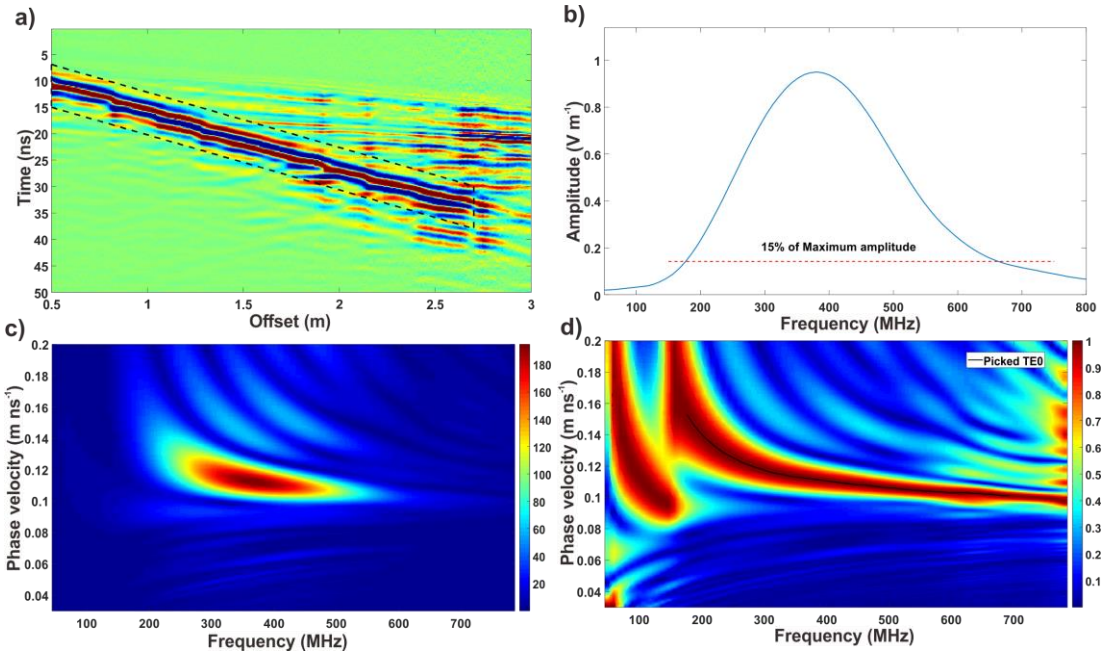

Fig. 2.3 (a) Dispersive surface GPR dataset measured at the end of the first infiltration event using 500 MHz antenna. Dashed lines indicated the zone used for the dispersion analysis. (b) Average frequency spectrum (normalized) of the GPR data. (c) Phase velocity spectrum before and (d) after normalization.

Single-layer low-velocity waveguide inversion was employed to invert the dispersive surface GPR data to obtain the thickness h_t (m), average permittivity of the wet layer ε_1(-), and the underlying material ε_2 (-). For this, the theoretical phase velocity $v_{model}(f_i, \varepsilon_1, \varepsilon_2, h_t)$ (m ns^{-1}) was calculated by solving the equation established by the given waveguide parameters $(\varepsilon_1, \varepsilon_2, h_t)$:

$$v_{model}(f_i, \varepsilon_1, \varepsilon_2, h_t) = \frac{c}{\sqrt{\varepsilon_1}\sin[\theta_m(f_i, \varepsilon_1, \varepsilon_2, h_t)]} \quad (2.4)$$

where $\theta_m(f_i, \varepsilon_1, \varepsilon_2, h_t)$ (rad) is the fundamental equation of modal theory (Arcone, 1984). Since the surface GPR measurements were conducted in the transverse electric (TE) mode, the fundamental modes (TE_0) and higher modes (TE_1, TE_2, etc.) of the guided wave can be present in the data, if the signals contain frequencies above the respective cutoff frequency (van der Kruk, 2006b). The dispersion inversion of fundamental mode and higher modes was performed through minimization of a cost function $C_m(\varepsilon_1, \varepsilon_2, h_t)$ (m ns^{-1}) based on the absolute difference between $v_{model}^{\mathrm{TE}_{mf}}(f_i, \varepsilon_1, \varepsilon_2, h)$ and $v_{data}^{\mathrm{TE}_{mf}}(f_i)$ (van der Kruk et al., 2006a):

$$C_m(\varepsilon_1, \varepsilon_2, h_t) = \sum_{i=1}^{nf} \frac{\left| v_{data}^{\mathrm{TE}_{m_f}}(f_i) - v_{model}^{\mathrm{TE}_{m_f}}(f_i, \varepsilon_1, \varepsilon_2, h_t) \right|}{n_f} \tag{2.5}$$

where n_f (-) refers to the number of frequency points picked in the phase velocity spectrum and m_f represents the mode of the guided wave. The inversion for single layer waveguide parameters is very sensitive to ε_1 and partly to h_t (Strobbia and Cassiani, 2007), whereas the inverted ε_2 are typically not accurate. The uncertainty in the inversion of $\varepsilon_2$is caused by simplifying the vertical SWC distribution to a single layer waveguide and the stronger measurement noise in the low-frequency part of the phase velocity spectrum (below 200 MHz) (Bikowski et al., 2012).

2.2.4 Determination of soil water content and storage

The complex refractive index model (CRIM) (Roth et al., 1990) was used to relate the dielectric permittivity obtained with GPR and TDR to SWC θ (cm^3 cm^{-3}) according to the following equation:

$$\theta = \frac{\sqrt{\varepsilon} - (1-\Phi)\sqrt{\varepsilon_s} - \Phi}{\sqrt{\varepsilon_w} - 1} \tag{2.6}$$

where, ε_w (-) refers to the permittivity of water (84 at 10°C). The permittivity of the soil particles ε_s (-) was considered to be 4.7 for this test site, as suggested by Klotzsche et al. (2019a) and Robinson et al. (2005). It is important to notice that porosity Φ changed from 0.33 to 0.25 (cm^3 cm^{-3}) at 0.3 m depth due to the presence of a plowing horizon (Fig. 2.1).

To verify the accuracy of the SWC estimates obtained by GPR and TDR, cumulative water storage (m) was calculated by integrating the measured SWC over the entire profile depth. The increase in water storage was then compared with the known irrigation amounts (Table 2.1). In the integration, it was assumed that the surface GPR measurements and the TDR measurements at 0.1 m depth represent the average SWC of the 0 - 0.1 m depth range. Furthermore, the horizontal borehole GPR and TDR measurements at 0.2, 0.4, 0.6, 0.8, and 1.2 m depth were assumed to represent the mean SWC of 0.1 - 0.3, 0.3 - 0.5, 0.5 - 0.7, 0.7 - 0.9, and 0.9 - 1.3 m depth,

respectively. The water storage was also calculated from the borehole GPR measurements only. Here, it was assumed that the GPR measurements at 0.2 m depth were representative for the mean SWC of the top 0.30 m of soil.

2.3 Results and discussion

2.3.1 Horizontal borehole GPR data

For a reliable estimation of the SWC changes due to infiltration, the time-zero T_0 has to be known accurately. The change in T_0 during the infiltration experiment is shown in Fig. 2.4. The maximum difference between two adjacent T_0 estimates was relatively small on day 1 (0.34 ns) and day 2 (0.73 ns), but was larger on day 3 (0.96 ns) and day 4 (0.8 ns). The largest variation of T_0 occurred on day 3, which could be caused by a too short warm-up period of the GPR system on this day. The uncertainty in the SWC estimates resulting from a 0.96 ns time-shift is 0.047 cm^3 cm^{-3} independent of the SWC.

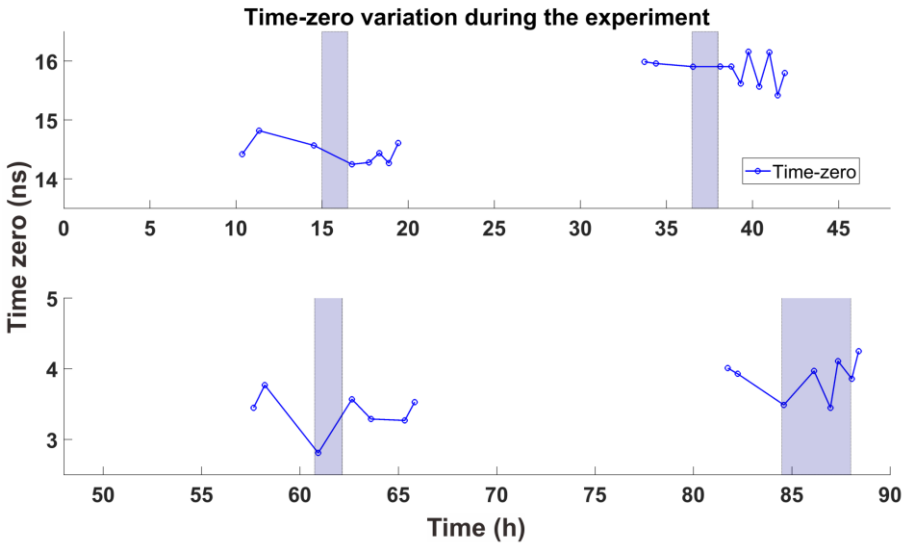

Fig. 2.4 The time-zero T_0 variation during the entire experiment. The duration of the infiltration events is indicated by the light blue background. Note that the y-axis has different scales for the first 2 and last 2 irrigation events.

Spatial SWC variation along the horizontal borehole tubes at five depths before and after the four infiltration events are shown in Fig. 2.5. Before the start of the infiltration experiment, the deeper soil was generally wetter than the top soil (Fig. 2.5a). After the infiltration event on day 1, an increase of the SWC was mainly observed at 0.2 m depth and the deeper soil was less affected. Moreover, infiltration introduced lateral heterogeneity in SWC at 0.2 m depth, especially at the

first and second day, which could be caused by the layout of the dripping system and the heterogeneity of the soil. During the infiltration events at day 3 and 4, the soil at 0.2 m depth was almost saturated and an increase of SWC was observed at all depths.

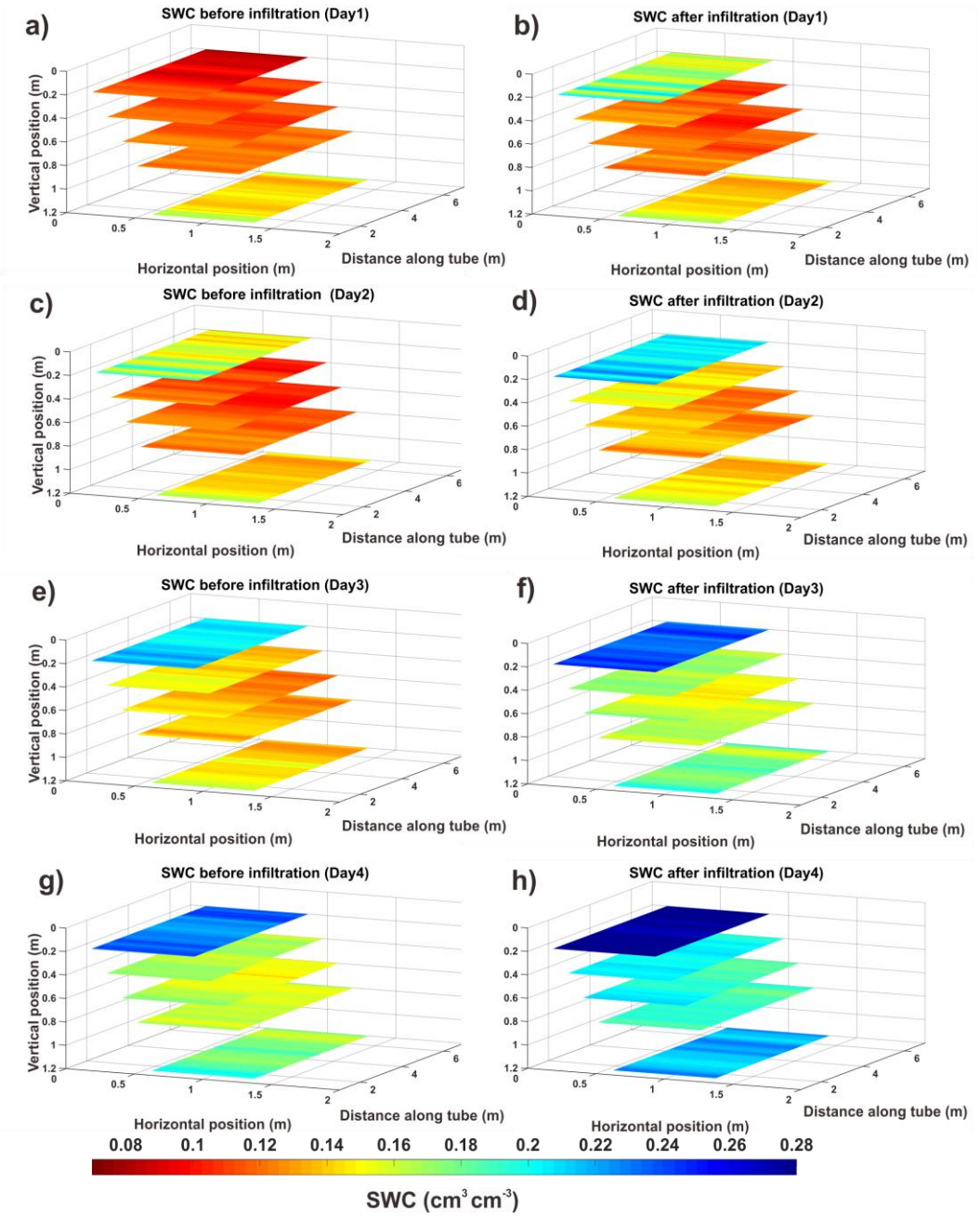

Fig. 2.5 Semi-3D image of SWC estimates from horizontal borehole GPR. Panels on the (a, c, e, and g) left side were measured before infiltration events for the four respective days, whereas panels on the (b, d, f, and h) right side were measured after the infiltration events for the respective days.

2.3.2 Semblance analysis of surface GPR data

The results of the semblance analysis for three different frequencies before and after infiltration are exemplary shown in Fig. 2.6. For the 100 and 200 MHz measurements gathered before infiltration (Fig. 2.6a, 2.6c), only the air wave could be identified because the soil was very dry and a large part of the radiation energy was thus contained in this wave.

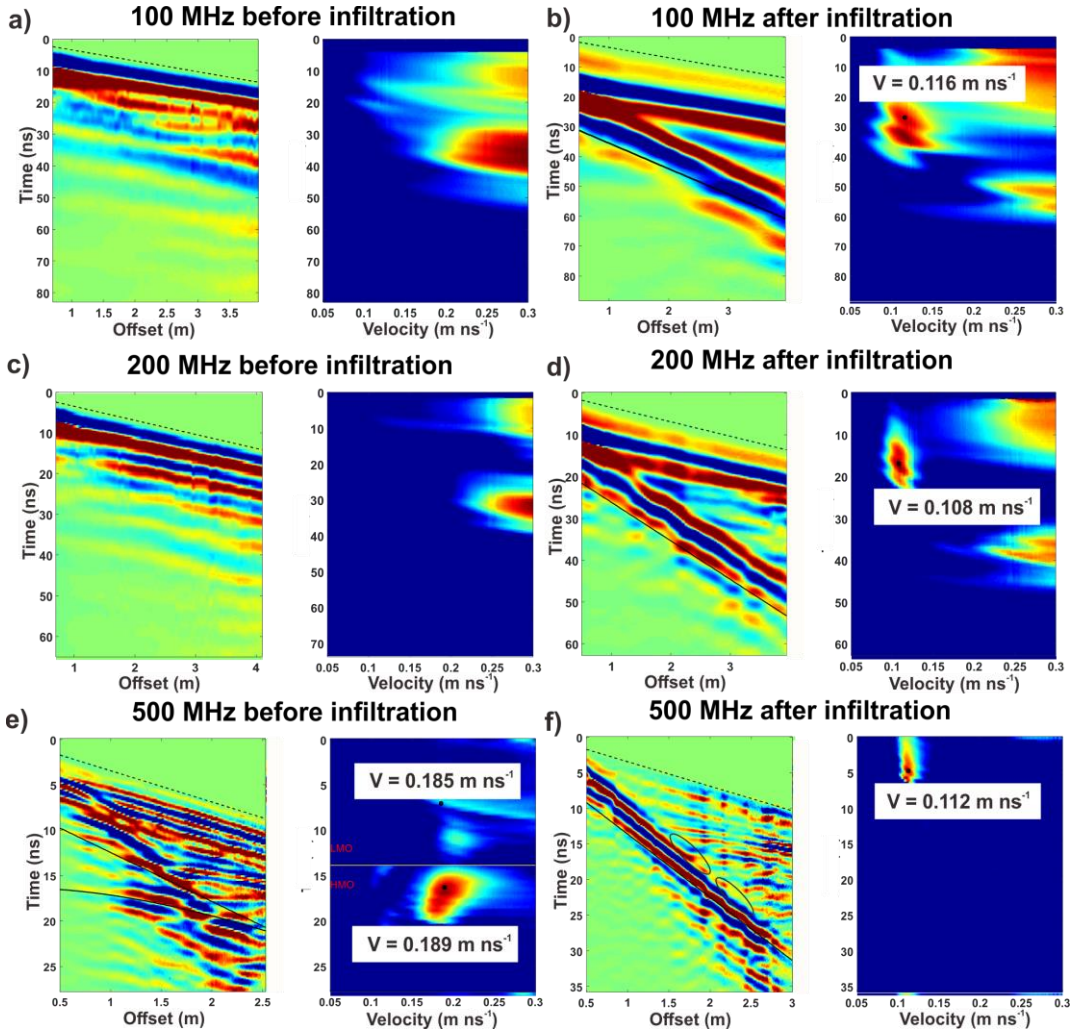

Fig. 2.6 WARR measurements with 100, 200, and 500 MHz data (right panel a, c, e) before and (left panel b, d, f) after infiltration and their semblance spectra. The black dashed lines indicate the first arrival of the direct air wave. The guided wave is enclosed by red dashed lines. The velocities of the ground and reflected wave were picked in the semblance spectra and indicated by the black circles. The corresponding ground and reflected waves are shown by straight and hyperbolic lines in the WARR measurements, respectively. The phase-shift of guided wave is enclosed by the eclipses.

For the 500 MHz data (Fig. 2.6e), a reflection from the bottom of the excavated field plot is observed as a hyperbolic move-out. Because of the strong interference with the air wave, the estimated velocity (0.19 m ns^{-1}) from the semblance analysis is not accurate, and can therefore not be used to estimate SWC. After infiltration, a clear ground wave could be observed for all frequencies (Fig. 2.6b, 2.6d and 2.6f). Additionally, the phase-shift of the ground wave in Fig. 2.6f suggests that the 500 MHz data were dispersive after the infiltration event, which was not observed in the 100 and 200 MHz data.

2.3.3 Dispersion analysis of surface GPR data

After the infiltration event of day 1, a guided wave was observed during the remainder of the infiltration experiment. Four typical WARR measurements obtained at day 2 of the infiltration experiment are shown in Fig. 2.7. The first WARR measurement (Fig. 2.7a) was obtained before the start of the infiltration on day 2. The low-velocity waveguide induced by the irrigation event of day 1 was still clearly present. The dispersion curve of the TE_0 is well defined and smooth, and the first higher mode TE_1 can also be easily identified (Fig. 2.7b).

In a first step, the TE_0 mode was used for inversion (Table 2.3). To validate the obtained results of the dispersion inversion, I performed synthetic forward modelling with the obtained inversion results using the GprMax software (Giannopoulos, 2005; Warren et al., 2016) (Fig. 2.7c, f, i, l). The slope and the phase-shift of the simulated guided waves matched well with the measured data. It should be mentioned that the field was relatively heterogeneous at the beginning of the infiltration due to the layout of the dripping system. Therefore, the dispersion curve of the data measured at the beginning of the infiltration event (Fig. 2.7e) was not only found to be distorted and of shorter frequency range (200 – 500 MHz) than other data, but also the TE_1 mode could not be identified. Consequently, a large ε_1 and a small layer thickness h_t were obtained with a larger uncertainty from inversion (Bikowski et al., 2012).

In a second step, data for the TE_0 and TE_1 mode were jointly inverted (Table 2.3). Compared to the inversion with TE_0 only, the TE_0-TE_1 inversion generally resulted in slightly larger ε_1 and smaller layer thickness h_t. TE_0 and TE_0-TE_1 results showed a good consistency and the largest difference between these two inversion approaches was also small with a difference of 0.085 for ε_1 and 0.016 m for h_t. Therefore, it was concluded that the consideration of the TE_1 mode in the inversion did not result in different waveguide parameters compared to the use of the TE_0 mode only. Additionally, since the TE_1 mode could not be identified for all measured GPR data, it was preferred to consistently use the TE_0 mode only for inversion.

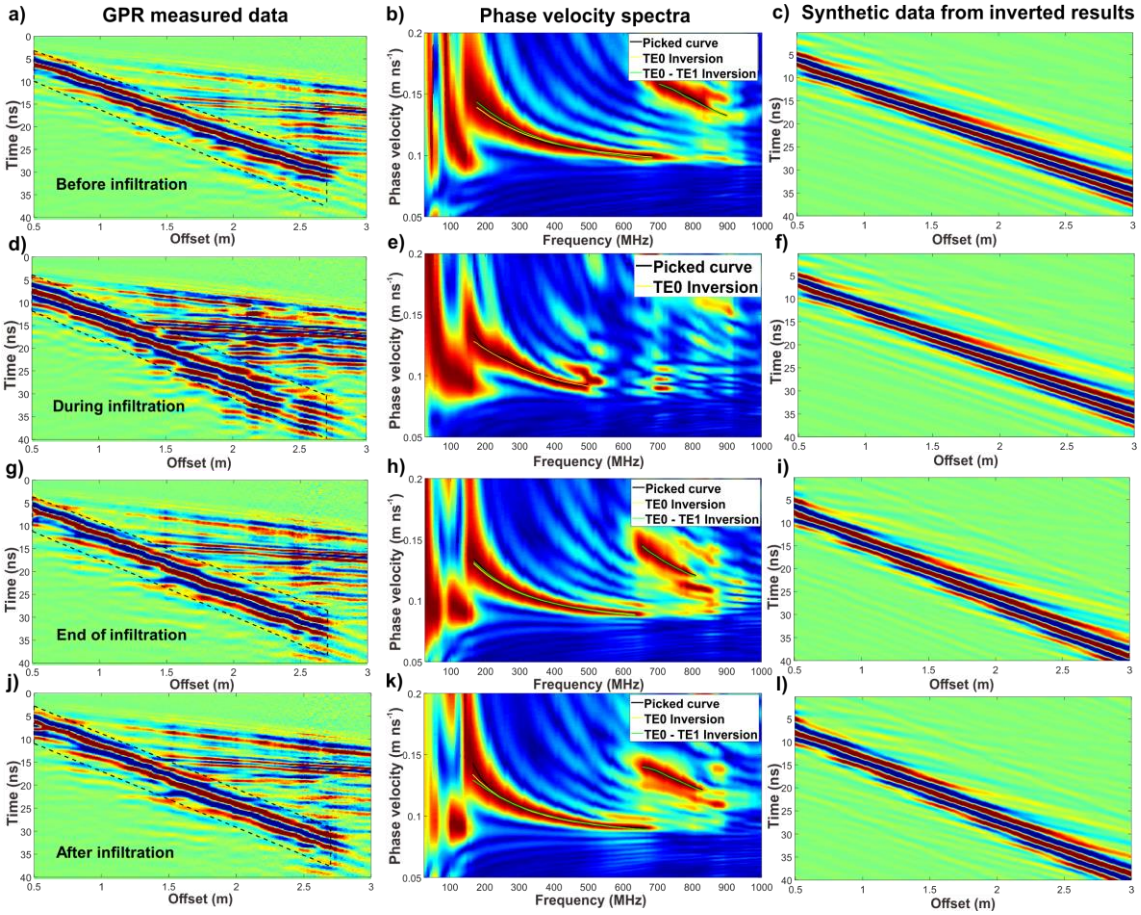

Fig. 2.7 Four typical dispersive WARR measurements with associated phase velocity spectra and modelled WARR measured obtained (a, b, c) before, (d, e, f) at the start of the infiltration event, (g, h, i) at the end of the infiltration event, and (j, k, l) after the infiltration event on day 2 of infiltration experiment. The guided waves are enclosed by the black dashed lines (left panel), which were also used to generate corresponding phase-velocity spectra. Synthetic modelled WARR data based on the TE_0 inversion results.

Table 2.3 Inversion results of dispersive 500 MHz data obtained in day 2

Data	Inversion methods	ε_1; SWC (-);($cm^3\,cm^{-3}$)	ε_2 (-)	h_t (m)	C_m (m ns^{-1})
Fig. 2.7a	TE_0	11.40;0.201	3.82	0.100	0.0013
	TE_0-TE_1	12.25;0.224	3.57	0.084	0.0019
Fig. 2.7d	TE_0	16.59;0.294	4.88	0.068	0.0017
Fig. 2.7g	TE_0	14.22;0.257	3.85	0.095	0.0007
	TE_0-TE_1	14.82;0.266	3.75	0.087	0.0011
Fig. 2.7j	TE_0	13.94;0.253	3.27	0.097	0.0009
	TE_0-TE_1	14.43;0.261	4.54	0.085	0.0019

The SWC estimates from the semblance and dispersion analysis as well as the calculated sampling depth derived from Eq. 2.3 are summarized in Table 2.4 for all surface GPR measurements. For the 500 MHz data, the SWC estimates obtained from semblance and dispersion analysis deviated considerably. This is due to the fact that the SWC obtained by semblance analysis is based on the group velocity of the guided wave, which is always lower than the phase velocity according to Eq. 2.4. As a result, semblance analysis underestimated SWC of the top layer for 500 MHz measurements. The results of the dispersion analysis suggest that the thickness of the waveguide was around 0.1 m during the entire experiment. This is attributed to layering caused by regular agricultural activity.

Table 2.4 Results of semblance and dispersion analysis

Time	Semblance results SWC ($cm^3\,cm^{-3}$); sampling depth Z_G(m)			Dispersion analysis (500 MHz)
	100 MHz	200 MHz	500 MHz	SWC(cm^3cm^{-3}); h_t (m)
Day 1				
11:32	/	/	/	/
15:26†	0.125; 0.747	0.095; 0.554	0.075; 0.362	/
16:28	0.152; 0.718	0.116; 0.535	0.136; 0.328	0.202;0.107
17:21	0.139; 0.731	0.119; 0.533	0.134; 0.329	0.189;0.135
18:39	0.138; 0.732	0.125; 0.528	0.124; 0.330	0.198;0.111
19:39	0.133; 0.738	0.129; 0.524	0.134; 0.329	0.194;0.116
Day 2				
12:00	0.148; 0.722	0.137; 0.519	0.131; 0.330	0.201;0.100
12:48†	0.173; 0.698	0.169; 0.495	0.163; 0.316	0.294;0.068
13:41†	0.183; 0.688	0.182; 0.487	0.191; 0.304	0.254;0.125
14:23†	0.178; 0.693	0.180; 0.488	0.171; 0.313	0.254;0.108
15:53	0.179; 0.692	0.167; 0.497	0.168; 0.314	0.257;0.095
17:04	0.168; 0.702	0.161; 0.501	0.167; 0.314	0.259;0.090
18:02	0.173; 0.697	0.171; 0.495	0.155; 0.319	0.253;0.097
Day 3				
10:50	0.179; 0.692	0.173; 0.493	0.153; 0.320	0.243;0.096
13:09†	0.180; 0.691	0.186; 0.485	0.168; 0.314	0.289;0.087
13:42†	0.204; 0.691	0.212; 0.469	0.191; 0.304	0.280;0.097
14:22†	0.204; 0.691	0.197; 0.478	0.182; 0.308	0.286;0.099
15:22	0.202; 0.672	0.189; 0.482	0.171; 0.313	0.283;0.083
16:44	0.197; 0.676	0.188; 0.483	0.169; 0.314	0.269;0.090
Day 4				
10:30	0.165; 0.705	0.179; 0.489	0.160; 0.317	0.247;0.097
12:49†	0.185; 0.687	0.186; 0.484	0.173; 0.311	0.338;0.062
13:21†	0.186; 0.686	0.210; 0.470	0.219; 0.294	0.298;0.091
13:52†	0.197; 0.676	0.205; 0.473	0.189; 0.305	0.311;0.082
15:07†	0.214; 0.663	0.204; 0.474	0.201; 0.300	0.306;0.092
16:11	0.192; 0.680	0.215; 0.467	0.188; 0.306	0.285;0.099

SWC was calculated by the CRIM.

Sampling depths of ground wave were calculated with Eq. 2.3

† Measuring times during the infiltration event.

2.3.4 Combined horizontal borehole and surface GPR data

The vertical SWC profiles obtained by combining the dispersion analysis and the mean SWC along the horizontal borehole tubes can be used to analyze the spatiotemporal soil water content evolution during the infiltration experiment (Fig. 2.8). As expected, changes in SWC were first observed at shallow depth (0.2 m) during the infiltration event on day 1. The GPR data gathered at 0.4 m depth also indicate a small increase in SWC, but measurements below 0.4 m were unaffected by the infiltrating water (Fig. 2.8a). Vertical SWC profiles measured before and after infiltration are shown in Fig. 2.9. After the irrigation event on day 1, the SWC obtained from surface GPR increased slightly overnight. This is possibly caused by the horizontal movement of water within the top soil layer during the night. After the start of the infiltration on day 2, the SWC increased and stayed at a relatively constant value and the thickness of the waveguide did not change. With further irrigation, the SWC close to the surface increased but water also moved downwards, as indicated by the increase in SWC below 0.4 m.

Water obviously redistributed to deeper depths between the infiltration event of day 2 and day 3 but also between day 3 and day 4 (Fig. 2.9). The SWC profiles for day 3 and day 4 show a clear increase in SWC for all depths during the infiltration event (Fig. 2.8c and 2.8d). The movement of the wetting front can clearly be seen in Fig. 2.9. After infiltration at day 1, the wetting front moved to a depth between 0.2 m and 0.4 m. After the infiltration event at day 2, the upper 0.8 m depth were wetted but the SWC at 1.2 m depth did not change yet. For the infiltration events at day 3 and day 4, it was observed that SWC increased at all depths, which suggests that the wetting front quickly moved to below 1.2 m depth at these days, which is a consequence of the higher initial water content in the soil profile and the associated higher unsaturated hydraulic conductivity.

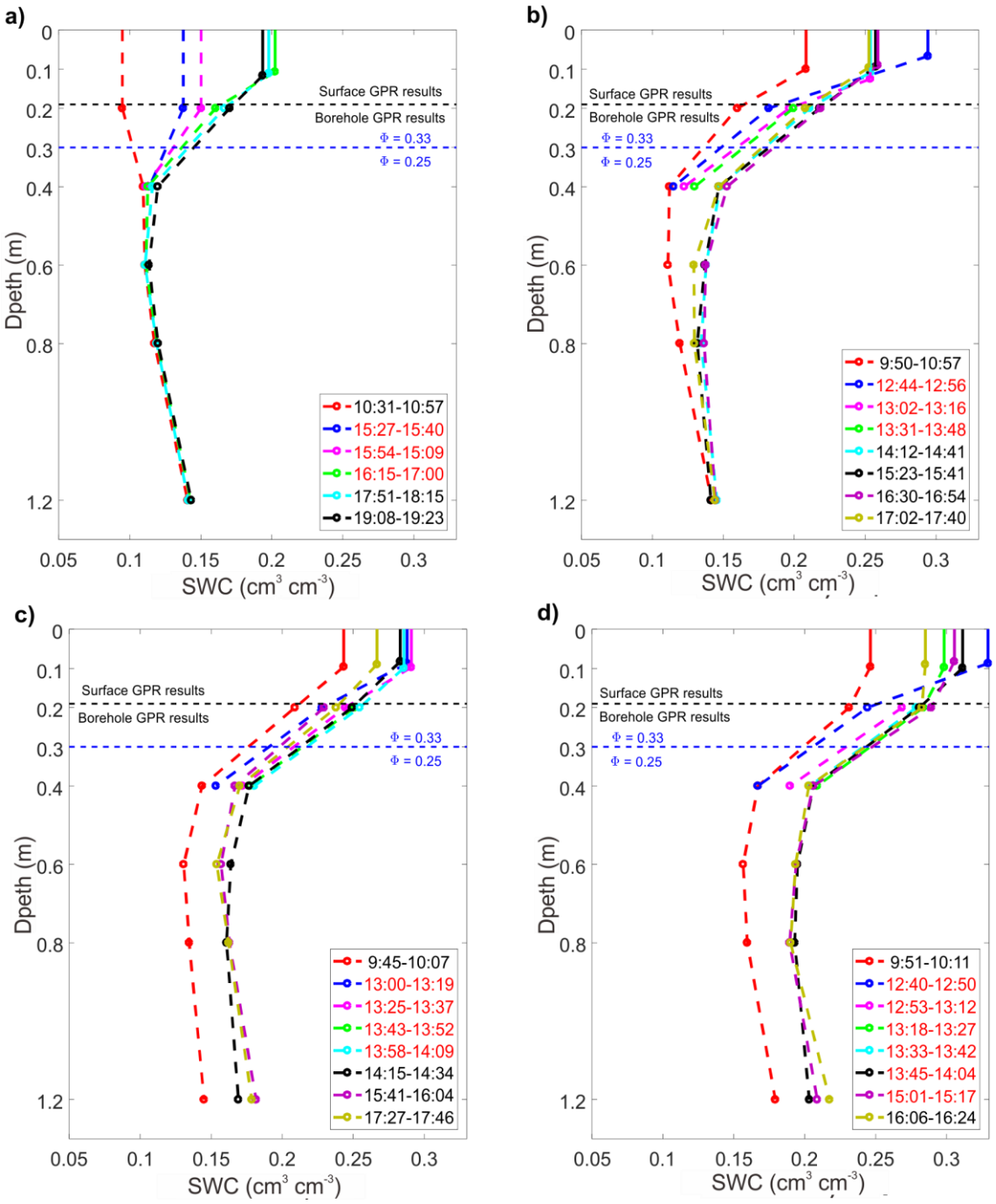

Fig. 2.8 Vertical SWC profiles at (a) day 1, (b) day 2, (c) day 3, and (d) day 4. The colors indicate the different times when the measurements were performed, whereas measurements taken during infiltration are shown in red in the legend. Above the horizontal black dashed line, the surface GPR results are shown, whereas the averaged borehole GPR results are plotted below this line. Note that the total porosity Φ changes from 0.33 to 0.25 at 0.3 m depth as indicated by the blue solid line due to previous tillage practice.

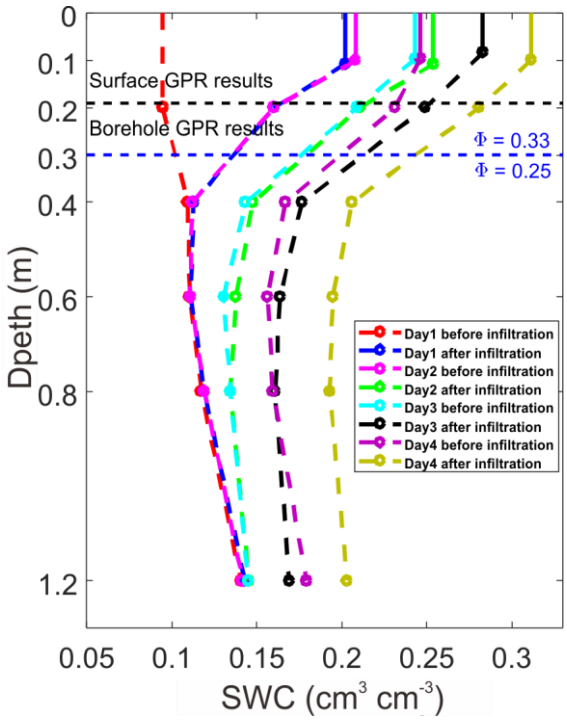

Fig. 2.9 Combined GPR SWC profiles measured before and after infiltration events for all days.

The time series of average SWC obtained with TDR sensors at six depths are shown in Fig. 2.10a along with the SWC estimated from the GPR measurements (average for the entire borehole length). It can be seen that the GPR and TDR measurements show a rapid and synchronous response to the four infiltration events and similar trends in SWC increase. Nevertheless, the SWC estimates obtained with GPR and TDR differed considerably, especially at 0.1 and 0.2 m depth. In particular, the SWCs determined with GPR measurements were higher than that obtained with TDR measurements at 0.1 m and lower at 0.2 m depth. These differences are attributed to the different sensing volumes of the TDR and GPR measurements. The TDR sensors provide point measurements approximately 1 m away from the trench wall, whereas the GPR measurements represent the average SWC of the top soil from 1.5 m to 7 m away from the trench. Therefore, GPR is expected to be more representative of the irrigated area and thus provide improved ability to monitor wetting front movement in this experiment. For example, SWC obtained with TDR increased up to a depth of 0.4 m during the first infiltration event, while the SWC obtained with GPR only responded at 0.1 and 0.2 m depth. Although it is possible that water infiltrated to 0.4 m depth in some places due to the spatial soil heterogeneity, it is unlikely that the wetting front moved to 0.4 m depth over the entire infiltration area because only 2.84 cm of water was applied in the first infiltration event.

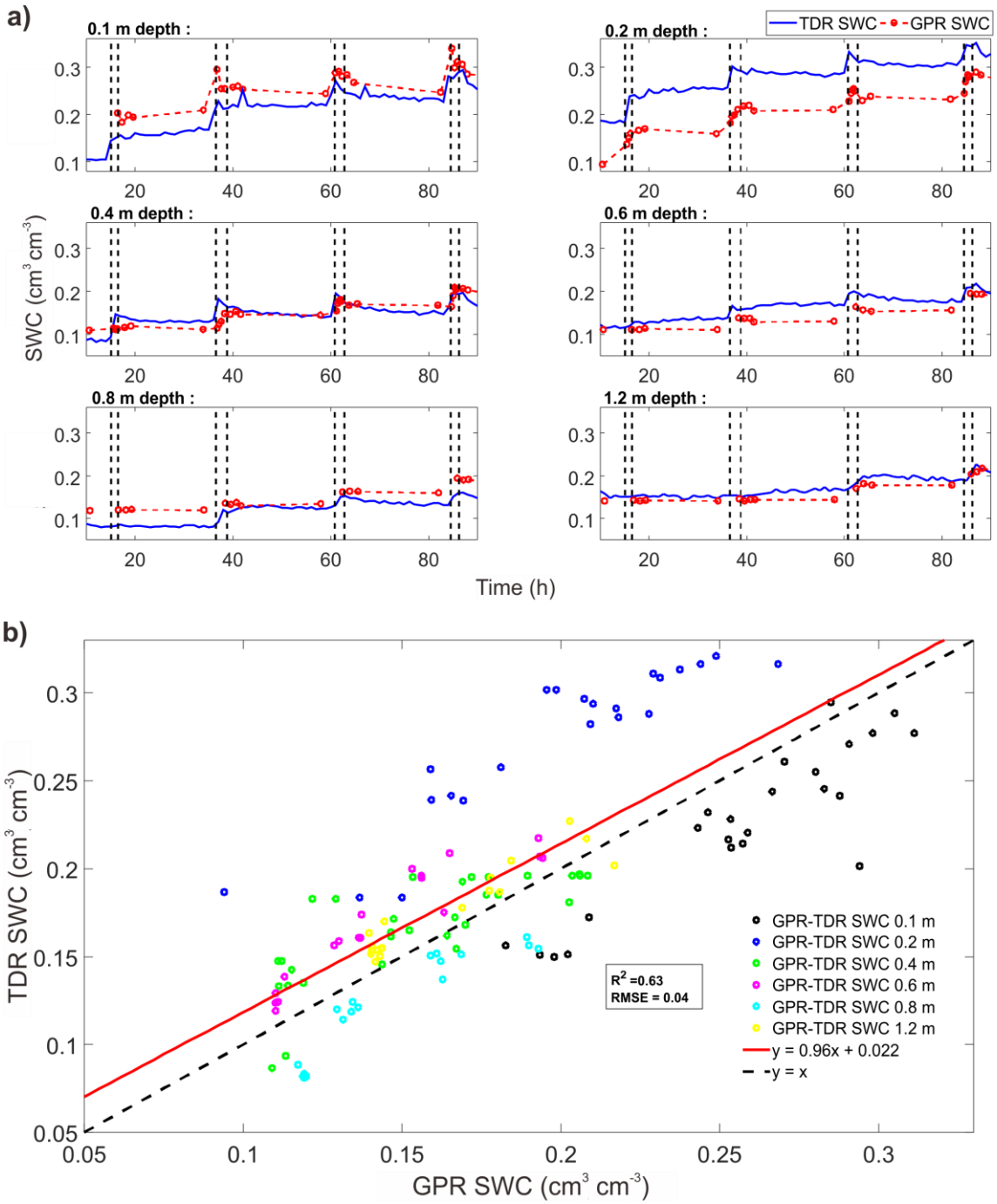

Fig. 2.10 (a) SWC time series at different depths obtained with GPR and TDR. Black dashed lines indicate the start and end time of infiltration events. (b) Comparison of SWC measurements obtained with GPR and TDR. Different colors represent different depths of investigation. Both the 1:1 line (dashed black) and a linear regression (red) are also shown.

The correlation between depth-averaged SWC obtained with GPR and TDR is shown in Fig. 2.10b. The linear regression between GPR and TDR results has a slope close to one, and the intercept is also small. This indicates an unbiased and fairly good agreement between GPR and the TDR data. However, there is substantial scatter in this relationship as indicated by the relatively low explained variance (R^2 of 0.63) and the high root mean square error (RMSE of 0.04 $cm^3\ cm^{-3}$). As mentioned before, the misfit is strongest for the shallow soil layers (0.1 and 0.2 m). There is a range of possible explanations for the relatively large misfit. First, there is some uncertainty in using surface GPR measurements to estimate SWC at 0.1 m depth since the inverted layer depth is varying around 0.1 m during the experiment and a homogeneous water content distribution in the top layer is assumed in the single-layer waveguide dispersion. Second, there is uncertainty in time-zero estimation for the horizontal borehole GPR data. Third, there is intrinsic uncertainty in the SWC estimates obtained with GPR and TDR. This includes uncertainty in travel time determination for both GPR and TDR and the uncertainty in the position of the horizontal boreholes. Fourth and foremost, there is a considerable difference between the sampling volumes of GPR and TDR (Klotzsche et al., 2019a; Huisman et al., 2001), which likely explains a considerable part of the observed scatter given the lateral heterogeneity of soil within the 7 m long facility.

To independently validate the GPR and TDR results, the change in water storage of the total profile was calculated for each individual measurement time (Fig. 2.11). To do so, the initial water storage before the start of the first infiltration experiment was subtracted from all other water storages calculated from the estimated SWC (Loeffler and Bano, 2004). Therefore, the increase in soil water storage for the upper 1.3 m depth can be directly compared with the total amount of irrigated water. The standard deviation of the SWC measurements obtained with GPR was used to represent the spatial variation of the water storage along the borehole tubes (black error bars in Fig. 2.11). Also, the spatial variation of the TDR water storage along the facility wall was visualized (yellow error bars in Fig. 2.11). It can be seen that the observed TDR water storage systematically overestimated the expected increase in water storage based on the irrigation amount by around 25% for day 1 to day 3. On the contrary, the increase in water storage obtained from borehole GPR only showed a 5 - 10% underestimation for day 1 and day 2. This is attributed to the lack of information on the SWC up to a depth of 0.2 m. By combining the surface and borehole GPR data, the error in water storage estimates was further reduced to 4 - 8% for day 1, 2, and 4. Only for day 3, the combined GPR results overestimated the increase in water storage by 0.008 m (10%), which can be explained by the relatively large uncertainty in the time-zero estimation for borehole GPR measurements at day 3 (Fig. 2.4). Towards the end of the infiltration

experiment, it is likely that water drained below the investigated depth range due to deep drainage (Fig. 2.8). Therefore, an underestimation of the increase in water storage should be expected for day 3 and day 4. Although the combined GPR result showed a good match with the known water amount for day 4, the water storage of the field is thus still potentially overestimated. Overall, it is concluded that the combined borehole and surface GPR measurements outperformed the two other methods for water storage estimation in this case.

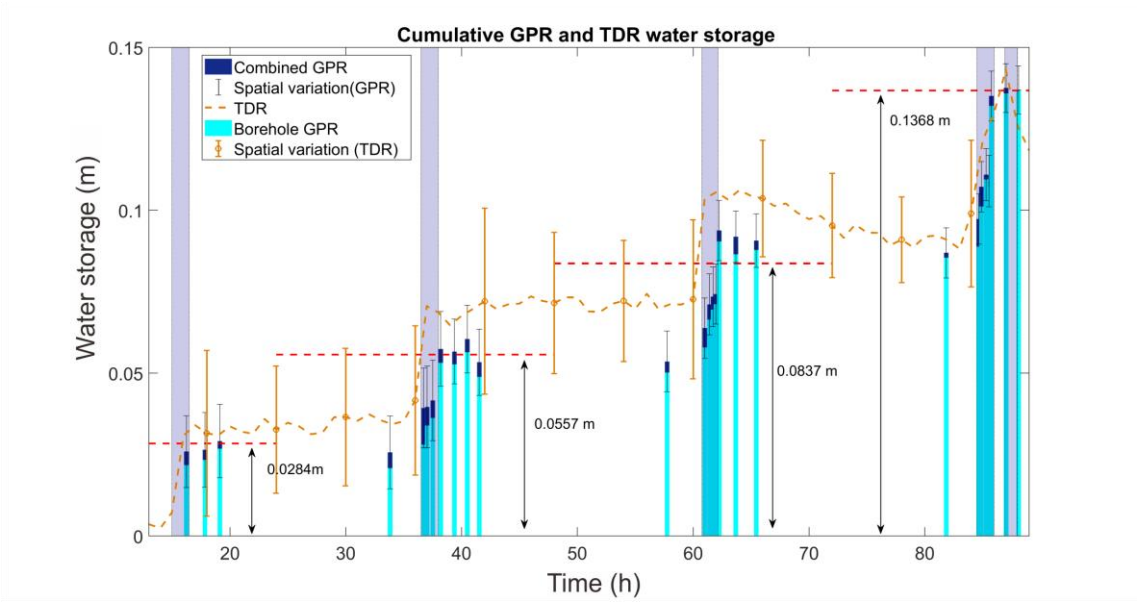

Fig. 2.11 Time series of changes in water storage estimated with borehole GPR (light blue bars), a combination of borehole and surface GPR (dark blue bars), and TDR (yellow dashed line). Light purple bars indicate time of irrigation and red dotted line the total water added to the system.

2.4 Summary and conclusions

In this chapter, surface and horizontal borehole GPR measurements were combined to investigate soil water content (SWC) dynamics up to a depth of 1.2 m in a field-scale infiltration experiment. Borehole GPR measurements provided SWC at five depths using zero-offset profiling (ZOP) surveys. Reference TDR measurements were taken hourly at six depths. In general, wetting front movement over the experimental period could clearly be monitored using GPR and TDR. However, the use of horizontal borehole GPR data alone failed to provide information on SWC changes of the top soil since the interpretation of borehole GPR measurements at 0.1 m depth was hindered by the interference of direct and critically refracted waves. Therefore, I additionally made surface GPR measurements to characterize the top soil. The surface GPR measurements with 500 MHz antenna showed infiltration-induced waveguides. Single layer waveguide

inversion was used to invert waveguide properties. By combining surface and horizontal borehole GPR results, representative vertical SWC profiles over the entire depth (0 – 1.2 m) were obtained for the entire infiltration experiment. The SWC profiles obtained by borehole GPR, combined borehole/surface GPR, and TDR were used to calculate water storage changes after infiltration and were compared to the amount of irrigated water. This analysis showed that TDR systematically overestimated the increase in water storage, which was attributed to the poor spatial representativeness of the local TDR measurements. The increase in water storage due to infiltration calculated from borehole GPR only underestimated water storage as long as the topsoil layer was not saturated. The combined use of borehole and surface GPR measurements provided the most accurate estimates of the increase in water storage. Nevertheless, further studies are needed to prove the advantage of the combined borehole/surface method for more natural infiltration events (e.g., natural rainfall). In addition, future work will explore the use of coupled hydrogeophysical inversion approaches to estimate soil hydraulic properties from the GPR data.

CHAPTER 3 SEQUENTIAL AND COUPLED INVERSION OF HORIZONTAL BOREHOLE GROUND PENETRATING RADAR DATA TO ESTIMATE SOIL HYDRAULIC PROPERTIES AT THE FIELD SCALE[2]

Abstract

Horizontal borehole ground penetrating radar (GPR) measurements can provide valuable information on soil water content dynamics in the vadose zone, and hence show potential to estimate soil hydraulic properties. In this chapter, the performance of both sequential and coupled inversion workflows to obtain soil hydraulic properties from time-lapse horizontal borehole GPR data obtained during an infiltration experiment were compared using a synthetic modelling study and the analysis of actual field data. The sequential inversion using the vadose zone flow model HYDRUS-1D directly relied on soil water content (SWC) profiles determined from the travel time of GPR direct waves using the straight-wave approximation. The synthetic modelling study showed that sequential inversion did not provide accurate estimates of the soil hydraulic parameters due to interpretation errors in the estimated SWC near the infiltration front and the ground surface. In contrast, the coupled inversion approach, which combined HYDRUS-1D with a forward model of GPR wave propagation (gprMax3D) and GPR travel time information, provided accurate estimates of the hydraulic properties in the synthetic modelling study. The application of the coupled inversion approach to measured borehole GPR data also resulted in plausible estimates of the soil hydraulic parameters. It was concluded that coupled inversion should be preferred over sequential inversion of time-lapse horizontal borehole GPR data in the presence of strong SWC gradients that occur during infiltration events.

[2] Adapted from Yu, Y., Weihermüller, L., Klotzsche, A., Lärm, L., Vereecken, H., Huisman, J.A., 2021. Sequential and coupled inversion of horizontal borehole ground penetrating radar data to estimate soil hydraulic properties at the field scale. J. Hydrol. 126010. doi: 0.1016/j.jhydrol.2021.126010

3.1 Introduction

Obtaining accurate hydraulic parameters of the vadose zone is important in a wide range of applications, including modelling of water flow and contaminant transport (e.g., Vereecken et al., 2007; Wagner, 1992;, managing water and soil resources (e.g., Blanco-Canqui and Lai, 2007; Hartmann et al., 2014), and evaluating climate change effects on forests (e.g., Martínez-Vilalta et al., 2002; McDowell and Allen, 2015). Hydraulic parameters can be determined by different laboratory methods (e.g., Neuzil et al., 1981), but this typically leads to hydraulic property estimates that are not representative of field conditions (Kool et al., 1987). Therefore, estimation of hydraulic properties at the field scale is preferred if characterization at this scale is intended (Klute and Dirksen, 1986).

Field-scale estimation of hydraulic properties is commonly based on measurements made with point-scale sensors, such as the neutron probe (Chanasyk and Naeth, 1996) and time domain reflectometry (TDR) (Robinson et al., 2008). Such methods allow the accurate determination of soil water content (SWC) dynamics, and therefore have been widely used for parameterizing hydrological models (e.g., Abbaspour et al., 2000; Katul et al., 1993; Kumar et al., 2010; Malicki et al., 1992; Nandagiri and Prasad, 1996; Steenpass et al., 2010; Wollschläger et al., 2009). In some studies, SWC measurements were combined with matric potential measurements obtained by tensiometers (e.g., Zhang et al., 2003) in order to better constrain the hydraulic parameter estimation (Vereecken et al., 2008). A major disadvantage of using point sensor information to estimate soil hydraulic properties is the relatively small sensing volume and the resulting limited representativeness for the field-scale soil states.

In the last decades, many studies reported the potential of using geophysical techniques, such as electromagnetic induction (EMI) (e.g., Brosten et al., 2011; Moghadas et al., 2017), electrical resistivity tomography (ERT) (e.g., Brunet et al., 2010; Huisman et al., 2010; Manoli et al., 2015; Mboh et al., 2012; Pollock and Cirpka, 2010) and ground penetrating radar (GPR) (e.g., Hubbard and Rubin, 2000; Looms et al., 2008a; Rossi et al., 2015), to obtain accurate field-scale estimates of SWC and soil hydraulic properties. GPR uses the travel time and attenuation of high-frequency electromagnetic waves travelling through the ground to obtain the dielectric permittivity ε and electrical conductivity σ of the subsurface (e.g., Holliger et al., 2001; Slob et al., 2010). Due to the direct relationship between ε and SWC (Topp et al., 1980), GPR is the one of the most promising geophysical methods for SWC estimation (e.g., Huisman et al., 2003a; Klotzsche et al., 2018). GPR can rapidly provide surveys for larger scales of interest (1 ~ 1000 m profiles) (e.g.,

Mahmoudzadeh Ardekani, 2013), which implies that GPR is capable of characterizing the spatiotemporal SWC distribution at the field scale (e.g., Steelman et al., 2012).

In general, GPR measurements can be performed off the ground surface (off-ground GPR) (e.g., Lambot et al., 2004), on the soil surface (surface GPR) (e.g., Huisman et al., 2002; van Overmeeren et al., 1997) or in vertical or horizontal boreholes (borehole GPR) (e.g., Redman et al., 2000). Off-ground GPR relies on the use of an ultra-wide frequency band for subsurface investigations, and hence can potentially provide high-resolution information about the soil states. However, off-ground GPR measurements are influenced by surface roughness and only have a limited penetration depth (Lambot et al., 2006a). For surface GPR measurements, SWC can be estimated based on the analysis of the direct ground wave (Grote et al., 2003; Weihermüller et al., 2007) or reflected waves (Lunt et al., 2005). Both GPR acquisition strategies have been successfully used to monitor water flow dynamics in unsaturated soil (Allroggen et al., 2015; Mangel et al., 2012; Moysey, 2010). The penetration depth of surface GPR is limited by the soil characteristics, especially by the bulk electrical conductivity. Furthermore, there is no control on the vertical resolution when using reflected waves for SWC determination (Huisman et al., 2003a). Borehole GPR can overcome these limitations but requires the availability and accessibility of appropriate boreholes or wells, and is therefore restricted to specialized test sites and experimental set-ups. Borehole GPR measurements have also been used to monitor SWC dynamics (Looms et al., 2008b). In addition, zero-offset profiling (ZOP) measurements between horizontal boreholes have been used to monitor SWC dynamics (Cai et al., 2016; Galagedara et al., 2002; Klotzsche et al., 2019a). Due to the good control on the vertical resolution and the improved spatial representativeness for the field plot scale, this kind of set-up provides detailed information on the spatial and temporal variation of SWC.

In order to derive soil hydraulic parameters from time-lapse GPR data, two types of inversion strategy can be used. The first type is commonly called sequential inversion and consists of three steps (Hinnell et al., 2010; Huisman et al., 2010). First, the dielectric permittivity ε is determined from the first arrival time of a GPR measurement using a straight-ray approximation (e.g., Galagedara et al., 2002) or a full-waveform inversion (e.g., Klotzsche et al., 2019b). Second, a petrophysical relationship is used to convert ε to SWC using the empirical Topp's equation (Topp et al., 1980) or a more advanced dielectric mixing model (Roth et al., 1990). Third, the obtained time-lapse SWC data are used in combination with a hydrological model to estimate soil hydraulic parameters using inverse modelling. However, the use of a sequential inversion strategy may cause errors in the estimated soil hydraulic parameters when errors due to simplified geophysical

data interpretations propagate into the estimated soil hydraulic parameters. An example of a potential source for such errors is the use of the straight-wave approximation for the travel path of the electromagnetic waves (Rucker and Ferré, 2004a). To overcome this problem, a coupled inversion strategy can be used (Hinnel et al., 2010; Lambot et al., 2006b). In contrast to sequential inversion, a coupled inversion links a hydrological model directly with a forward model of the geophysical data, and the mismatch between measured and modelled geophysical response is minimized (i.e., first arrival time or even the full waveform in the case of GPR). In doing so, the soil hydraulic parameters used in the hydrological model can be optimized, while error propagation is avoided. The coupled inversion approach relies heavily on an accurate forward hydrological model. A wrong conceptualization of the subsurface in terms of layering or processes not adequately captured by the hydrological model (e.g., dual porosity or macropore flow) will introduce errors that propagate into the estimated parameters.

A range of studies have employed off-ground GPR, surface GPR, and vertical borehole GPR measurements for estimating soil hydraulic properties from time-lapse SWC information by using either a sequential or a coupled inversion approach (e.g., Busch et al., 2013; Chen et al., 2001; Chen et al., 2004; Jadoon et al., 2012; Jaumann and Roth, 2018; Jonard et al., 2015; Kowalsky et al., 2005; Lambot et al., 2009; Rucker and Ferré, 2004b). Compared to these GPR acquisition strategies, horizontal borehole GPR measurements have several advantages to reveal the temporal and spatial SWC variations at the field plot scale. Firstly, horizontal borehole GPR measurements can provide SWC information at specific depths and thus have larger penetration depth and better control on vertical resolution compared to off-ground and surface GPR. Secondly, horizontal borehole GPR measurements provide a higher lateral spatial representativeness of the field plot compared to vertical borehole GPR measurements. However, no studies have been conducted yet that use horizontal borehole GPR measurements to parameterize a hydrological model. In this chapter, the performance of both sequential and coupled inversion workflows to obtain soil hydraulic properties from time-lapse horizontal borehole GPR data obtained during an infiltration event will be compared. To systematically study the differences between the two inversion approaches, a synthetic modelling experiment will be presented first. In a second step, actual horizontal borehole GPR measurements will be inverted using a coupled inversion approach. The resulting estimates of the hydraulic parameters will be compared to available independent hydraulic property estimates obtained from TDR measurements.

3.2 Method and material

3.2.1 Test site and GPR data acquisition

The details of the test site, experimental set-up, GPR data acquisition, and GPR data analysis were introduced in Section 2.2. Therefore, only a short summary is provided here.

In this facility, three plots (7 x 3 m) were established with different treatments (natural rain, rain-sheltered, and irrigated). GPR access tubes of 7 m length were horizontally installed at 0.1, 0.2, 0.4, 0.6, 0.8, and 1.2 m depth across the entire length of the plot. The soil in the facility originates from fluvial gravel deposits from the Rur river system and is characterized as an Orthic Luvisol with high stone content (>50%) and a loamy texture (Table 3.1). Due to tillage activity, soil porosity Φ changes from 0.33 $cm^3\,cm^{-3}$ near the surface to approximately 0.25 $cm^3\,cm^{-3}$ below 0.3 m depth. In order to install the GPR access tubes, the entire plot was dug out and refilled layer-wise. Therefore, no pedogenetic horizons are detectable anymore below the plough horizon. No clear pedogenetic layers are detectable in the gravely layers of the natural soil either.

The infiltration experiment consisted of five infiltration events that were carried out at the rain-sheltered plot during a 4-day period. Water was infiltrated using a drip irrigation system that was supplied by water from an underground tank at a constant rate (0.03 cm min^{-1}). Approximately 2.7 cm of water was applied for each infiltration event of 90 min (Fig. 3.1a). ZOP surveys were made using a GPR system (PulseEKKO, Sensors & Software, Canada) with 200 MHz borehole antenna. GPR measurements were made at six depths (0.1, 0.2, 0.4, 0.6, 0.8 and 1.2 m) before and after infiltration events. During the infiltration events, GPR measurements were restricted to the boreholes at 0.1, 0.2 and 0.4 m depth as the SWC was expected to increase mainly at shallow depths at the beginning of each infiltration event. For each ZOP survey, the transmitter and receiver were first pushed to the end of the borehole (7 m) and then pulled simultaneously throughout the boreholes in 0.05 m steps. The survey ended at 1.5 m distance from the access trench to avoid that reflections from the trench wall and installed sensors interfered with the direct waves.

Table 3.1 Soil texture of fine soil, mass fraction of stones and porosity of the field according to Cai et al. (2016)

Depth	Sand	Silt	Clay	Stones	Porosity
(cm)			(Mass %)		(cm^3cm^{-3})
Topsoil (0 - 30)	35	52	13	50	0.33
Subsoil (30 – 120)	37	47	16	69	0.25

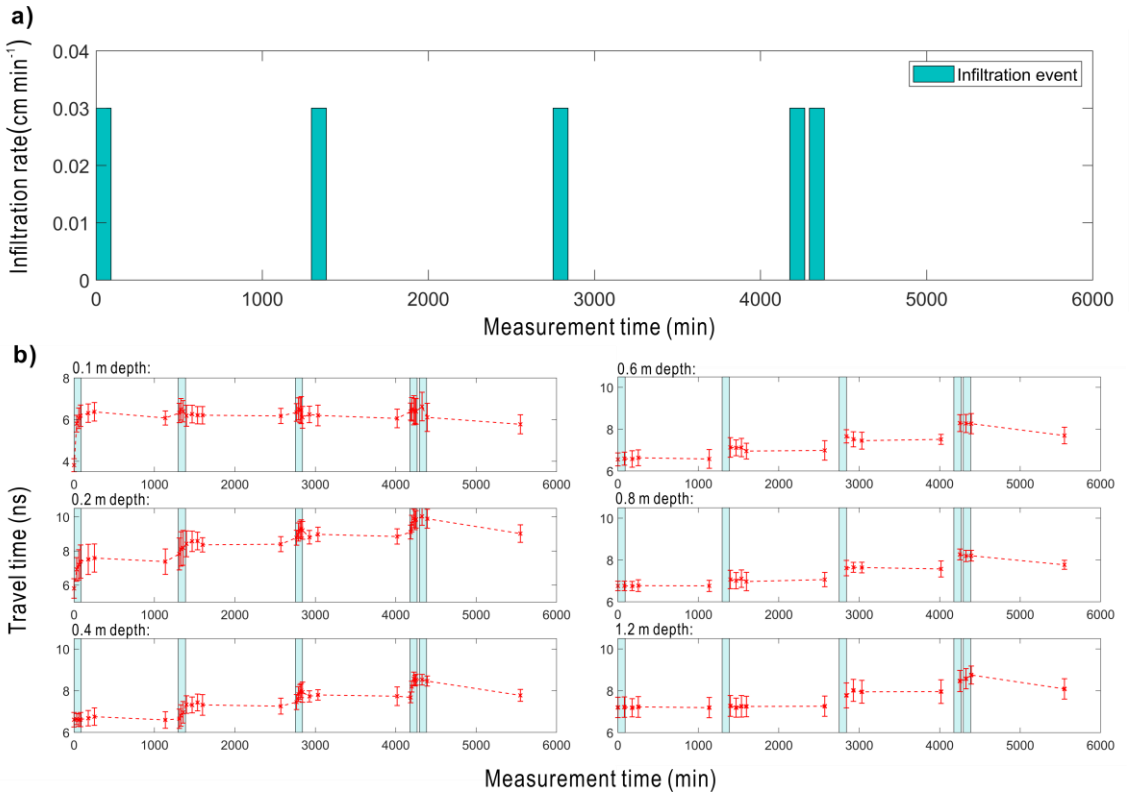

Fig. 3.1 (a) Schedule and amount of irrigated water for the five infiltration events and (b) GPR travel time data measured at 6 different depths during the infiltration experiment. The timing of the infiltration events was indicated by light green background. The spatial variation of the travel times along the 5.5 m borehole tube is indicated by the error bars. Note that different y-axis scales are used for the results of different depths.

The development of the mean GPR travel time at different depths is shown in Fig. 3.1b. To determine the GPR travel time from the ZOP data, the time-zero offset (T_0) and first arrival time (t^{obs}) of the direct wave were determined by using the strategy introduced in Section 2.2.2. In this strategy, T_0 was determined from wide angle reflection and refraction (WARR) measurements with the borehole antennas in air and t^{obs} was manually picked for each trace. GPR travel times measured at 0.1 and 0.2 m depth increased after the first infiltration event. In

response to the second infiltration event, travel times up to a depth of 0.8 m responded to the infiltration. After the third infiltration event, the travel times increased at all depths. The standard deviation of the travel times is also shown in in Fig. 3.1b, which illustrates the spatial variability along the 5.5 m borehole tubes that were generated by the expected differences in the irrigation rate of the used dripping system and small-scale lateral water content variations caused by the heterogeneity of the soil. SWC information at each depth can be estimated based on the straight-ray approximation and CRIM model (Eq. 2.1, Eq. 2.2 and Eq. 2.6).

3.2.2 Hydrological modelling

In this case, HYDRUS-1D was used to simulate the 1D vertical water flow in porous media based on the Mualem - van Genuchten (MvG) model where soil hydraulic properties were described by five parameters K_s, θ_s, θ_r, α, and n (See Section 1.5.1). For the simulation of vertical SWC dynamics, the model domain was set to be 150 cm deep and was discretized with 151 nodes with an equal spacing of 1 cm. Simulations were initialized using linearly interpolated SWC estimates from measured permittivity obtained from borehole GPR data acquired prior to the first infiltration event. Evaporation and root water uptake were both neglected in the simulation, as evaporation was low with respect to the amount of infiltrated water and the soil was bare. An atmospheric boundary condition with surface run-off was used to represent the irrigation events at the upper boundary of the domain. At the lower boundary of the domain, a seepage face (h = 0) was used. The use of a seepage face was required to match SWC observations and avoid excessive drainage out of the profile, which occurred when a free drainage boundary condition was used. A physical explanation for the need to use a seepage face may be the presence of a compacted soil layer directly below the rhizotron facility caused by the construction of the facility. As an alternative to the use of a seepage face, a longer soil profile with a dense layer with low K_s could have been used. However, this would have made the hydrological simulations computationally more demanding, especially in the case of the coupled inversion.

3.2.3 GPR modelling

The gprMax3D model was used to simulate GPR wave propagation with the Finite-difference time-domain (FDTD) numerical method (Giannopoulos, 2005; Warren et al., 2016). The size of the simulation domain for the gprMax3D simulation was set to 2 x 1.1 x 2.2 m, including a soil of 1.5 m thickness below an air layer of 0.7 m. The 3D domain was discretized with nodes with 0.02 m spacing and perfectly matched layers (PML) were used at the boundaries of the model domain (Berenger, 1994). The center frequency of the antenna was set to 200 MHz and the first

derivative of a Gaussian waveform was selected as the excitation function for the current source. As I only considered the velocity information for the GPR data interpretation, the electrical conductivity of the soil was assumed to be zero.

3.2.4 Set-up for sequential and coupled inversion

To estimate hydraulic parameters from horizontal borehole GPR measurements, both sequential and coupled inversion strategies were used. The general set-ups of the two inversion strategies are illustrated in Fig. 3.2a and Fig. 3.2b. A key difference between the two approaches is that the sequential inversion approach directly optimizes the misfit between the SWC obtained from the GPR measurements θ^{obs} (cm^3 cm^{-3}) and the simulated SWC θ^{mod} (cm^3 cm^{-3}) provided by HYDRUS-1D, whereas the coupled inversion optimizes the misfit between the travel time of the measured GPR data t^{obs} (ns) and the simulated travel time t^{mod} (ns) obtained with gprMax3D using SWC information (θ^{mod}) provided by HYDRUS-1D. The misfits for the sequential and coupled inversions were described using cost functions based on the root-mean-square error (RMSE) between observed and simulated data:

$$C_{MVG}(\theta) = \sqrt{\frac{\sum_{i=1}^{n_m}(\theta_i^{mod} - \theta_i^{obs})^2}{n_m}} \tag{3.1}$$

$$C_{MVG}(t) = \sqrt{\frac{\sum_{i=1}^{n_m}(t_i^{mod} - t_i^{obs})^2}{n_m}} \tag{3.2}$$

Where $C_{MVG}(\theta)$ (cm^3 cm^{-3}) and $C_{MVG}(t)$ (ns) are the cost functions based on SWC and travel time, respectively. n_m (-) is the number of GPR measurements.

In order to minimize these cost functions, the shuffled complex evolution (SCE-UA) algorithm introduced by Duan et al. (1993) was used. SCE-UA is a global optimization algorithm that not only has been widely used in hydrological research (e.g., Chu et al., 2010; Thyer et al., 1999) but also in geophysical applications (e.g., Liu et al., 2018; Mangel et al., 2017). The SCE-UA algorithm requires the specification of parameter bounds for each parameter considered in the optimization. The optimization includes several steps. First, different sets of hydraulic parameters are randomly created in the feasible parameter space and the cost function value for each of these parameter sets is calculated. Second, the parameter sets are sorted in order of their cost function value and distributed into several complexes that are subsequently evolved using the competitive complex evolution (CCE) algorithm (Duan et al., 1994). After this first loop of evolution, the complexes are merged again into a single population, which again is sorted in order of increasing cost function value and divided into complexes for the next optimization loop. The algorithm is

considered to be converged if the cost function valued reaches a specified value (i.e., the known error of the data) or if the improvement in the best model is below 0.01% in the last 10 evolution loops.

Since no GPR measurements were made in dry soil conditions, the inversion is not expected to be sensitive to θ_r. In order to build an independent hydrological model based on GPR measurement, θ_r was fixed it to 0 for the inversion and only K_s, θ_s, α, and n were estimated. K_s was inverted by using its log-transform ($\log(K_s)$). The algorithms for both sequential and coupled inversion were coded in GNU Octave (Eaton, 2012).

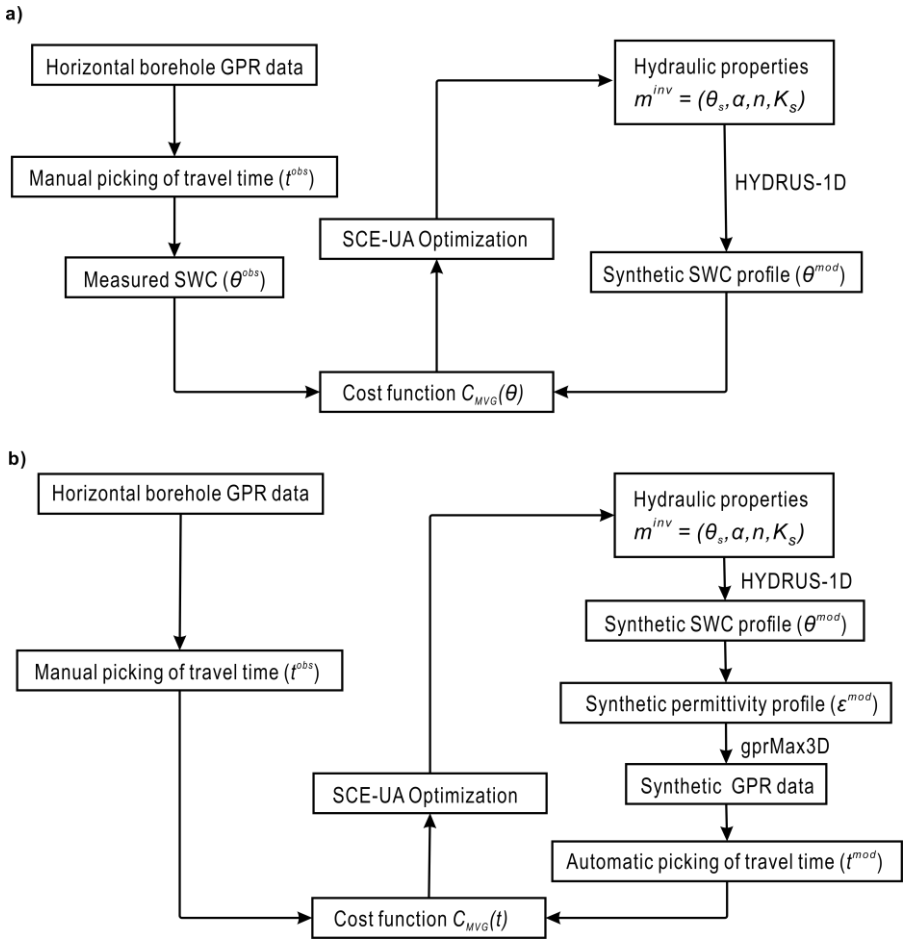

Fig. 3.2 Flow charts of (a) sequential inversion and (b) coupled inversion.

3.2.5 Set-up for synthetic infiltration experiments

Synthetic model experiments were performed to gain further insight into the feasibility of obtaining plausible parameter estimates from sequential and coupled inversion of time-lapse

borehole GPR data. In a first model experiment, a 1-layer soil profile was considered. I used the soil hydraulic parameters for the top soil (0 - 30 cm) determined by Cai et al. (2018a), which were estimated from TDR measurements at the same depths as the GPR access tubes (Table 3.2). In order to generate synthetic data for the model experiments, five infiltration events were simulated with an infiltration rate of 0.03 cm min^{-1}, which corresponds with the infiltration rate used in the actual field experiment. Since the 1-layer soil profile was constructed using the hydraulic parameters of the topsoil (higher θ_s), the amount of applied water was increased in the synthetic modelling experiment. In particular, the first three irrigation events now lasted 400 min whereas the last two infiltration events still lasted 90 min. After obtaining the SWC profile (θ^{mod}) from HYDRUS-1D, a dielectric permittivity profile ε^{mod} (-) was calculated using the rearranged form of the CRIM model given in Eq. 2.6:

$$\varepsilon^{mod} = [(\sqrt{\varepsilon_w} - 1) * \theta^{mod} + (1 - \Phi) * \sqrt{\varepsilon_s} + \Phi]^2 \quad (3.3)$$

This dielectric permittivity profile was then used to simulate GPR measurements for the six depths using gprMax3D.

A synthetic modelling experiment with a 2-layer soil profile was also performed. Sequential and coupled inversions for the 2-layer soil profile were conducted based on the infiltration schedule of the actual experiment (Fig. 3.1a). The hydraulic parameters in this second experiment were also based on Cai et al. (2018a). However, the saturated hydraulic conductivity of the subsoil (K_{s2}) was changed from 0.0004 cm min^{-1} reported by Cai et al. (2018a) to 0.04 cm min^{-1}, because it had to be larger than the infiltration rate of 0.03 cm min^{-1} to avoid ponding of water at the layer interface. For a more realistic synthetic modelling study, Gaussian noise with zero mean and a standard deviation of 0.1 ns and 0.01 cm^3 cm^{-3} was added to the synthetic travel times and SWC data, respectively, for both the 1-layer and the 2-layer model.

Table 3.2 Soil hydraulic parameters for the rhizotron facility

Depth	θ_r	θ_s	α	n	K_s	l
(cm)	(cm^{3}cm^{-3})	(cm^{3}cm^{-3})	(cm^{-1})	(-)	(cm min^{-1})	(-)
0 - 30	0.043	0.326	0.036	1.386	0.057	1.47
30- 120	0.053	0.229	0.050	1.534	0.0004†;0.04††	-2.78

† The K_s value of subsoil estimated by Cai et al. (2018a).
†† The K_s value used for synthetic study of 2-layer soil profile.

The implementation of the coupled inversion approach requires an automatic picking of the first arrival time. For the simulated GPR data, the first arrival time can be automatically determined using an amplitude threshold. To obtain this threshold, the excitation moment T_s (ns) of the simulated data was determined from the onset of the source wavelet. The source wavelet is

defined as the first derivative of the Gaussian waveform:

$$I = -2\zeta\sqrt{e^{\frac{1}{2\zeta}}}e^{-\zeta(t-\chi)^2}(t-\chi) \quad (3.4)$$

where $\zeta = 2\pi^2 f^2$ and $\chi = 1/f$, I is the electric current density (A m^{-2}), e (-) is the natural logarithm, and f (MHz) is the center frequency of the antenna (200 MHz). From this source wavelet, a T_s of 1.62 ns was manually determined (Fig. 3.3a). Subsequently, an air wave was simulated using antennas positioned at 0.1 m above the ground surface (Fig. 3.3b). With the known propagation velocity in air (0.3 m ns^{-1}) and the antenna separation (0.75 m), the true travel time of the air wave is 2.5 ns. The appropriate amplitude threshold (0.0158 V m^{-1}) was then determined from the amplitude of the simulated air wave at the travel time of 4.12 ns, which is the sum of T_s (1.62 ns) and true travel time of the air wave (2.5 ns).

To verify the robustness of the automatic first arrival time determination, a synthetic infiltration-induced SWC profile was generated by HYDRUS-1D (Fig. 3.3c) and ZOP measurements were simulated using gprMax3D at different depths. The amplitude threshold of 0.0158 V m^{-1} was used to determine the first arrival time (Fig. 3.3d). It was found that the amplitude of the traces rapidly increased after the determined first arrival time, which confirms the robustness of automatic procedure for the determination of the first arrival time.

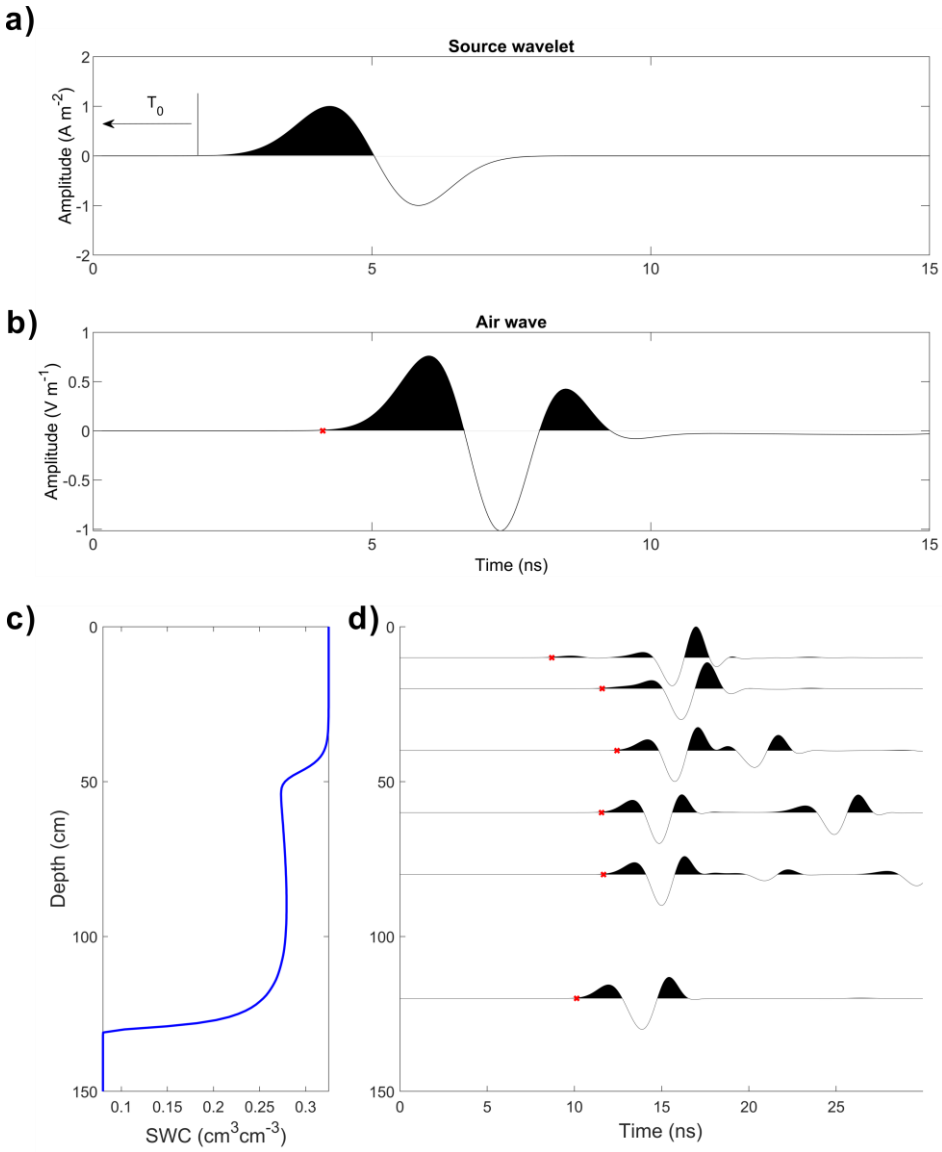

Fig. 3.3 (a) The source wavelet. (b) A synthetic trace of air wave generated by gprMax3D. (c) A synthetic vertical SWC profile generated by HYDRUS-1D. (d) Six synthetic GPR traces obtained using the synthetic vertical SWC distribution shown in (c). The red crosses indicate the first arrival time of the GPR traces.

3.2.6 Uncertainty analysis

Proper quantification of uncertainty in the estimated soil hydraulic parameters is of great importance given that the information content of soil water content measurements for the estimation of soil hydraulic properties depends on the initial and boundary conditions during the experiment (Mboh et al., 2011). In this study, I used both response surface analysis (Toorman et al., 1992) and a simple first-order approximation (Kool and Parker, 1988; Kuczera and

Mroczkowski, 1998; Vrugt and Dane, 2006) to investigate the uncertainty of the inverted hydraulic parameters.

Response surfaces provide a 2D view of the cost function distribution obtained with a grid search. In order to obtain such surfaces, two hydraulic parameters (e.g., α and n) are varied between defined bounds, whereas the other hydraulic parameters (e.g., log(K_s) and θ_s) are fixed at their true (or optimized) value. Response surfaces are a robust method to visualize parameter uncertainty and the minimum of the cost function. However, they commonly require a high computational effort, especially in the case of many model parameters (i.e., the 2-layer model). Therefore, this method was only used for the synthetic model study with a 1-layer soil profile.

A classic first-order approximation of parameter uncertainty was also used (Vrugt and Dane, 2006). It is based on the covariance matrix (C_v) of the optimized hydraulic parameters, which is calculated by:

$$C_v = s_v^2 (J^T J)^{-1} \tag{3.5}$$

where s_v^2 is the error variance between simulated and observed data and *J* is the Jacobian matrix. The Jacobian matrix is the first-order partial derivative of the cost function for each inverted hydraulic parameter and was obtained using a finite difference approach. The marginal posterior distribution of the estimated hydraulic parameters (m^{est}) is assumed to be a multivariate normal distribution $N(m^{est}, C_v)$. The uncertainty of the estimated hydraulic parameters can be approximated by the confidence interval for a given level (i.e., 99%) of significance calculated from the diagonal elements of C_v. A matrix (A) that provides the correlation between the estimated hydraulic parameters can be obtained by dividing the elements of C_v with the square root of the diagonal elements of C_v:

$$A_{ij} = \frac{C_{v_{ij}}}{C_{v_{ii}}^{1/2} C_{v_{jj}}^{1/2}} \tag{3.6}$$

This first-order approximation is an efficient way for estimating the uncertainty of the estimated hydraulic parameters for linear or nearly linear hydrologic models and the correlation matrix is a useful indicator of parameter correlation (Zhu and Mohanty, 2003). If the hydrological model is highly non-linear, the first-order approximation may be unreliable. Therefore, I only focus on A_{ij} values larger than 0.6 in our analysis.

3.3 Results and discussion

3.3.1 Synthetic infiltration experiments

The simulated vertical SWC profiles at times where GPR measurements were obtained are shown in Fig. 3.4 for the synthetic modelling study with a 1-layer soil. It can be seen that the infiltration front moved down to 0.6 and 1.2 m depth after the first and second infiltration event, respectively. After the third infiltration event, the entire soil profile was saturated. Because of the high saturation after the third infiltration event, the infiltration front moved rapidly downward through the entire soil profile during infiltration events 4 and 5.

The SWC estimates obtained from the first-arrival time of simulated horizontal borehole GPR measurements using a straight-wave approximation are also shown in Fig. 3.4b. It was found that SWC estimates obtained from GPR measurements at shallow depth (0 – 0.2 m) and near the infiltration front underestimated the actual SWC (Fig. 3.4b and 3.4c). This is attributed to the interference of the direct wave with critical refractions generated at the air – soil interface and the infiltration front where the dielectric permittivity changes sharply (Rucker and Ferré, 2004a). For this reason, horizontal borehole GPR measurements at 0.1 m depth were previously not considered for SWC estimation (Klotzsche et al., 2019a). In the synthetic study, these data were also not used in the sequential inversion to reduce this interpretation error. Unfortunately, errors in SWC estimates near the infiltration front cannot be simply identified and eliminated and thus are expected to affect the estimated hydraulic parameters obtained with the sequential inversion approach. For the coupled inversion, the effect of the air-soil interface is considered in the simulation of GPR wave propagation and therefore there is no need to remove the measurement at 0.1 m depth. However, the information content with respect to the soil hydraulic properties is expected to be limited for these measurements because of the limited travel path length in the topsoil.

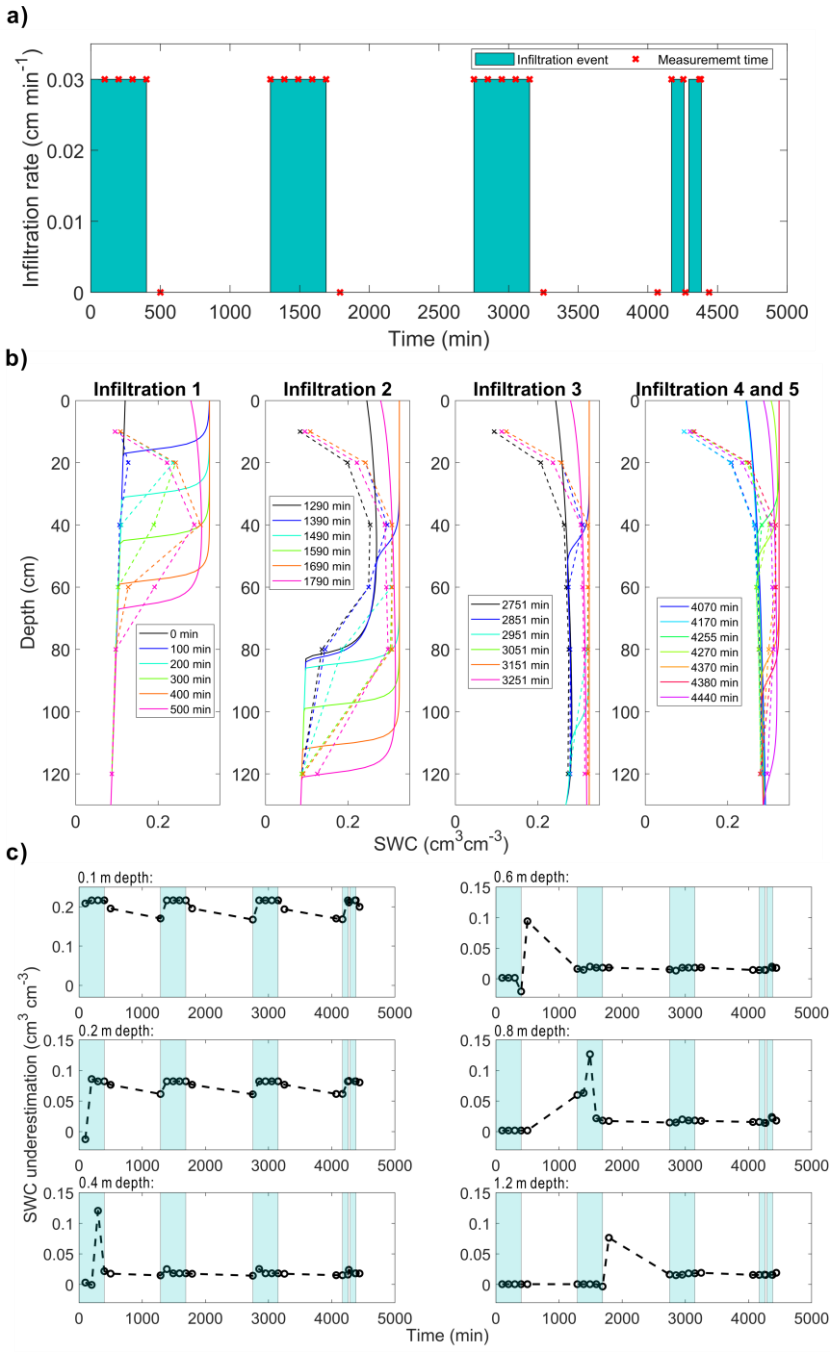

Fig. 3.4 (a) Schedule of the synthetic infiltration events and synthetic GPR measurements. (b) Synthetic vertical SWC profiles from HYDRUS-1D (solid lines) and synthetic vertical SWC profiles estimated by GPR data (dashed lines) based on the vertical water content distribution used as inputs in gprMax3D. The colors indicate different measurement times. The GPR estimated SWCs at 0.2 – 1.2 m depth were inverted using a sequential inversion approach to estimate the hydraulic parameters for the 1-layer soil. (c) Differences between GPR-estimated and simulated HYDRUS-1D SWCs. The timing of the infiltration events is indicated by the light green background. Note that different y-axis scales are used for the results of different depths.

Fig. 3.5a presents the response surface based on true SWC data that would be obtained using point measurements (i.e., TDR) at the same depth as the borehole GPR measurements. The corresponding response surfaces for the noise-free coupled inversion of the synthetic GPR data are shown in Fig. 3.5b. It can be seen that the cost functions for point and GPR measurements have a very similar misfit distribution. This is not unexpected given that point and GPR measurements provide a similar type of information, albeit with a different sampling volume (Klotzsche et al., 2019a).

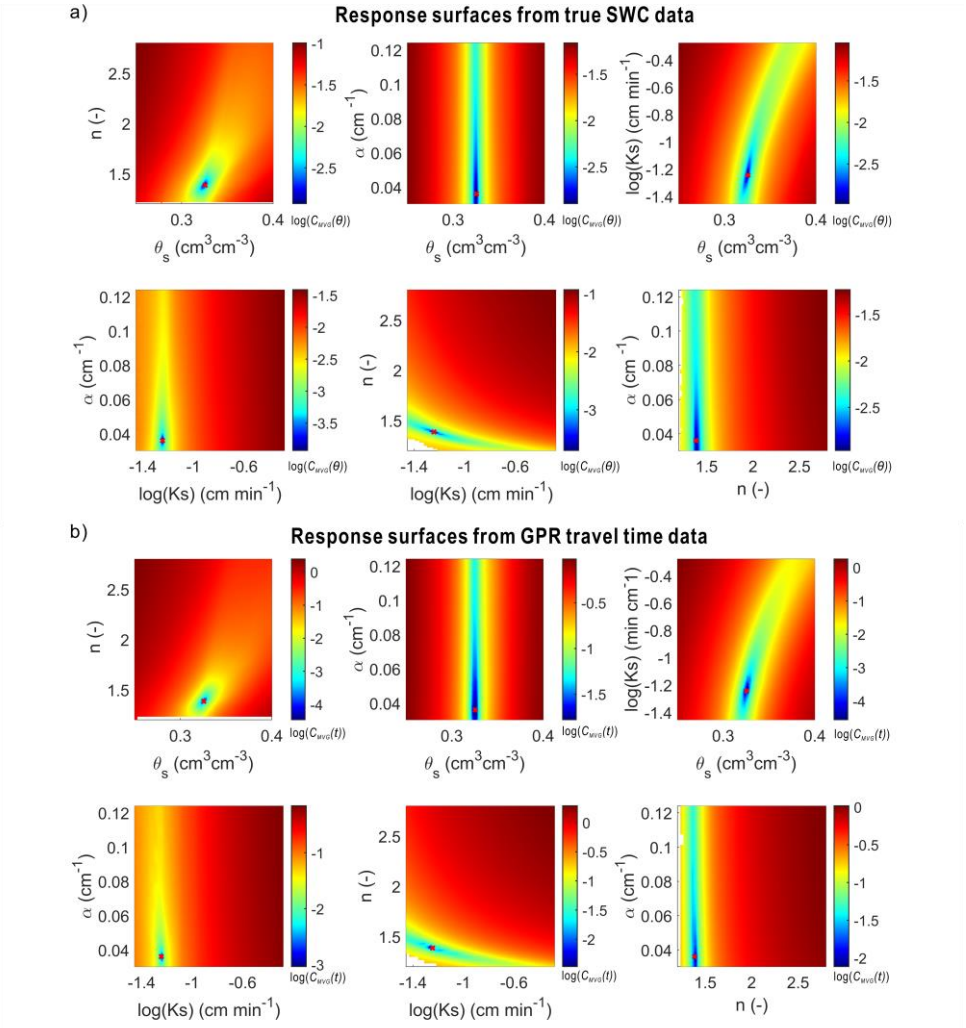

Fig. 3.5 Response surfaces for different pairs of hydraulic parameters obtained using (a) true SWC data simulated by HYDRUS-1D and (b) noise-free synthetic GPR travel times. The cost function values are shown in logarithmic scale. Blank spaces indicate that the hydrological model did not converge for the selected parameters. The global minimum of the cost function is shown by the red cross. Also note that the cost functions of sequential and coupled inversion ($C_{MVG}(\theta)$ and $C_{MVG}(t)$) have different units (cm^3cm^{-3} and ns, respectively).

The response surfaces can be used to gain insight in the expected parameter uncertainty. In the case of the α parameter, the response surfaces for $n - \alpha$, $\theta_r - \alpha$, and $\theta_s - \alpha$ indicate that changes in the cost function are parallel to the α axis. This suggests that the α parameter is independent from the other parameters. Although a clear minimum in the cost function value can be observed in these three surfaces, it is also elongated in the direction of the α axis suggesting that the α parameter is expected to be less constrained in the inversion results compared to the other model parameters. According to the response surfaces for $\theta_s - n$ and $\theta_s - \log(K_s)$, estimates of θ_s are expected to be correlated with the estimates of n and $\log(K_s)$. In the vicinity of the global minimum, the response surface is almost perpendicular to the θ_s axis and steep, which suggests that θ_s estimates are well-constrained during inversion. The global minimum in the response surface between $\log(K_s)$ and n is positioned in an elongated valley. A strong negative correlation between the parameter estimates for $\log(K_s)$ and n is thus expected, which implies that the GPR measurements may not contain sufficient information to simultaneously constrain both $\log(K_s)$ and n.

Sequential and coupled inversions were performed using noisy simulated GPR measurements for the 1-layer soil profile. In the case of the sequential inversion, the fitted SWC data showed a large misfit with the expected SWC (Fig. 3.6a), particularly for the shallow depths (0.2 m). This is also reflected in the large cost function value (0.05 $cm^3\ cm^{-3}$) for the optimized parameters, which is much higher than the added uncertainty in the SWC data (0.01 $cm^3\ cm^{-3}$). Additionally, the SWC profiles simulated by using the estimated parameters from the sequential inversion showed large deviation with the SWC profiles from the true forward model (Fig. 3.7a). Due to the poor fit to the data, the hydraulic parameters were not accurately estimated by the sequential inversion (Table 3.3). In particular, θ_s was strongly underestimated and this resulted in a large mismatch between the inverted and true water retention curves (Fig. 3.8a). Moreover, the estimated value for K_s was at the lower boundary of the feasible parameter space (0.035 cm min^{-1}), which is almost equal to the infiltration rate. The n and α parameters were also overestimated, which resulted in a large difference between the inverted and true relative hydraulic conductivity function (Fig. 3.8b). As detailed above, sequential inversion of ZOP data may lead to erroneous estimates of hydraulic parameters if strong vertical gradients in SWC are present (e.g., infiltration-induced gradients).

In the case of the parameters estimated from coupled inversion, the simulated travel time fitted the known travel time from the true model well (Fig. 3.6b) as expressed by the low RMSE of 0.1 ns. Also, the simulated SWC profiles matched well the SWC profiles from the true model (Fig.

3.7a). It should be noted that the coupled inversion was ended when the cost function value decreased to the standard deviation of the Gaussian noise (0.1 ns) (Table 3.3) to avoid overfitting. Therefore, the data simulated with the inverted model parameters have the same RMSE as the noise-free data and the simulated travel times based on the inverted parameters also match well with the noise-free data.

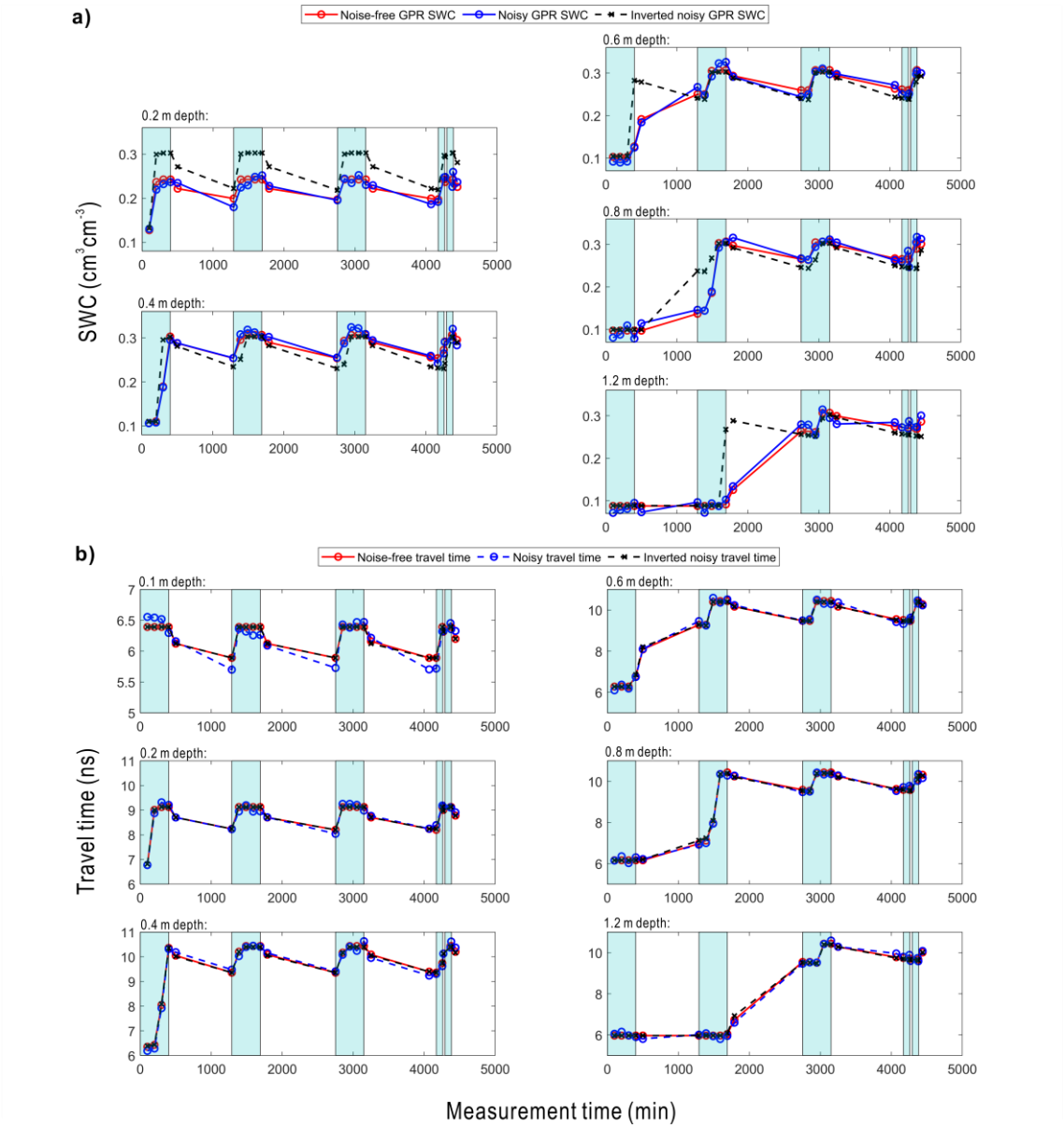

Fig. 3.6 (a) Sequential inversion results of noisy GPR SWC estimations. (b) Coupled inversion results of noisy GPR travel time data. SWC data at 0.1 m depth was not used for sequential inversion. The timing of the infiltration events is indicated by the light green background. Note that different y-axis scales are used to show the results for different depths.

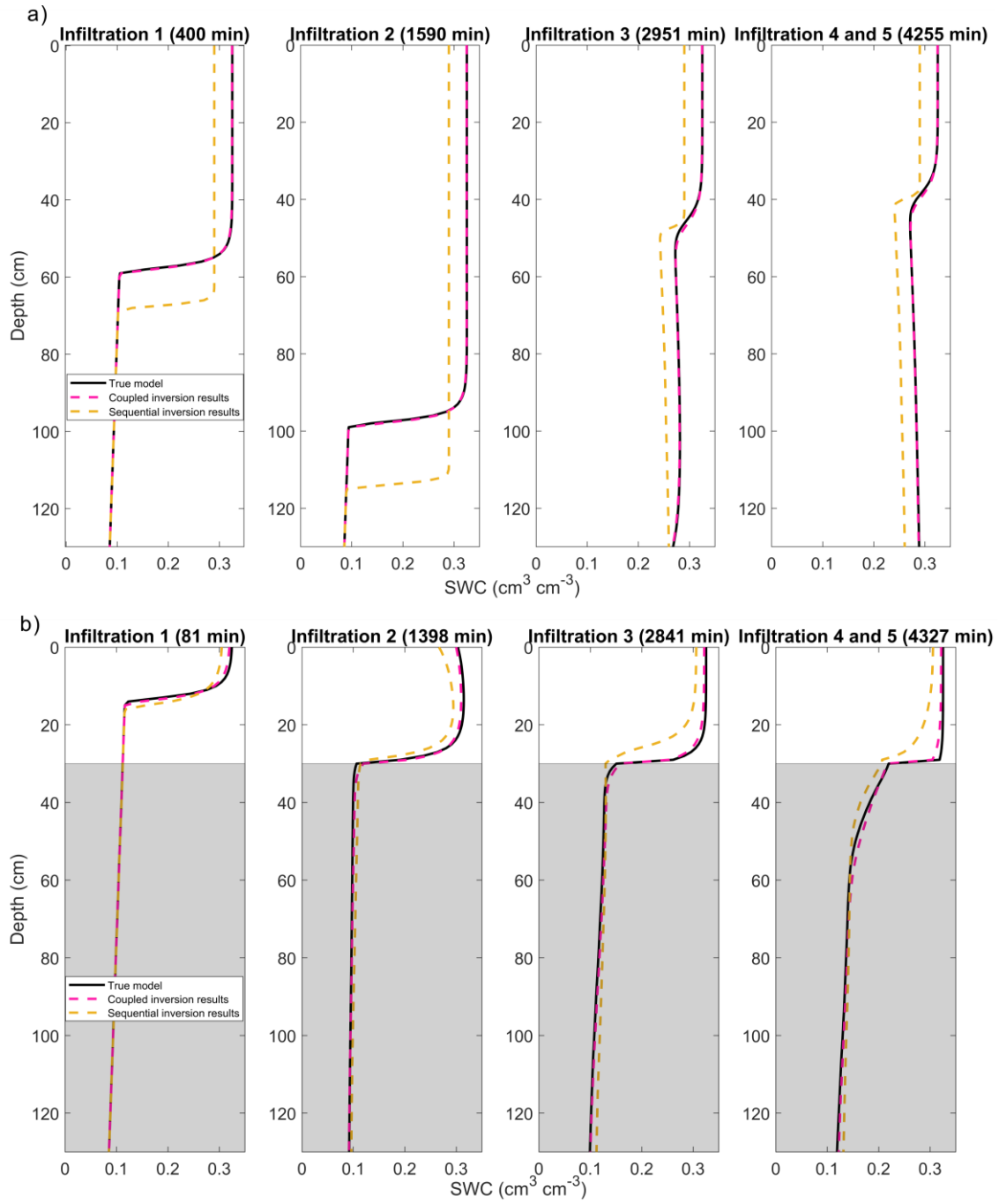

Fig. 3.7 Vertical SWC profiles of the (a) 1-layer and (b) 2-layer soil profile, which were simulated by using the true model (black solid line), parameters estimated from the coupled inversion (purple dashed line) and sequential inversion (yellow dashed line) at four different measurement times. Note that the different background indicates the different layers.

Table 3.3 Inverted results of noisy synthetic data

	True value	Bounds	Inverted results	
			Sequential inversion	Coupled inversion
		homogenous soil profile		
θ_s (cm^3cm^{-3})	0.326	0.25 – 0.40	0.290	0.326±0.001†
α (cm^{-1})	0.036	0.030 – 0.125	0.106	0.036±0.003
n (-)	1.386	1.1 – 2.8	1.431	1.358±0.016
$\log(K_s)$ (cm min^{-1})	-1.244	-1.456 – -0.276	-1.456	-1.168±0.038
Cost-function	-	-	0.05	0.1
		2-layer soil profile		
θ_{s1} (cm^3cm^{-3})	0.326	0.30 – 0.40	0.345	0.324±0.007
α_1 (cm^{-1})	0.036	0.030 – 0.125	0.036	0.036±0.004
n_1 (-)	1.386	1.1 – 2.8	1.506	1.312±0.024
$\log(K_{s1})$ (cm min^{-1})	-1.244	-1.456 – -0.276	-0.276	-0.996±0.048
θ_{s2} (cm^3cm^{-3})	0.229	0.15 – 0.30	0.300	0.240±0.007
α_2 (cm^{-1})	0.050	0.030 – 0.125	0.038	0.045±0.004
n_2 (-)	1.534	1.1 – 2.8	1.696	1.431±0.020
$\log(K_{s2})$ (cm min^{-1})	-1.398	-1.456 – -0.276	-1.456	-1.108±0.048
Cost-function	-	-	0.01	0.1

†The values indicated the 99% confidence interval based on the first-order approximation.

The values for θ_s and α were accurately estimated by coupled inversion (Table 3.3). However, the estimated values for n and $\log(K_s)$ showed a slight deviation from the true model, likely because of the strong correlation between these two parameters. The accurate estimation of the hydraulic parameters is also reflected in the good match between the estimated and known water retention and relative hydraulic conductivity function (Fig. 3.8a, 3.8b). The first-order uncertainty estimates for the coupled inversion are presented in Table 3.3 and the associated correlation matrix of the estimated hydraulic parameters is given in Table 3.4. The results indicate a strong negative correlation for $\log(K_s)$ - n and weak correlations between other pairs of hydraulic parameters. This is consistent with the results of the response surface analysis and confirms that the first-order approximation provides a meaningful assessment of parameter uncertainty.

In a next step, the synthetic modelling study for the 2-layer soil profile was analyzed. As expected from the results of the 1-layer soil profile, the parameters estimated using sequential inversion deviated considerably from the true hydraulic parameters (Table 3.3) and the estimated and true

water retention (Fig. 3.8c, 3.8e) and relative hydraulic conductivity functions did not match well (Fig. 3.8d, 3.8f). Hence, sequential inversion will not be considered for the analysis of the actual field measurements.

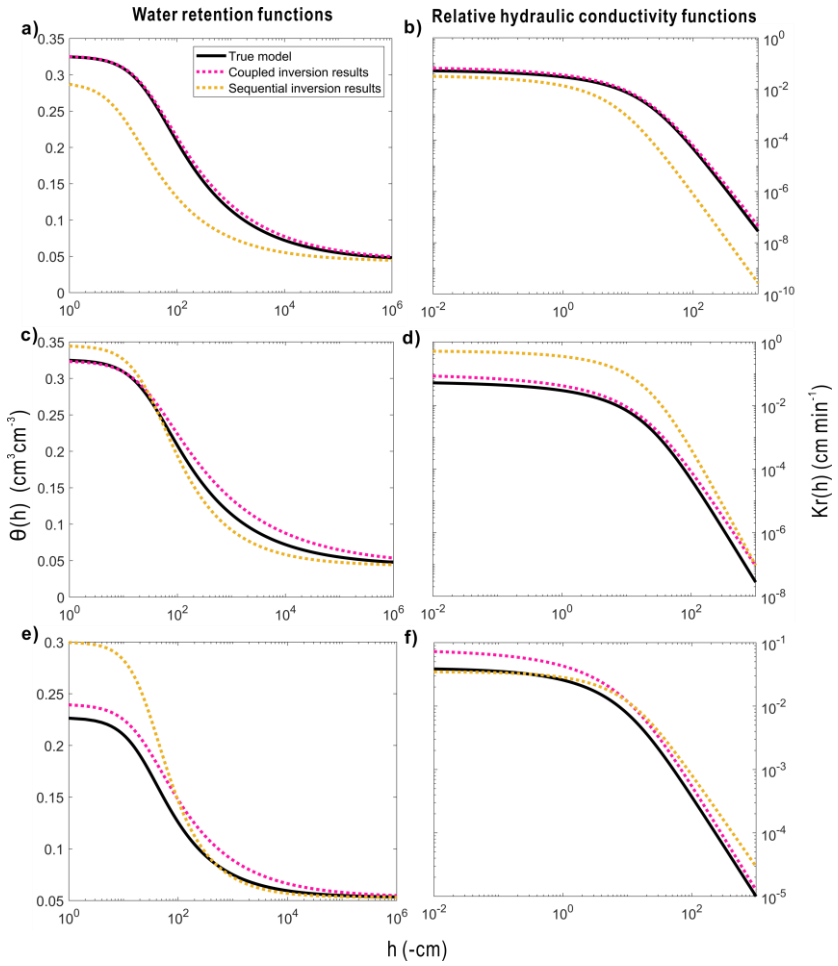

Fig. 3.8 Water retention $\theta(h)$ and relative hydraulic conductivity $K_r(h)$ function for the (a,b) synthetic homogeneous soil profile, and the (c,d) topsoil and (e,f) subsoil of the 2-layer profile.

Table 3.4 Correlation matrix of the estimated hydraulic parameters for the homogeneous profile

	α (cm^{-1})	n (-)	$\log(K_s)$ ($cm\ min^{-1}$)	θ_s (cm^3cm^{-3})
n	-0.335	1		
$\log(K_s)$	0.233	-0.694†	1	
θ_s	-0.086	0.256	0.186	1

†The values indicated the pairs of parameters showing strong correlation.

The results of the coupled inversion for the 2-layer soil profile generally were consistent with the results of the 1-layer profile, despite the dimensional expansion of the search space from four to eight parameters. Again, the estimated travel times from coupled inversion results nicely fitted the noisy synthetic travel time series (Fig. 3.9) and the vertical SWC profiles from the true model (Fig. 3.7b). In addition, accurate hydraulic parameter estimates were obtained (Table 3.3), as also confirmed by the minor differences in estimated and true water retention (Fig. 3.8c, 3.8e) and relative hydraulic conductivity functions (Fig. 3.8d, 3.8f).

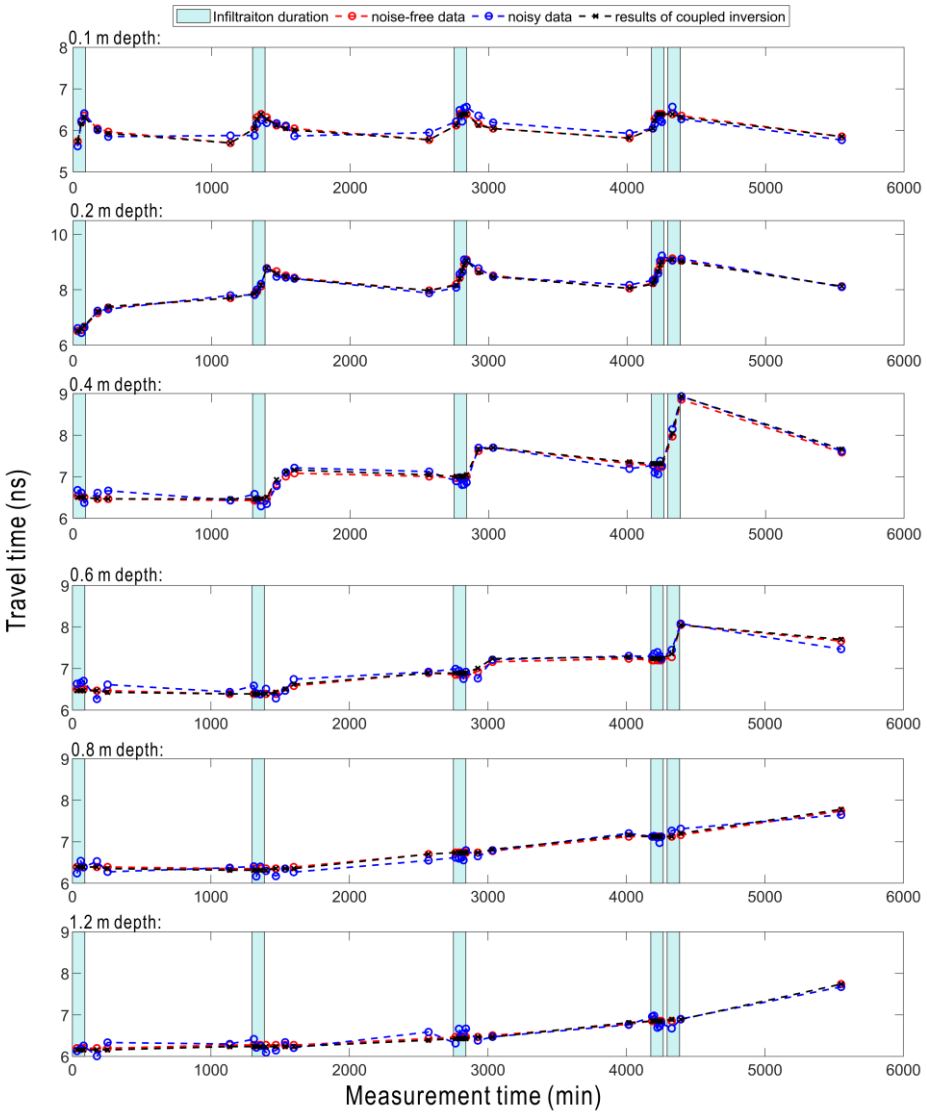

Fig. 3.9 Coupled inversion results of noisy GPR travel time data for 2-layer profile. The timing of the infiltration events is indicated by the light green background. Please note that results for different depths are shown with difference range of y-axis scale.

3.3.2 Inversion of experimental GPR data

Coupled inversion was used to estimate the hydraulic parameters from the measured horizontal borehole GPR data shown in Fig. 3.10. The resulting fit to the measured data is also shown in Fig. 3.10 and the estimated soil hydraulic parameters are provided in Table 3.5. For comparison, the simulated data using the hydraulic parameters of Cai et al. (2018a) are also provided, which are based on long-term TDR measurements also made during vegetation periods.

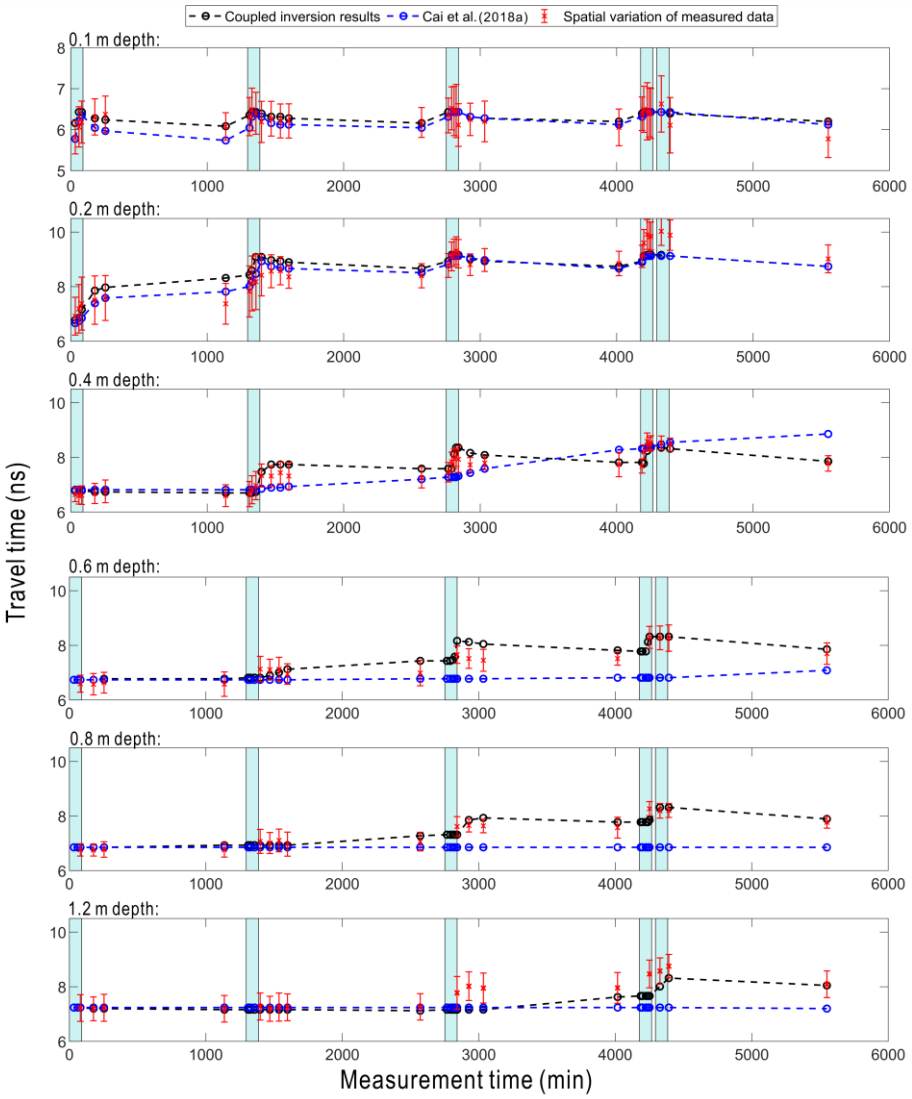

Fig. 3.10 Coupled inversion results of measured GPR travel time data at different depths. Simulated travel time using the hydraulic parameters of Cai et al. (2018a) and inverted model are shown in blue and black dashed lines, respectively. The timing of infiltration events is indicated by the light green background. Please note that different y-axis scales are used for the results at different depths.

The comparison between measured and simulated travel times showed a good correspondence at 0.1 m depth both for the inverted hydraulic parameters and the parameters from Cai et al. (2018a) (Fig. 3.10). For 0.2 m depth, the measured GPR travel times steadily increased during the entire infiltration experiment, whereas the simulated travel times using both sets of hydraulic parameters remained constant after the second infiltration event because the soil reached saturation. This can be explained by the heterogeneous nature of the topsoil, which is supported by the large spatial variation of the GPR travel time data. For the subsoil, the key features of the measured time-lapse GPR data were well captured by the coupled inversion, also considering the spatial variability in the measured GPR data. The simulated travel time data based on the hydraulic parameters of Cai et al. (2018a) did not match the observed GPR data well in the subsoil (i.e., at 0.6, 0.8, and 1.2 m depth). This is attributed to the small K_{s2} used in Cai et al. (2018a), which results in a slow movement of the infiltration front in the subsoil (Fig. 3.11), and therefore, a reduced variation in simulated water content at large depths.

Table 3.5 Inverted Soil hydraulic parameters for the rhizotron facility from measured GPR data.

Depth (cm)	θ_r (cm^3cm^{-3})	θ_s (cm^3cm^{-3})	α (cm^{-1})	n (-)	$\log(K_s)$ ($cm\ min^{-1}$)	l (-)
		[cost-function = 0.32 (ns)]				
0 – 30	0	0.328±0.011†	0.032±0.011	1.125±0.028	-0.983±0.266	0.5
30 - 120	0	0.196±0.009	0.038±0.015	1.202±0.054	-1.022±0.349	0.5

†The values indicated the 99% confidence interval based on the first-order approximation.

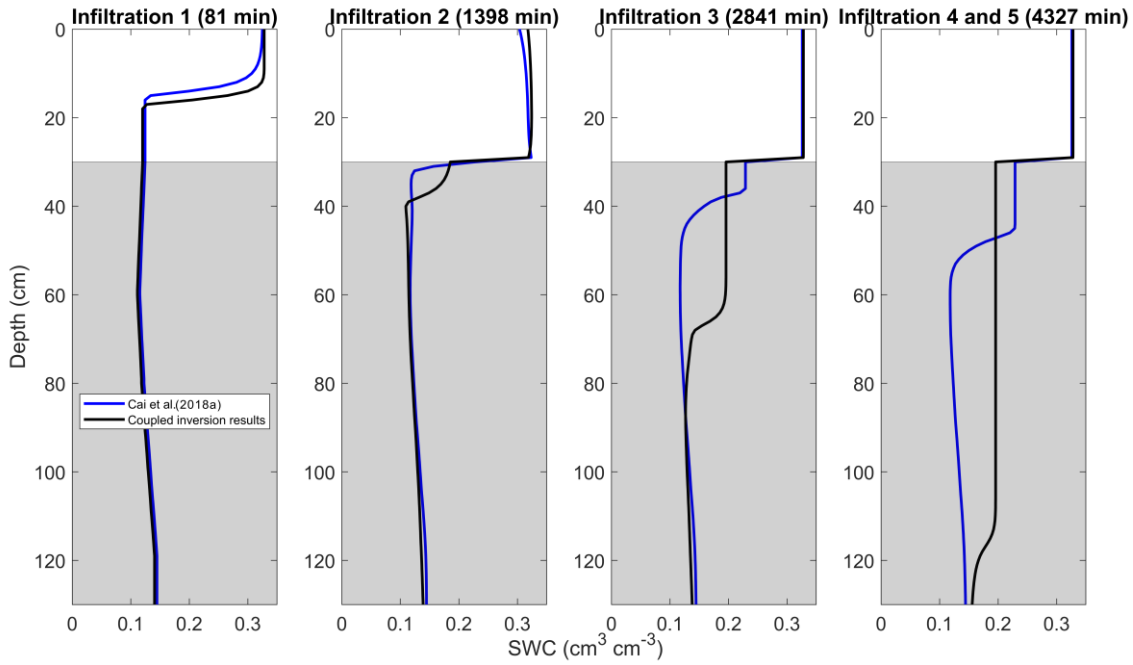

Fig. 3.11 Vertical SWC profiles simulated by using hydraulic parameters from the inversion of measured data (black lines) and Cai et al. (2018a) (blue lines). Note that the different backgrounds indicate the different soil types.

Measured and inverted GPR travel time data are directly compared in Fig. 3.12. The use of the hydraulic parameters from Cai et al. (2018a) clearly resulted in a systematic underestimation of the measured data and a relatively high RMSE of 0.43 ns. The hydraulic parameters obtained using coupled inversion better matched the measured travel time data, as indicated by the lower RMSE (0.32 ns) and a higher R^2 value (0.90). Nevertheless, the RMSE between inverted and measured GPR data is still relatively large. This is partly attributed to the heterogeneity of the topsoil, as the measurements at 0.2 m depth make up a considerable part of the observed misfit. Furthermore, there is uncertainty in the initial SWC profile, which is solely based on GPR measurements at six different depths. Here, extrapolation from the shallowest borehole to the soil surface is problematic, and may have introduced some degree of uncertainty. Finally, there is intrinsic uncertainty in the field GPR measurements and data processing, such as the uncertainty in the position of the horizontal boreholes and the uncertainty in the determination of the time-zero or first arrival time of measured GPR data. These issues obviously did not affect the coupled inversion in the synthetic case study but they are highly relevant for the inversion of actual field measurements.

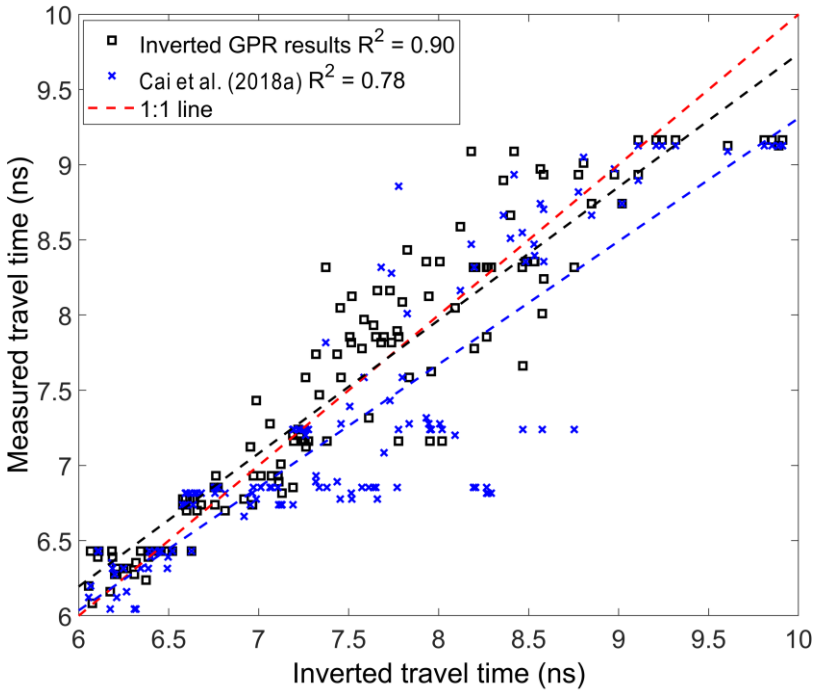

Fig. 3.12 Linear regression between measured and GPR travel time data obtained using the inverted hydraulic parameters (black squares) and the hydraulic parameters of Cai et al. (2018a) (blue crosses). The 1:1 line is indicated by the dashed red line.

The results of the first-order uncertainty estimation of the inverted hydraulic parameters are provided in Table 3.5. The uncertainty of α and θ_s are comparable for the top- and subsoil, whereas n and $\log(K_s)$ showed a larger uncertainty for the subsoil. This can be explained by the strong negative correlation (A = -0.615) between n_2 and $\log(K_{s2})$ (Table 3.6). All other pairs of hydraulic parameters did not show strong correlations. Fig. 3.13 presents the water retention and relative hydraulic conductivity functions obtained using coupled inversion. The associated uncertainty was obtained by randomly plotting 100 sets of hydraulic parameters drawn from the uncertainty bounds provided in Table 3.5. As can be seen from the uncertainty bounds, θ_s is associated with a relatively low uncertainty, whereas the n value is associated with a larger uncertainty as indicated by the increasing spread of the functions at lower pressure heads. Furthermore, uncertainty in the water retention function is similar for the top- and subsoil (Fig. 3.13a, 3.13c). For comparison, the functions based on the hydraulic parameters of Cai et al. (2018a) were also provided. The water retention function obtained using coupled inversion clearly deviated from that of Cai et al. (2018a), which showed a faster decrease of water content with matric potential due to the larger n value. Additionally, a lower θ_s was estimated by the coupled inversion.

Table 3.6 Correlation matrix of the inverted hydraulic parameters for the 2-layer model

	α_1 (cm^{-1})	n_1 (-)	$\log(K_{s1})$ (cm min^{-1})	α_2 (cm^{-1})	n_2 (-)	$\log(K_{s2})$ (cm min^{-1})	θ_{s1} (cm^3cm^{-3})	θ_{s2} (cm^3cm^{-3})
n_1	-0.388	1						
$\log(K_{s1})$	0.324	0.045	1					
α_2	-0.077	0.129	0.138	1				
n_2	-0.119	-0.139	-0.163	-0.069	1			
$\log(K_{s2})$	0.061	-0.059	-0.046	0.549	-0.615†	1		
θ_{s1}	-0.032	-0.226	0.189	0.040	-0.087	0.049	1	
θ_{s2}	-0.058	-0.347	-0.192	-0.083	0.404	0.070	-0.192	1

†The values indicated the pairs of parameters showing strong correlation.

The hydraulic conductivity functions obtained using coupled inversion also showed a similar uncertainty for the top- and subsoil (Fig. 3.13b, 3.13d). For the topsoil, the hydraulic conductivity function obtained using coupled inversion corresponded well with the function obtained in Cai et al. (2018a). This is at least partly due to the similarity in the inverted K_s obtained in this study and in Cai et al. (2018a). However, there are obvious differences in the hydraulic conductivity functions for the subsoil due to differences in estimated K_s. There is a range of possible explanations for the observed differences. First, the estimation of K_s is known to be scale-dependent. For example, laboratory methods using small sample volumes often lead to lower K_s compared to estimates from in-situ measurement from a larger soil volume (Busch et al., 2013; Rovey II and Cherkauer, 1995). The results of Cai et al. (2018a) were based on TDR measurement that only cover a small areal fraction of the rhizotron facility, whereas the GPR measurements represent a larger volume (Klotzsche et al., 2019a). Thus, a higher K_s is perhaps expected for the GPR measurements since the importance of preferential flow in macropores likely increased from the TDR to the GPR scale. The analysis presented here also indicated potential parameter correlations between K_s and n. Since larger n values were reported by Cai et al. (2018a), this may explain the small K_s values. It is also important to note that Cai et al. (2018a) estimated hydraulic parameters with a more complex model set-up that considered root water uptake. In particular, root water uptake parameters were estimated alongside the hydraulic parameters, which might have hampered the correct estimation of the soil hydraulic parameters and likely increased the uncertainty in the estimated hydraulic parameters obtained by Cai et al. (2018a). Finally, it is important to note that Cai et al. (2018a) assumed free drainage as a lower boundary condition whereas a seepage face was used in this study.

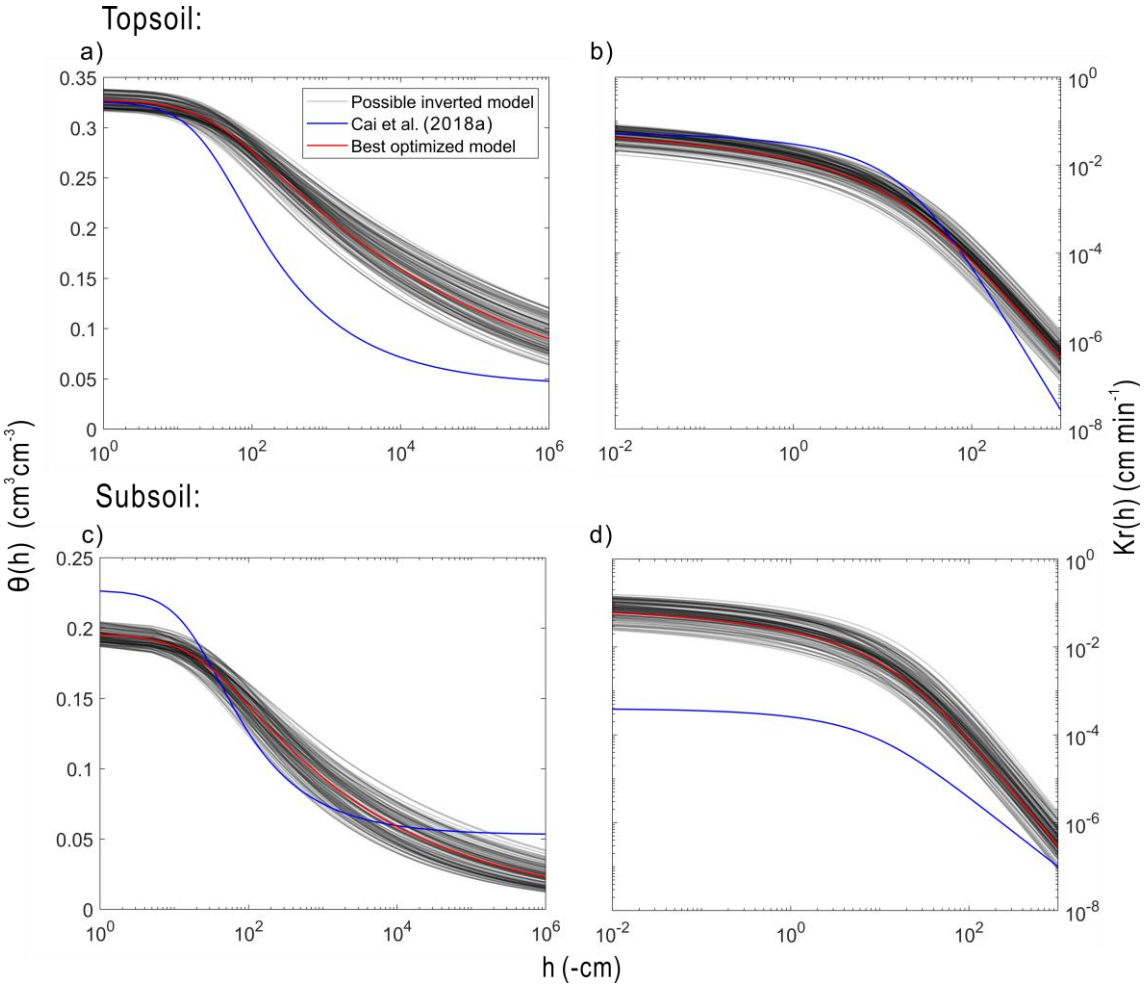

Fig. 3.13 Water retention $\theta(h)$ and relative hydraulic conductivity $K_r(h)$ function from 100 possible inverted hydraulic parameter sets (dark lines), the hydraulic parameters of Cai et al. (2018a) (blue line) and the hydraulic parameters with the best fit (red line) for the (a, c) top soil and (b, d) subsoil.

3.4 Summary and conclusions

In this chapter, I used both sequential and coupled inversion strategies to estimate hydraulic parameters from horizontal borehole GPR measurements during an infiltration experiment. First, a synthetic modelling study was set-up to compare the two inversion approaches independent of measurement and model errors. In a noise-free synthetic study using a 1-layer soil profile, a response surface analysis was used to evaluate correlation between hydraulic parameters. The results showed that the hydraulic parameters n and $\log(K_s)$ were strongly correlated, which implies that the GPR measurements were not able to simultaneously constrain $\log(K_s)$ and n. In a next step, synthetic SWC and travel time data with added noise were used to estimate hydraulic

parameters using sequential and coupled inversion approaches, respectively. It was observed that a sequential inversion approach relying on the conventional straight-ray approximation to estimate SWC did not provide accurate hydraulic parameter estimates if strong vertical gradients in SWC were present due to infiltration. The coupled inversion approach, which combined 3D modelling of GPR measurements with a 1D vadose zone flow model, was able to provide accurate estimates of the hydraulic parameters both for a 1-layer and a 2-layer soil profile because interpretation errors associated with the straight-ray approximation were avoided. In a final step, horizontal borehole GPR measurements made during an infiltration experiment were inverted using a coupled inversion approach. The estimated hydraulic parameters were reasonably consistent with water retention and relative hydraulic conductivity functions reported by Cai et al. (2018a) for the same site.

In conclusion, the coupled inversion of horizontal borehole GPR measurements provided accurate field-scale estimates of soil hydraulic parameters. Because of the larger sampling volume compared to point sensors, the estimated hydraulic parameters are expected to have an improved field representativeness. In future studies, coupled inversion of horizontal borehole GPR data may be used to estimate 2D and perhaps even 3D distributions of soil hydraulic parameters by considering all measured travel times over the profile, although this will obviously be associated with a higher computational effort. A disadvantage of the proposed approach is that GPR measurements are still taken manually and are thus time-consuming, whereas point sensors often allow automated data acquisition. As an alternative to GPR, other geophysical methods such as ERT can also be employed to estimate hydraulic parameters. ERT can investigate the subsurface with high resolution, and data acquisition can be automated. However, the electrical conductivity distribution obtained with ERT is not only sensitive to SWC but also depends on several other factors (e.g., clay content, pore water salinity) (Binley et al., 2015). This can complicate vadose zone model parameterization using ERT measurements considerably. It would be interesting to extend coupled inversion by considering the full GPR waveform instead of solely using travel time information, as was recently proposed for seismic data by Li et al. (2020). It is expected that this would increase the information content of the GPR measurements in the inversion, and therefore reduce uncertainty in the estimated hydraulic parameters and provide chances to estimate hydraulic properties of multi-layer soils.

CHAPTER 4 COUPLED FULL WAVEFORM INVERSION OF HORIZONTAL BOREHOLE GROUND PENETRATING RADAR DATA TO ESTIMATE SOIL HYDRAULIC PARAMETERS: A SYNTHETIC STUDY[3]

The coupled inversion approach has been introduced as an effective technique to characterize soil hydraulic properties based on time-lapse geophysical measurements. As shown in Chapter 3, it has been successfully used to estimate the soil hydraulic properties for the Selhausen test site using GPR travel time data. There may be room for further improvement of the coupled inversion approach by extending it to coupled full waveform inversion (CFWI) of GPR data. This topic is explored in this chapter using a synthetic modelling study with a 2-layer soil profile with unknown layer depth.

4.1 Introduction

Borehole GPR data are conventionally processed by using ray-based inversion approaches (e.g., Irving et al., 2007), which only provide velocity and attenuation information obtained from the first arrival times and first cycle amplitudes of the GPR data, respectively. Such approaches generally have a limited resolution for subsurface characterization because only a small amount of the data is considered. Therefore, ray-based inversions have difficulty to provide images that resolve small-scale high-contrast layers, such as high-porosity zones that form preferential flow paths in aquifer systems or impermeable clay lenses (Klotzsche et al., 2019b). In contrast, full-waveform inversion (FWI) of GPR data takes the entire measured signal into account, including reflections and refractions, and is therefore able to provide more accurate and spatially higher resolved permittivity and electrical conductivity images than ray-based methods. The FWI method was first proposed by Tarantola (1984) for seismic data. FWI of seismic data has been further developed since then and is currently widely used (e.g., Berkhout, 2012; Brossier et al., 2009; Vigh and Starr, 2008). A comprehensive overview of FWI developments and applications is provided by Virieux and Operto (2009). Because of the similarity between seismic and GPR data, FWI has also been used for analyzing off-ground (Lambot and Andre, 2014), surface (Busch

[3]Adapted from Yu, Y., Huisman, J.A., Klotzsche, A., Vereecken, H., Weihermüller, L., 2021, Coupled full waveform inversion of horizontal borehole ground penetrating radar data to estimate soil hydraulic parameters: a synthetic study, in preparation.

et al., 2014), and borehole GPR data (Klotzsche et al., 2019b) to obtain high-resolution information on the spatial distribution of both ε and σ. The application of FWI for off-ground and surface GPR has mainly focused on estimating the properties of simplified models with a limited number of unknowns, such as layered media (Busch et al., 2012; Ihamouten et al., 2019) or cylindrical objects (Liu et al., 2018) in the subsurface. In contrast, FWI of vertical borehole GPR data uses a gradient-based inversion algorithm to obtain high resolution subsurface images (Gueting et al., 2017; Klotzsche et al., 2010; Klotzsche et al., 2014; Looms et al., 2017). For FWI of horizontal borehole GPR data, so far only a preliminary study was performed by Klotzsche et al. (2016) to invert ε and σ for a 2-layer soil profile of the Selhausen test site from ZOP data (see Section 2.2.1). As indicated in Chapter 2, the measured data for shallow boreholes (e.g., 0.1 m depth) is difficult to interpret due to the interference of the direct ground wave and the critically refracted air wave at the soil-air interface. The approach of Klotzsche et al. (2016) applied the FWI based on a SCE-UA optimization to retrieve the soil permittivity and conductivity for shallow boreholes by considering the wave interactions at the interface. This approach worked well with synthetic GPR data but is still challenging to apply to measured GPR data, because it is difficult to estimate an efficient source wavelet from a single ZOP trace.

To estimate soil hydraulic properties from time-lapse geophysical data, a coupled inversion approach can be used (e.g., Hinnell et al., 2010; Huisman et al., 2010; Lambot et al., 2006b; Mboh et al., 2012). Compared to a traditional sequential inversion approach where the hydrological model is inverted with SWC information estimated from geophysical data, coupled inversion is recognized as a more reliable and advanced approach that directly assimilates the geophysical data and therefore avoids interpretation errors from data processing. In Chapter 3, coupled inversion was applied successfully to GPR travel times to estimate the soil hydraulic parameters. Since GPR waveforms are expected to contain more information about the subsurface than GPR travel times, it is anticipated that the combined use of coupled inversion and FWI (i.e., coupled full waveform inversion, CFWI) is potentially able to provide soil hydraulic parameter estimates with less uncertainty. Up to now, there are only a few studies that have reported the use of CFWI to estimate hydraulic parameters from time-lapse off-ground GPR measurements (Lambot et al., 2009) or synthetic seismic data (Li et al., 2020). However, until now, no studies have been conducted that applied CFWI to borehole GPR data for parameterizing hydrological models.

This chapter aims to investigate potential benefits and shortcomings of a coupled full-waveform inversion (CFWI) for estimating soil hydraulic parameters and layer thickness for a 2-layer profile using synthetic horizontal borehole GPR data. First, a workflow of the CFWI will be proposed.

Next, an efficient synthetic infiltration experiment will be designed to simulate SWC and GPR data. Afterwards, parameter correlations between hydraulic parameters and layer thickness for the CFWI will be analyzed. Finally, CFWI will be applied to the synthetic data and the inversion results will be compared with the results from coupled inversion of GPR travel times.

4.2 Method and material

4.2.1 Set-up of the coupled full waveform inversion

To estimate soil hydraulic parameters and soil layer thickness for a 2-layer soil profile, the following CFWI set-up is used (Fig. 4.1). The set-up is similar to those shown in Fig. 3.2 for the sequential inversion and coupled inversion based on GPR travel times. Compared to the latter approach, the main difference is that CFWI directly optimizes the misfit between measured E^{obs} (V m^{-1}) and simulated waveforms E^{mod} (V m^{-1}) in the time domain instead of the first arrival times. For the coupled inversion of travel times, it was assumed that the effects of soil electrical conductivity could be neglected, which is reasonable given that the first arrivals of GPR data are not sensitive to the soil electrical conductivity. In contrast, soil electrical conductivity should be considered for GPR modelling in CFWI, since the soil electrical conductivity influences the attenuation, and thus, the amplitude of the GPR waveform. The distribution of the electrical conductivity can be reasonably obtained from the distribution of SWC(θ) and a petrophysical relationship, e.g., Archie's law (Archie, 1942):

$$\sigma^{mod} = \frac{1}{k_a}\,\sigma_w \Phi^{m_a}\left(\frac{\theta}{\Phi}\right)^{n_a} \tag{4.1}$$

where σ^{mod} (S m^{-1}) is the bulk soil conductivity used for GPR modelling, σ_w is the conductivity of the water (assumed to be 0.0519 S m^{-1} here), Φ (cm^3 cm^{-3}) is the porosity of the respective layer (Table 3.1), k_a (-) is a tortuosity constant, m_a (-) is the cementation exponent and n_a (-) is the saturation exponent. In this case, k_a, m_a, and n_a are assumed to be 1, 2, and 2, respectively, as suggested by Huisman et al. (2010).

The cost function $C_{MVG}(E)$ (V m^{-1}) in CFWI consists of the RMSE between the synthetic and measured electrical fields:

$$C_{MVG}(E) = \sqrt{\frac{\sum_{i=1}^{n_e}(E_i^{mod} - E_i^{obs})^2}{n_e}} \tag{4.2}$$

where n_e (-) is the number of the electric field points in the synthetic GPR data. It should be noted, that simulated GPR waveforms commonly contain more electric field points than measured GPR waveforms. To ensure that the measured and synthetic data are of the same size,

either the measured GPR data can be interpolated, or the simulated data can be resampled.

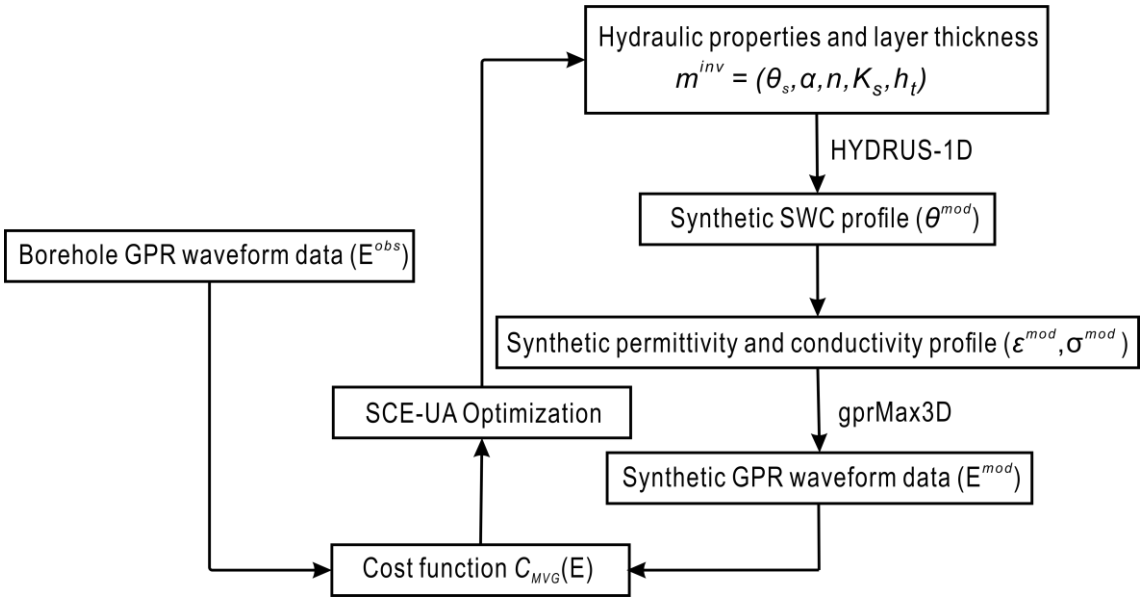

Fig. 4.1 Flowchart of the coupled full waveform inversion (CFWI) method.

4.2.2 Set-up for synthetic infiltration experiment

A synthetic case study is used to investigate the feasibility of obtaining plausible hydraulic parameter estimates for a 2-layer profile by using CFWI. The results of CFWI will be compared to results obtained with coupled inversion of GPR travel times as a reference. As in previous chapters, the hydraulic parameters determined by Cai et al. (2018a) were used to generate synthetic SWC profiles (Table 3.2). The infiltration experiment described in Chapter 3 (Fig. 3.1a) showed that coupled inversion of time-lapse borehole GPR travel time data can provide plausible parameter estimates. In this chapter, the infiltration experiment was modified to improve the modelling efficiency by reducing the number of required simulations. In particular, horizontal borehole GPR data were simulated for three depths only (0.2, 0.4, and 0.6 m depths) because the GPR data for 0.1 m depth were less informative (Chapter 3). Moreover, it is unnecessary to obtain GPR data at 0.8 and 1.2 m depths to estimate the hydraulic parameters for a 2-layer soil profile with a layer boundary at 0.3 m depth. With this reduction of measurement depths, less water needed to be supplied and the number of GPR measurements and the duration of the infiltration event could be reduced. The schedule of the modified infiltration experiment is shown in Fig. 4.2a. It uses the same infiltration rate (0.03 cm min^{-1}) as in Chapter 3, but it now considers a single 6-hour infiltration event (360 min) followed by a 90-min period with soil water redistribution without infiltration. GPR data were simulated every 30 min at all three depths. The set-up for

hydrological modelling was identical to the set-up used in Chapter 3 (see Section 3.2.2). Due to the reduction in the number of measurement depths, the size of the modelling domain for GPR simulations could also be reduced. The size of the simulation domain for the gprMax3D simulations was now set to 2 x 1.5 x 1.5 m, including a soil profile of 0.8 m thickness. The other settings for gprMax3D (e.g., grid size, source wavelet) were as described in Section 3.2.3.

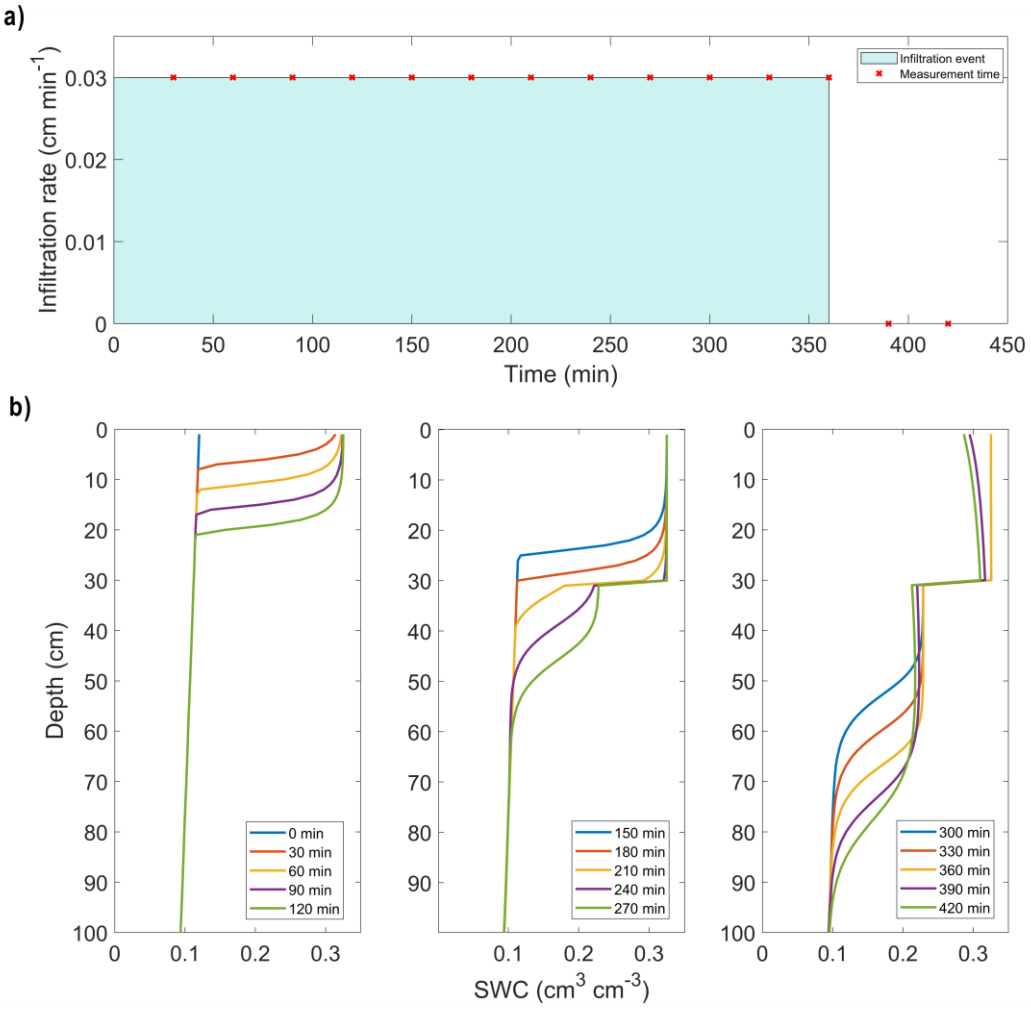

Fig. 4.2 (a) Schedule of the infiltration experiment and synthetic GPR measurements. (b) Synthetic vertical SWC profiles obtained with HYDRUS-1D at the time of the GPR measurements obtained with the hydraulic parameters provided in Table 3.2.

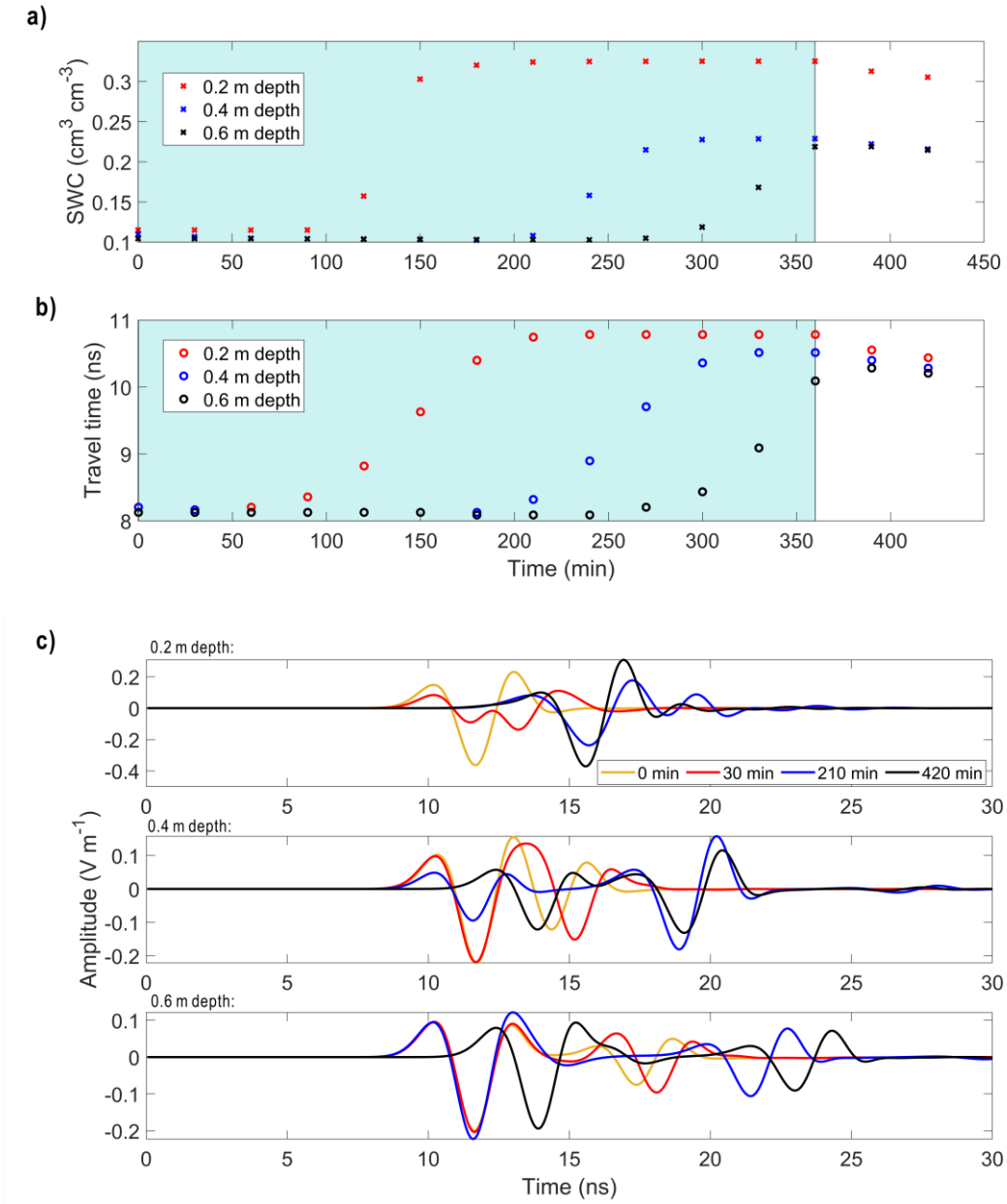

Fig. 4.3 (a) Synthetic time-lapse SWC data at 0.2, 0.4, and 0.6 m depths. (b) GPR travel times obtained from synthetic GPR data based on vertical water content distributions used as inputs in gprMax3D. (c) Synthetic GPR waveform data obtained at 3 different measurement times. The timing of the infiltration events is indicated by the light green background.

The synthetic vertical SWC profiles at times when GPR measurements were conducted are shown in Fig. 4.2b. It can be seen that the infiltration front reached the layer boundary at a depth of 30 cm after 180 min. At the end of the infiltration event (360 min), the upper 0.6 m of soil was saturated and the infiltration front moved to 0.8 m depth. After the infiltration stopped, the infiltration front still moved down to a depth of 0.9 m and the SWC above 0.6 m depth slightly

decreased due to redistribution. The synthetic time-lapse SWC data at 0.2, 0.4, and 0.6 m depths are shown in Fig. 4.3a. The soil at 0.2 and 0.4 m depth reached saturation after 200 and 300 min, respectively. After obtaining the synthetic SWC profiles, the dielectric permittivity profiles used for GPR modelling were obtained using the CRIM model (Eq. 2.6) and the electrical conductivity profiles were obtained using Eq. 4.1. These dielectric permittivity and electrical conductivity profiles were used to obtain synthetic GPR data with gprMax3D, which were then used to determine the GPR first arrival time data (Fig. 4.3b). The approach for automatic picking of the GPR first arrival times is described in Section 3.2.5. A comparison of Fig. 4.3a and Fig. 4.3b shows that the synthetic time-lapse SWC data and GPR travel time data have synchronous dynamics during the entire experiment.

The GPR waveforms simulated before (0 min), at the beginning (30 min), middle (210 min), and end (420 min) of the infiltration event are shown in Fig. 4.3c for different borehole depths. In general, the waveforms simulated at different times show large differences, which was not always the case for the soil water content measurements and the first arrival times. For example, the arrival time of the direct wave simulated at a 0.6 m depth did not show a clear difference between 0 and 30 min (Fig. 4.3b), but the simulated GPR waveforms are obviously different at these measurement times (Fig. 4.3c). To explain this in detail, the wavefield snapshots for the GPR measurements at 0.6 m depth were obtained at the infiltration times of 0 and 30 min (Fig. 4.4). At the early stage of the GPR measurements (8 ns), only the direct waves were generated (Fig. 4.4a and 4.4b). As the infiltration front did not move to 0.6 m depth, the waveforms of the direct wave that were measured by the receiver between 8 and 14 ns (Fig. 4.3c) did not show differences at these two measurement times. The reflected waves were generated on the land surface at around 12 ns (Fig. 4.4b and 4.4c). Since the infiltration event increased the SWC of the top 0.1 m of the soil at 30 min (see Fig. 4.2b), the permittivity of the top soil and the reflection coefficient of the land surface were changed. As a result, the travel time and amplitude of the reflected waves measured by the receiver between 15 and 20 ns (Fig. 4.3c) showed substantial differences (see Fig. 4.4e – 4.4h) at these measurement times.

For a more realistic synthetic modelling study, Gaussian noise with zero mean and a standard deviation of 0.1 ns (Δt) and 0.01 $cm^3\ cm^{-3}$ ($\Delta\theta$) was added to the noise-free GPR travel time and SWC data, respectively. The noise level of 0.1 ns for GPR travel times is based on the sampling interval of 0.2 ns used for measuring GPR data, which limits the accuracy of travel time determination. The noise level of 0.01 $cm^3\ cm^{-3}$ for SWC data is based on the averaged uncertainty of TDR measurements (Topp and Ferré, 2005). The noise added to the GPR waveform data was

based on noise evaluation using previously measured GPR waveforms at recorded times before the first arrival, which showed that noise varied from 0.1 to 0.5 % of the maximum amplitude. Therefore, Gaussian noise with zero mean and a standard deviation of 0.5 % of the maximum amplitude (ΔE) was added to the simulated GPR waveforms in this synthetic study. After obtaining the final inversion results using different inversion approaches, the uncertainty of the estimated parameters was evaluated using the first-order approximation described in Section 3.2.6.

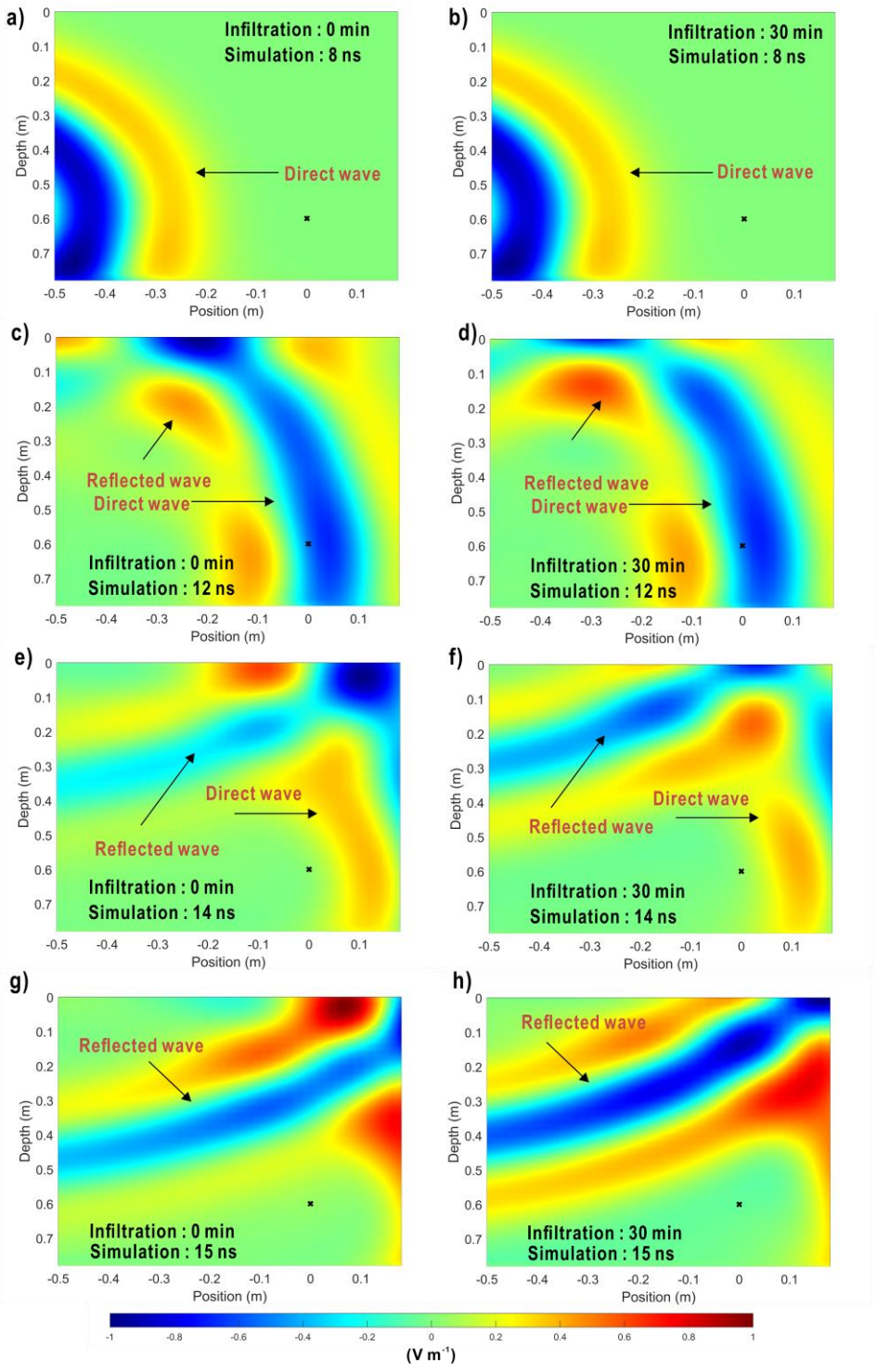

Fig. 4.4 Snapshots of the GPR wavefields for transmitter and receiver position at 0.6 m depth. Wavefields are shown for (a, b) 8 ns, (c, d) 12 ns, (e, f) 14 ns and (g, h) 15 ns for two different measurement times of the infiltration experiment. Each wavefield was normalized with the maximum field value. The position of the receiver antenna is indicated by the black cross. Note that the transmitter is located at a position of -0.75 m at a depth of 0.6 m.

4.3 Results

4.3.1 Response surfaces

In a first step, parameter correlations were analyzed using response surface analysis. Given the available computing power, it was not possible to calculate the response surface for all parameter pairs for a 2-layer profile in the case of GPR travel time and waveform data. In Chapter 3, response surfaces for SWC and GPR travel times were already used to investigate parameter correlations between soil hydraulic parameters for a 1-layer profile (Fig. 3.5). It was found that the response surfaces from GPR travel times and SWC showed similar parameter correlations. Since the layer thickness (h_t) was also considered as a model parameter in this chapter, response surfaces considering this parameter were specifically analyzed to reveal the correlations between layer thickness and different hydraulic parameters for a 2-layer soil profile from GPR waveforms, GPR travel times, and SWCs at three depths (Fig. 4.5).

In general, response surfaces obtained from different types of data again showed similar parameter correlations. In the response surfaces for $h_t - n_1$ and $h_t - n_2$, a steep gradient of the cost function can be observed near the global minimum, which indicates that h_t, n_1, and n_2 are well constrained by the inversion. However, in the response surfaces for $h_t - \log(K_{s1})$, $h_t - \log(K_{s2})$, $h_t - \alpha_1$, and $h_t - \alpha_2$ the misfit distribution is perpendicular to the h_t axis, suggesting that the $\log(K_{s1})$, $\log(K_{s2})$, α_1, and α_2 are less constrained in the inversion. The global minima in the response surfaces for $h_t - \theta_{s1}$ and $h_t - \theta_{s2}$ are positioned in an elongated valley, which implies that θ_{s1} and θ_{s2} are negatively correlated with h_t.

The misfit distributions in the response surfaces from SWC show a strong change at h_t = 0.2 m and h_t = 0.4 m (Fig. 4.5), which were the depths where SWC data were simulated. To explain this, synthetic SWC data (Fig. 4.6a) were simulated by using h_t = 0.18 m and h_t = 0.22 m, while keeping the other parameters at the optimal values (see blue crosses in Fig. 4.5a). Large SWC differences were observed at 0.2 m depth after the soil got fully saturated, because the saturated SWC at this depth was different for the models with h_t = 0.18 m and h_t = 0.22 m (θ_{s1}= 0.229 and θ_{s2} = 0.326 $cm^3\,cm^{-3}$). Similarly, models with the layer boundary below 0.4 m depth will also have different saturated SWCs. The response surfaces for GPR travel times and waveforms do not show a sudden change at h_t = 0.2 m and h_t = 0.4 m. Although, the simulations with h_t = 0.18 m and h = 0.22 m show differences in GPR travel time (Fig. 4.6b) and GPR waveforms (Fig. 4.6c), the cost function values for GPR travel times (0.36 and 0.23 ns) and GPR waveforms (0.98

and 0.84 V m^{-1}) showed much less pronounced differences as SWCs (0.05 and 0.014 cm^3cm^{-3}). This can be explained by the fact that GPR measurements have a larger sampling volume than point measurements. Because of the spatial averaging, GPR travel times and waveforms will be less sensitive to abrupt changes in the vertical SWC profile.

Besides potential parameter correlations, it is also interesting to analyze the cost function values in the response surfaces from different types of data, which were visualized in logarithmic scale after normalization with the expected noise level ($\Delta t, \Delta\theta, \Delta E$). Using this normalization, the areas enclosed by green in the response surfaces can qualitatively be interpreted as the parameter uncertainty. The response surfaces show that many model parameters can be inverted with low uncertainty for the GPR waveform data (at least in theory). To further illustrate this, two sets of model parameters (black crosses in Fig. 4.5a) were selected in the response surfaces for $h_t - \theta_{s1}$, while the other parameters were set to the optimal parameters. SWC, travel times, and waveforms were simulated for both sets of model parameters (Fig. 4.7). It can be seen that both SWC and travel times (Fig. 4.7a and 4.7b) only showed very minor differences for these two sets of simulations. For the simulated GPR waveforms (Fig. 4.7c), the two sets of model parameters also provide almost identical GPR waveforms at the beginning of the experiment (30 min) because the infiltration front was still located at a shallow depth in the first layer (see Fig. 4.2b). When the infiltration front approached the layer boundary (210 min), obvious differences appeared between the waveforms from the true model and the two selected parameter sets, especially at the 0.2 m depth. To explain this in detail, the wavefield snapshots were simulated with the true model and the selected parameter sets (Fig. 4.8). Due the considerable SWC (permittivity) differences between the first and second layer, a strong reflected wave was generated on the layer boundary. It can be seen that the reflected wave was superimposed with the direct wave, but that this did not affect the first arrival time (Fig. 4.8a, 4.8b and 4.8c). Hence, the GPR travel times for the selected parameter sets only showed minor differences. However, the path length and reflection coefficient of the reflected wave are related to h_t, and thus the travel time and amplitude of this reflected wave were different and resulted in the substantial differences for the simulated GPR waveforms (Fig. 4.8d and 4.8e). This also explains the difference in GPR waveforms for these models at the end of the infiltration (420 min). These results highlight that the inversion of SWC obtained with a point measurement such as TDR or GPR travel times only contains information about the SWC at or near the borehole depth. On the other hand, CFWI contains additional information on the hydraulic parameters, and especially the layer depth due to the reflected wave generated from the layer boundary. Therefore, CFWI is expected to outperform the inversion of SWCs and travel times for estimating h_t.

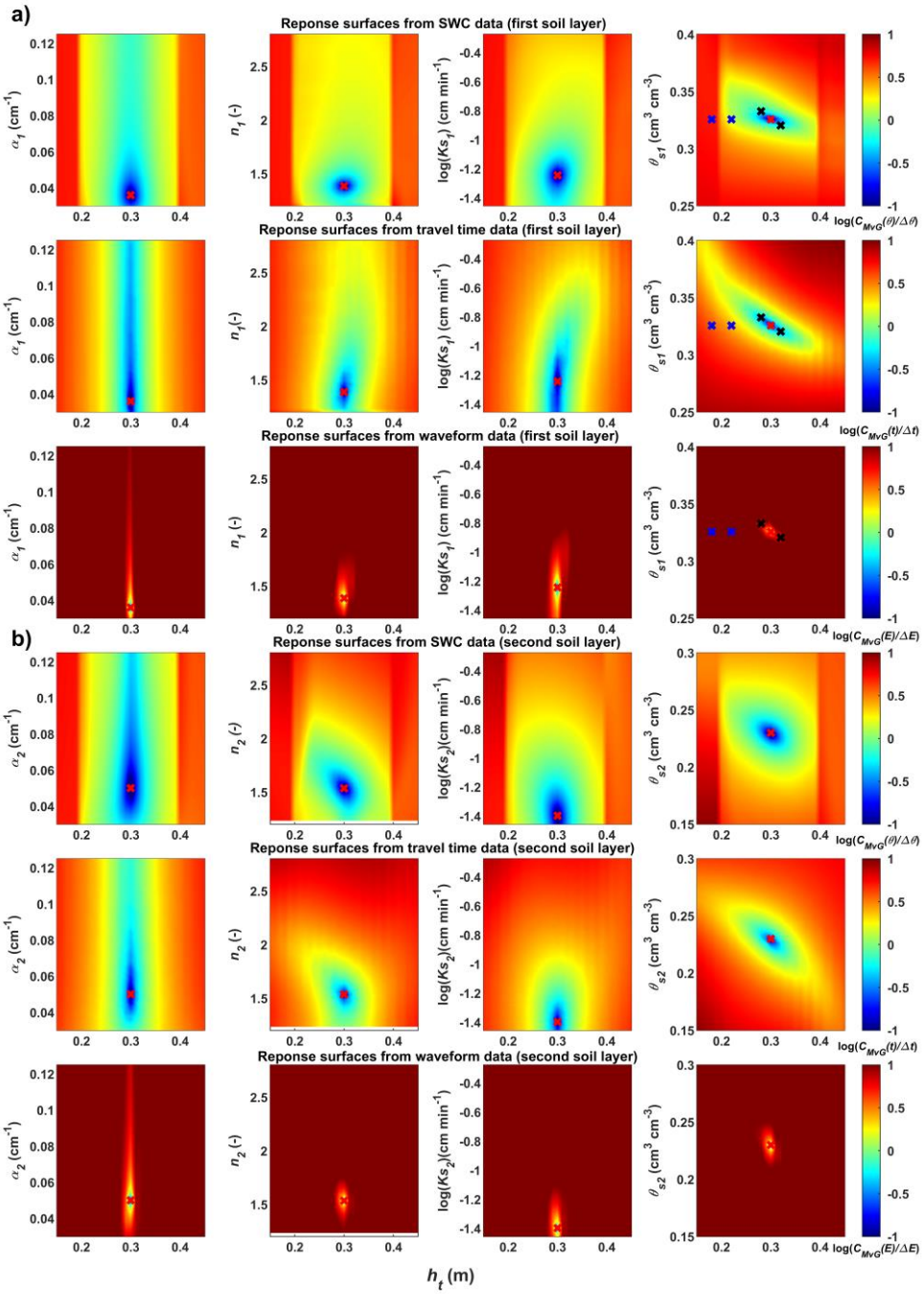

Fig. 4.5 Response surfaces for layer thickness (h_t) and different hydraulic parameters of (a) the first layer and (b) second layer from GPR waveforms, GPR travel times, and SWC. The cost function values were normalized by their noise level and shown in logarithmic scale. Blank spaces indicate that the hydrological model did not converged. The true model is shown by the red cross. In the response surfaces for $h_t - \theta_{s1}$, the black crosses refer to the models of (0.28 m, 0.332 cm^3cm^{-3}) and (0.32 m, 0.320 cm^3cm^{-3}) and the blue crosses refer to the models of (0.18 m, 0.326 cm^3cm^{-3}) and (0.22 m, 0.326 cm^3cm^{-3}).

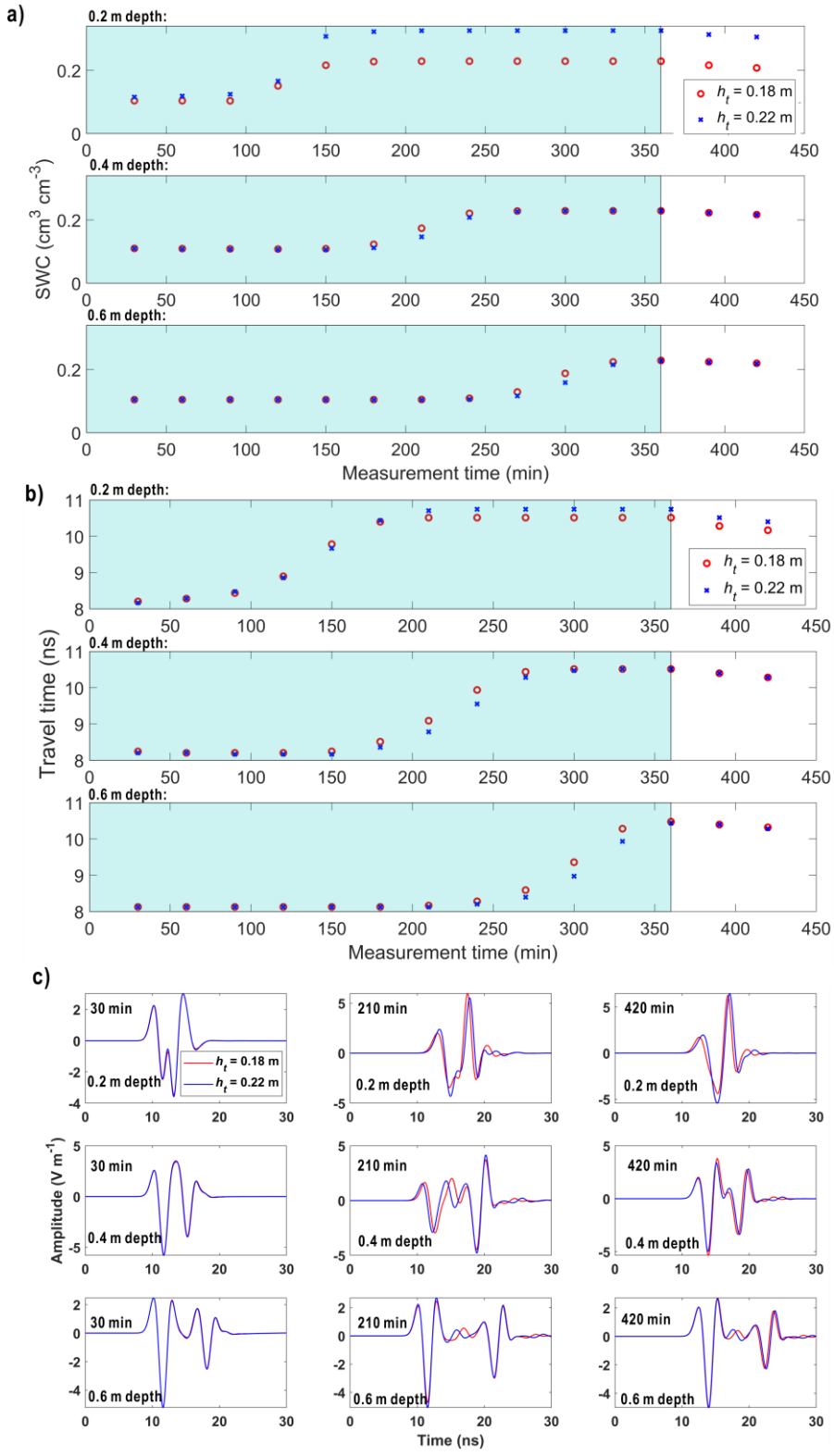

Fig. 4.6 (a) SWC data, (b) synthetic travel times, and (c) synthetic GPR waveforms at three different times calculated according to the models indicated by the blue crosses in Fig. 4.5. The length of the infiltration event is indicated by the light green background.

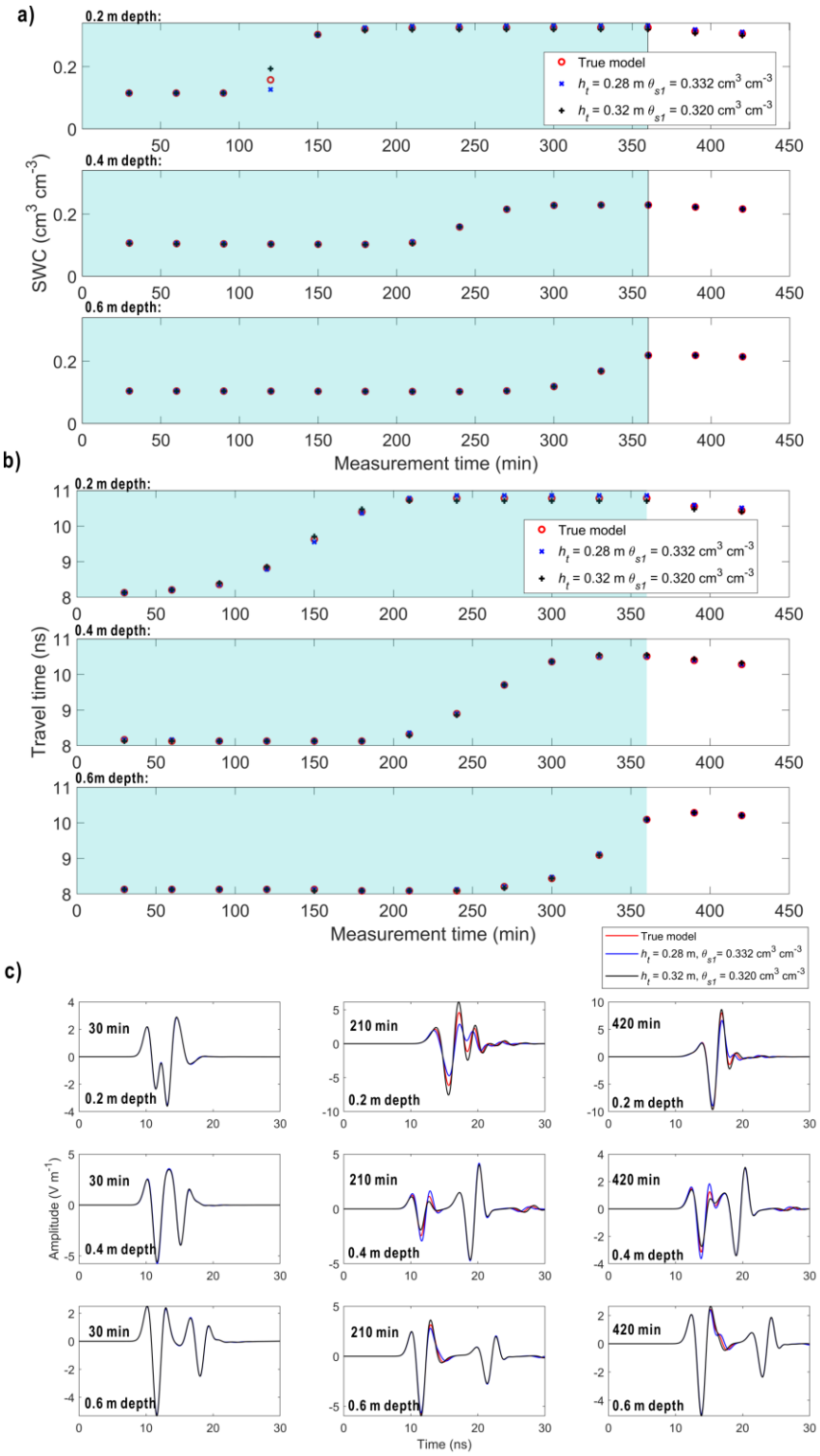

Fig. 4.7 (a) SWC data, (b) synthetic travel times and (c) synthetic GPR waveforms at three different times calculated according to the models indicated by black crosses in Fig. 4.5 and the true model. The length of the infiltration event is indicated by the light green background.

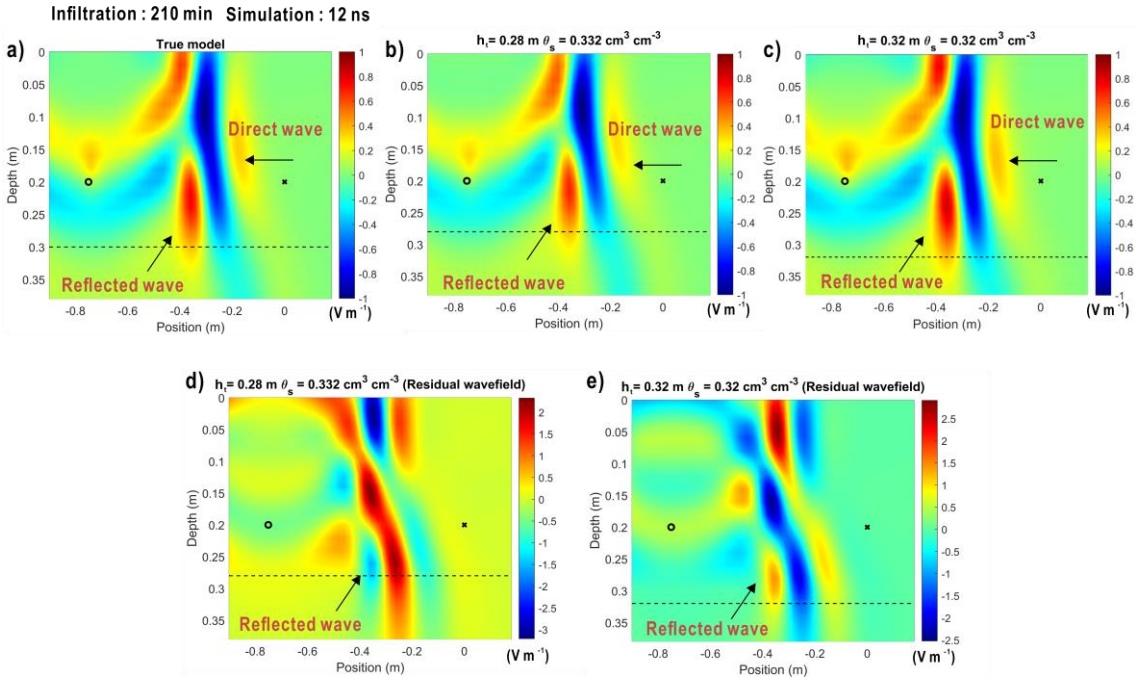

Fig. 4.8 Snapshots of the GPR normalized wavefields simulated at 12 ns for the GPR measurement conducted at 210 min, based on (a) true model, (b) and (c) two selected models indicated by black crosses in Fig. 4.5. (d) and (e) indicate the residual wavefields. The layer boundary is shown by the black dashed line. The positions of the transmitter and receiver antenna are indicated by the black circle and black cross, respectively.

4.3.2 Coupled full waveform inversion

In a second step, hydraulic parameters were estimated by using coupled inversion of noisy travel times and waveforms (Table 4.1). To avoid overfitting, inversions were stopped when the noise levels for travel time (0.1 ns) and waveform data (0.03 V m^{-1}) were reached. In general, the noisy travel times (Fig. 4.9a) and waveforms (Fig. 4.9b) were fitted well by the estimated parameters from coupled inversion of travel time and CFWI, respectively. It also can be seen that the waveforms simulated with the results of the coupled inversion of travel times resulted in a slight mismatch for several measurements, e.g., the measurement conducted at 0.2 m depth at 210 min. This can be attributed to the fact that the coupled inversion of travel times did not use all the information contained in the waveforms. In the case of the coupled inversion of travel times, the inversely estimated parameters showed larger uncertainty, whereas for CFWI the parameter uncertainty was lower and θ_{s1}, α_1, θ_{s2}, α_2, and h_t were accurately estimated. The CFWI estimated values of n_1, $\log(K_{s1})$, n_2, and $\log(K_{s2})$ still showed a slight difference with the true value, which is likely caused by the correlations between $n_1 - \log(K_{s1})$ and $n_2 - \log(K_{s2})$ (Table 4.2). Other parameter combinations did not show strong correlations.

Table 4.1 Inverted results of noisy travel time and waveform data

	True value	Bounds	Inverted results	
			Travel times	Waveforms
	————	2-layer soil profile	————	
θ_{s1} (cm^3cm^{-3})	0.326	0.30 – 0.40	0.330±0.007	$0.326\pm2.58\times10^{-5}$†
α_1 (cm^{-1})	0.036	0.030 – 0.125	0.042± 0.017	0.037±0.0002
n_1 (-)	1.386	1.1 – 2.8	1.240±0.125	1.369±0.002
$\log(K_{s1})$ (cm min^{-1})	-1.244	-1.456 – -0.276	-0.976± 0.180	-1.214±0.004
θ_{s2} (cm^3cm^{-3})	0.229	0.15 – 0.30	0.232± 0.007	$0.229\pm4.03\times10^{-5}$
α_2 (cm^{-1})	0.050	0.030 – 0.125	0.063±0.014	0.049±0.0002
n_2 (-)	1.534	1.1 – 2.8	1.379±0.076	1.527±0.0012
$\log(K_{s2})$ (cm min^{-1})	-1.398	-1.456 – -0.276	-1.123±0.194	-1.396±0.0026
h_t (m)	0.3	0.2 – 0.4	0.29± 0.020	$0.30\pm2.34\times10^{-5}$
Cost-function	-	-	0.01 (ns)	0.03 (V m^{-1})

†The values indicated the 99% confidence interval based on the first-order approximation.

Table 4.2 Correlation matrix of the inverted hydraulic parameters from CFWI

	α_1 (cm^{-1})	n_1 (-)	$\log(K_{s1})$ (cm min^{-1})	α_2 (cm^{-1})	n_2 (-)	$\log(K_{s2})$ (cm min^{-1})	θ_{s1} (cm^3cm^{-3})	θ_{s2} (cm^3cm^{-3})	h_t (m)
n_1	-0.499	1							
$\log(K_{s1})$	0.488	-0.936†	1						
α_2	-0.228	0.441	-0.424	1					
n_2	0.128	0.474	-0.415	-0.054	1				
$\log(K_{s2})$	-0.248	-0.100	0.042	0.519	-0.783†	1			
θ_{s1}	0.272	-0.417	0.604	-0.054	-0.212	0.049	1		
θ_{s2}	-0.162	-0.010	-0.066	0.259	-0.354	0.474	-0.257	1	
h_t	0.127	-0.105	0.154	-0.043	-0.086	0.067	-0.188	-0.122	1

†The values indicated the pairs of parameters showing strong correlation.

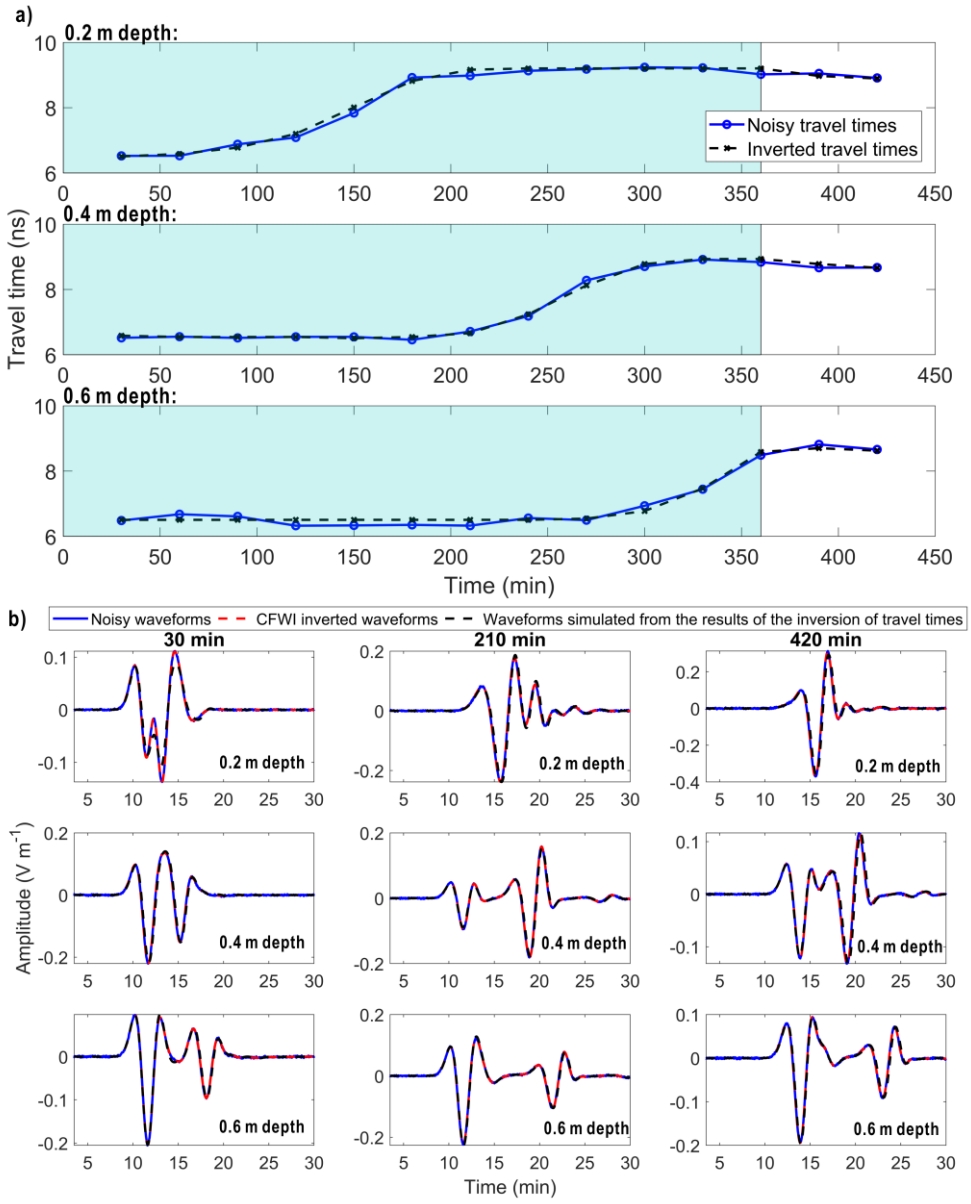

Fig. 4.9 Coupled inversion results from (a) noisy travel times and (b) noisy GPR waveforms. The length of the infiltration event is indicated by the light blue background.

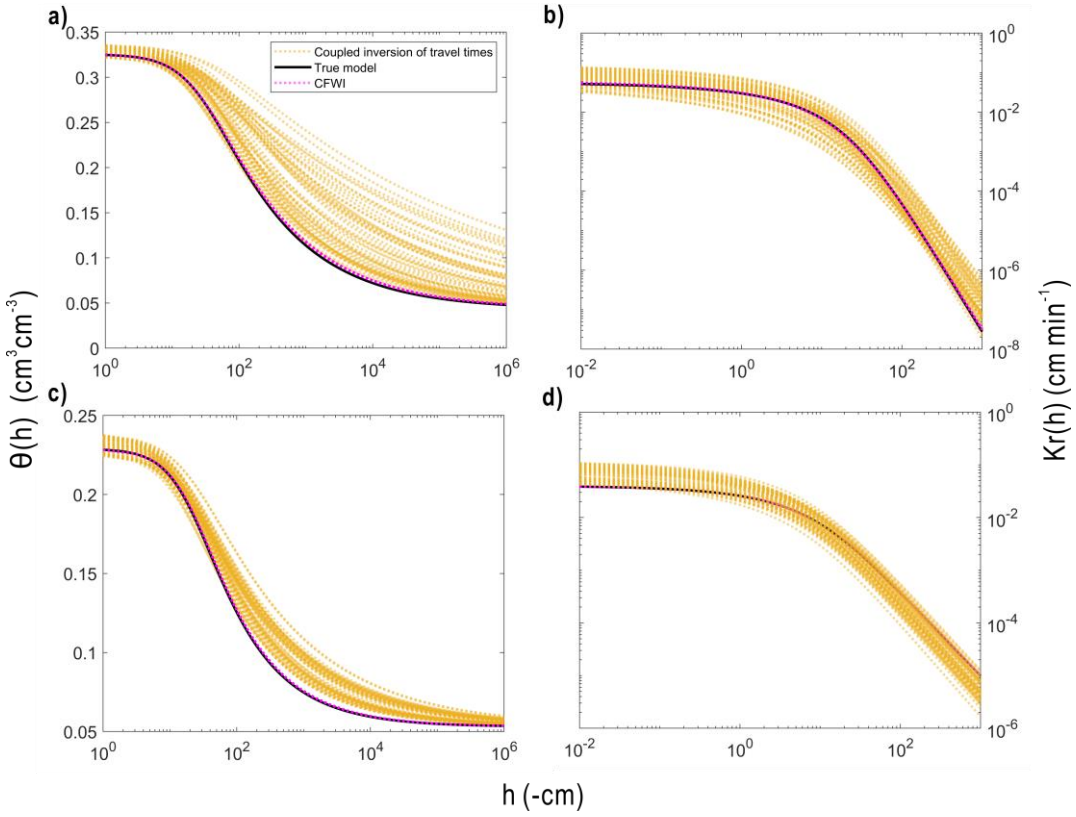

Fig. 4.10 Water retention $\theta(h)$ and relative hydraulic conductivity $K_r(h)$ functions for the first (a, b) and (c, d) second soil layer obtained from the true model (black line) and 50 possible inverted hydraulic parameters sets from coupled inversion of travel times (yellow dashed lines) and CFWI (purple dashed lines), respectively.

Fig. 4.10 presents 50 realizations of the water retention and relative hydraulic conductivity functions based on the estimated parameters from CFWI and coupled inversion of travel times and the associated uncertainty in Table 4.2. Since the CFWI accurately obtained the hydraulic parameters with considerably smaller uncertainty, a very good match was found between the estimated and true water retention and relative hydraulic conductivity functions. However, for the coupled inversion of travel times, the estimated water retention functions (Fig. 4.10a and 4.10c) showed relatively larger uncertainty and did not accurately predict the true function at low pressure heads, because the n_1 and n_2 of the true model were not within the uncertainty bounds of the estimated n_1 and n_2. In addition, since the uncertainty interval of estimated K_{s2} did contain the true K_{s2} value, a slight mismatch (Fig. 4.10d) of the estimated and true relative hydraulic conductivity functions can be found when the second layer is close to the saturation.

4.4 Discussion

Although CFWI showed advantages over the coupled inversion of GPR travel time in the presented synthetic study, it is currently still challenging to use CFWI for processing experimental GPR data. Similar to the FWI approach proposed by Klotzsche et al. (2016), the use of CFWI requires an accurate estimation of the source wavelet from the measured GPR data as the GPR waveform does not only depend on the medium properties (dielectric permittivity and electrical conductivity) but also on the source wavelet emitted by the system and the coupling of the antenna and the medium (Busch et al., 2012, Klotzsche et al., 2018). Ineffective source wavelet estimation from measured GPR data will likely result in erroneous simulation of GPR waveform data, and in consequence will lead to erroneous estimates of the hydraulic parameters using CFWI. Normally, the effective source wavelet is estimated using a deconvolution approach, which relies on the measured data and forward modelling based on starting model values. If there are insufficient measurements with varying offsets or angles, it is very difficult to define such starting models and hence to obtain effective source wavelets. Therefore, the effective source wavelet is very difficult to estimate from GPR data obtained by ZOP data acquisition. For the GPR data in this thesis, the phase of the effective source wavelet can be estimated using a starting model where the permittivity is obtained from a ray-based inversion with sufficient accuracy. However, the amplitude of the wavelet is directly coupled to the medium properties and is very sensitive to small changes in the electrical conductivity. For this reason, it is not yet possible to apply CFWI to the GPR data presented in this thesis. To estimate an effective waveform for CFWI, a feasible approach would be to perform MOG measurements before measuring the ZOP data or to apply the workflow proposed by Busch et al. (2012) to estimate the source wavelet from the ZOP/ MOG data.

A second challenge for CFWI is the need for accurate estimation of the electrical conductivity distribution. In this chapter, the electrical conductivity profiles for GPR modelling were obtained from the corresponding SWC profiles by using Archie's law. However, the uncertainty in Archie's law for estimating soil conductivity from SWC is much greater than that in the petrophysical models relating permittivity and SWC (e.g., CRIM), because soil electrical conductivity is also sensitive to other factors, e.g., clay content and pore water salinity (Binley et al., 2015). Furthermore, Archie's law does not consider surface electrical conductivity associated with the electrical double layer surrounding soil particles. Advanced petrophysical models should be employed in future studies to consider the influence of the surface conductivity (e.g., Revil et al., 2007; Mboh et al., 2012). In addition, the electrical conductivity distribution may not only be

related to the SWC distribution, because of independent variations in the pore water electrical conductivity associated with fertilizer application or geochemical reactions in the subsurface. This mismatch between the distribution of electrical conductivity and SWC cannot be neglected in a real-life infiltration experiment. To accurately describe the electrical conductivity distribution, it may thus be necessary to consider a solute transport and/or geochemical model coupled with the Richards equation (Eq. 1.1) to predict the distribution of the bulk electrical conductivity in the unsaturated soil (e.g., Loague and Green, 1991). Unfortunately, by doing so more unknowns will be introduced and will undoubtedly increase the difficulty of CFWI. Finally, soils of high salinity or clay content may lead to a strong attenuation of the waveform amplitude. As a result, the noise level of the actual field data measured in these types of soil could be relatively high. Compared to the coupled inversion of the travel times, CFWI may thus be less robust to estimate the hydraulic parameters for these types of soils.

Another point of discussion is that the use of CFWI relies heavily on accurate simulations of GPR data, as the amplitudes of the entire waveform are considered in the cost function. For the gprMax3D modelling using the Finite-difference time-domain method (FDTD), the systematic modelling errors generated from the finite-difference discretization and numerical dispersion (Warnick, 2005) will likely also introduce errors in the hydraulic parameter estimation. In this study, the grid size was set to 0.02 m, which may not be sufficient for accurate GPR simulations in actual 2D or 3D applications of CFWI.

Finally, it is important to emphasize here that CFWI is time-consuming. For the synthetic study presented here, CFWI took almost 10 days with a computer cluster (48 processers of AMD Opteron 6300) or a week with the JURECA supercomputer (24 processors) although the FDTD algorithm in gprMax3D was able to calculate in parallel. If modelling errors need to be further reduced, the discretization of the simulation needs to be refined, which will further increase computational costs. Therefore, it is important to improve the efficiency and accuracy of the current GPR modelling method. An additional improvement in the computational efficiency of CFWI can be achieved by the simultaneous parallelization of the SCE-UA and FDTD algorithm, which should also be explored in future studies.

4.5 Conclusions

In this chapter, I conducted a synthetic study to explore the feasibility of using CFWI to estimate the hydraulic parameters and the layer thickness for a 2-layer soil profile. First, a workflow for CFWI was introduced. Compared with the coupled inversion of travel times, CFWI directly uses

the entire GPR waveform and can therefore avoid propagation of uncertainties from the picking of first arrivals into the inversion. In a next step, I used the 2-layer soil profile introduced in Chapter 3 and proposed an efficient infiltration experiment to obtain synthetic vertical SWC profiles. This experiment included a 6-hour infiltration event with GPR measurements at three depths only (0.2, 0.4, and 0.6 m depth). Based on this experimental design, response surfaces for the layer thickness and different hydraulic parameters were calculated for point SWC measurements, GPR travel times and GPR waveforms to investigate potential parameter correlations. It was found that h_t was negatively correlated with θ_{s1} and θ_{s2}. In addition, the response surfaces indicated that CFWI provided more accurate estimates of layer depth compared with coupled inversion of GPR travel times and inversion of point SWC measurements. This is attributed to the fact that CFWI contains additional information introduced by the reflected wave from the layer boundary. Finally, CFWI and coupled inversion of GPR travel times were applied to the synthetic infiltration experiment. The simulated waveforms and travel times matched well with the noisy data but the estimates of the hydraulic parameters from the coupled inversion of travel times showed a slight deviation from the true values and a relatively larger uncertainty in the hydraulic conductivity and retention functions. On the other hand, hydraulic parameters estimated from CFWI had considerably smaller uncertainty and thus better matched the known water retention and hydraulic conductivity curves. However, a range of challenges remain for the application of CFWI to real field experiments. First, a robust approach for source wavelet estimation for measured ZOP data has to be developed. Moreover, the use of a more sophisticated hydrological model that couples the simulations of water flow and solute transport has to be considered for CFWI to cope with changes in electrical conductivity associated with fertilization and geochemical processes. In addition, the accuracy and efficiency of the current GPR modelling has to be improved. In conclusion, CFWI has several advantages over the coupled inversion of GPR travel times and it is expected to be a promising inversion approach for estimating hydraulic parameters at field scale, after solving several remaining problems.

CHAPTER 5 SYNTHESIS AND OUTLOOK

5.1 Synthesis

The work performed in this thesis aimed to investigate the potential of time-lapse GPR measurements for the estimation of soil hydraulic parameters from infiltration events. First, the combined use of surface and horizontal borehole GPR to monitor SWC variations during an infiltration experiment conducted at a rhizotron facility at the Selhausen test site was investigated. Second, the performance of sequential and coupled inversion strategies for estimating soil hydraulic parameters based on horizontal borehole GPR measurements was tested. Finally, the feasibility of the use of CFWI for estimating soil hydraulic parameters and layer thickness for a 2-layer profile was explored and current limitations of CFWI for the application to measured borehole GPR data were discussed.

In the first part (Chapter 2), SWC dynamics during an infiltration experiment were monitored by the combined use of horizontal borehole and surface GPR measurements. The 200 MHz ZOP borehole GPR data were processed using a ray-based approach to reveal the spatial SWC variations along the horizontal boreholes installed at 0.2, 0.4, 0.6, 0.8, and 1.2 m depth during the infiltration experiment. However, the ray-based approach did not provide accurate SWC estimates for the top soil (0 – 0.1 m depth) from the horizontal borehole GPR data measured at 0.1 m depth, because of interference between the direct and refracted wave at this shallow depth. To obtain detailed SWC information for the top soil, multi-offset surface GPR measurements were made with different antenna frequencies (100, 200, and 500 MHz). Standard semblance analysis was employed to process these data. The SWC estimates obtained from 100 and 200 MHz data corresponded to large sampling depths of 0.7 and 0.5 m, respectively, and were therefore not suitable to represent the SWC of the shallow top 0.1 m soil layer. On the other hand, the 500 MHz GPR data showed strong dispersion because the wavelength at this frequency is comparable with the thickness of the infiltration-induced waveguide. As a result, semblance analysis did not provide accurate SWC estimates for the 500 MHz data. To solve this problem, a dispersion analysis was employed to correctly estimate the SWC of the wet layer close to the surface and the thickness of the waveguide. The estimated thickness was found to be around 0.1 m during the entire experiment, which is attributed to the presence of a plough layer associated with agricultural management that acted as the waveguide. Hence, the SWC estimates obtained from the waveguide was used to represent the average SWC of the top 0.1 m of the soil. Finally, the vertical SWC

profiles (0 – 1.2 m) was obtained by combining the SWC estimates from the horizontal borehole and surface GPR, which was used to reconstruct the SWC dynamics during and between infiltration events. To increase confidence in the obtained results, the SWC estimates from GPR were compared to the independent SWC estimates from TDR. Reasonable consistency was found between the GPR and TDR estimates, as they displayed a similar temporal response to the infiltration events. Furthermore, a regression between SWC estimates obtained with GPR and TDR resulted in a slope close to 1 (0.96) and a small intercept of 0.02 cm^3cm^{-3}. Finally, the changes in soil water storage over the entire soil profile were calculated for both GPR and TDR. It was found that the combined GPR estimates matched well with the known water amount used during irrigation, whereas the water storage obtained with TDR systematically overestimated the known water storage due to the poor spatial representativeness of the local TDR measurements that were made on one side of the irrigated area only.

In the second part (Chapter 3), the feasibility of estimating soil hydraulic properties for the rhizotron facility at the Selhausen test site was evaluated by employing either a sequential inversion or a coupled inversion approach to the horizontal borehole GPR data. First, a synthetic infiltration experiment for a 1-layer profile was designed based on soil hydraulic parameters reported by Cai et al. (2018a) and the schedule of the infiltration experiment used in Chapter 2. Synthetic vertical SWC profiles were obtained using HYDRUS-1D at actual GPR measurement times and used to simulate GPR wave propagation for measurements at 6 depths (0.1, 0.2, 0.4, 0.6, 0.8, and 1.2 m) with gprMax3D. GPR travel times were automatically picked from the synthetic GPR measurements and used to estimate SWC at the six depths based on a ray-based approach. Response surfaces were obtained by conducting grid searches based on the cost functions for GPR travel times and true SWC data to demonstrate the correlations between the soil hydraulic parameters. It was found that the saturated water content θ_s, can be well constrained by the inversion, whereas the α parameter is expected to be less constrained. The hydraulic parameters n and $\log(K_s)$ were negatively correlated, and thus cannot be well disentangled from each other. In a next step, the GPR SWC estimates and GPR travel time data with added noise were inverted by a sequential and a coupled inversion approach, respectively. In the sequential inversion approach, the soil hydraulic parameters were estimated from the SWC estimates obtained from the GPR data using the straight-wave approximation. This did not return accurate estimates of the soil hydraulic parameters because the SWC obtained with this approach underestimated the actual SWC at shallow depths and near the infiltration front. On the other hand, the coupled inversion directly assimilated GPR travel times, and thus avoided interpretation errors which occurred in the SWC estimates using the ray-based approach. Therefore, the coupled

inversion provided accurate estimates of the hydraulic properties both for a 1-layer and a 2-layer soil profile. In the final step, soil hydraulic parameters were estimated from actual GPR data using the coupled inversion approach. The results showed a reasonable consistency with the water retention and relative hydraulic conductivity functions reported in the independent study of Cai et al. (2018a).

In the third and final part (Chapter 4), the feasibility of coupled inversion of horizontal borehole GPR full waveform data for estimating soil hydraulic parameters and layer thickness for a 2-layer profile was investigated. First, a workflow for such a coupled full waveform inversion (CFWI) was proposed. In contrast to the coupled inversion of GPR travel times, CFWI directly optimized the misfits between measured and simulated waveforms in the time domain instead of the first-arrival times. In the established CFWI workflow, the soil electrical conductivity profile was estimated from SWC and Archie's law. This was not required for the coupled inversion of GPR travel times because the electrical conductivity only influences the amplitude of GPR waveforms. Based on the infiltration experiment introduced in Chapter 2 and 3, a new synthetic infiltration experiment was designed to reduce the computational costs needed for the inversion. In the new infiltration experiment, only one single 360-min infiltration event was assumed for a 2-layer soil profile and horizontal GPR data were obtained at 0.2, 0.4, and 0.6 m depth only. To evaluate the correlation between the soil hydraulic parameters and the layer thickness during parameter estimation, response surfaces were again calculated based on the true SWC data, GPR travel times, and GPR waveforms. For the different inversion approaches, the layer thickness, h_t, was found to be negatively correlated with the saturated water content of the topsoil (θ_{s1}) and subsoil (θ_{s2}). Furthermore, the response surfaces demonstrated that CFWI can more accurately estimate the layer thickness h_t compared with the coupled inversion of travel times and inversion of SWC data, because CFWI contains additional information through the reflected wave generated from the layer boundary. In a next step, CFWI and coupled inversion of GPR travel times were performed for the synthetic infiltration experiment. CFWI estimated soil hydraulic parameters and layer thickness with considerably smaller uncertainty and matched well with the known water retention and hydraulic conductivity functions, whereas the hydraulic parameters obtained by the coupled inversion of travel times exhibited a slight deviation from the true parameters and relatively larger uncertainty in the hydraulic conductivity and retention functions. Despite the promising results demonstrated by the synthetic study, the application of CFWI to measured horizontal borehole GPR data is still challenging. A first challenge is the required knowledge of the effective source wavelet used for CFWI, as it cannot be estimated from the GPR data obtained with a ZOP data acquisition strategy. A second challenge for CFWI is the need for accurate

estimation for the electrical conductivity distribution during the infiltration experiment, because the uncertainty in the petrophysical relationship between electrical conductivity (e.g., Archie's law) is much greater than that in the petrophysical models relating permittivity and SWC (e.g., CRIM). Furthermore, the distribution of electrical conductivity may not only be related to the SWC distribution, but might be also influenced by independent variations in the pore water electrical conductivity associated with fertilizer application or geochemical reactions in the subsurface. Finally, CFWI is time-consuming and even more computational costs would be demanded if CFWI is used to estimate actual 2D/3D distribution of soil hydraulic parameters, as it requires higher accuracy for the simulation of GPR data.

In general, it was concluded that the combined use of borehole and surface GPR measurements allows to determine spatiotemporal SWC dynamics during infiltration events. Furthermore, hydraulic parameters can reliably be estimated using the coupled inversion of the GPR travel time data measured during infiltration. It was also found that ZOP measurements underestimated the actual SWC at depths where strong SWC gradients are present. As a result, coupled inversion outperforms sequential inversion for estimating the hydraulic parameters from ZOP data if there are strong vertical SWC gradients. Considering the computational costs of coupled inversion, sequential inversion still is useful when vertical variation in SWC is low. Finally, it was shown that CFWI can estimate the hydraulic parameters and layer thickness with less uncertainty compared to coupled inversion of GPR travel times. Therefore, it is expected to be a promising method for characterizing soil hydraulic properties at the field scale after several remaining challenges have been adequately addressed.

5.2 Outlook

The presented work showed how GPR measurements can be used to characterize soil hydraulic properties at the field scale. As the research and rethinking should never cease, the following section provides perspectives on improving the presented work and ideas that may be worthwhile to explore in future studies.

As shown in Chapter 2, the ray-based approach cannot provide accurate SWC estimates for the top 0.1 m of soil from horizontal borehole GPR data measured at 0.1 m depth. Besides the combination with surface GPR data explored in this thesis, another approach to obtain accurate SWC estimates at 0.1 m depth is to use FWI for the horizontal borehole GPR data, as already suggested by Klotzsche et al. (2016). However, the main challenge of performing FWI is how to estimate an efficient source wavelet from a single ZOP trace. Furthermore, the depth of the horizontal boreholes was found to vary in time due to regular agricultural activity and soil compaction at the Selhausen test site. Therefore, FWI may be also need to take the borehole depth into consideration. Theoretically, this can be achieved because the refracted wave at the soil-air interface is sensitive to the borehole depth.

It is common for infiltration events to generate low velocity waveguides resulting in the dispersion of surface GPR data. Infiltration-induced near-surface SWC profiles can be resolved by using dispersion analysis of surface GPR data. In Chapter 2, the dispersion analysis of a single layer waveguide model was employed to obtain the SWC information of the top soil. Due to the stronger measurement noise at low frequencies and the simplification of the vertical SWC distribution to a single-layer model, the SWC of the material underlying the waveguide was inaccurately estimated. To solve this issue, a joint waveguide inversion of the high-frequency (e.g., 500 MHz) and low-frequency (e.g., 250 MHz) dispersive surface GPR data can be performed, since the permittivity of the underlying material is more sensitive to the low frequencies of the dispersion curve (Bikowski et al., 2012). Furthermore, a piece-wise linear model can be employed (Mangel et al., 2017). This will not only reduce the inversion uncertainty of the permittivity of the underlying material (Strobbia and Cassiani, 2007), but will also provide a more continuous and smoother SWC profile that better describes the actual vertical SWC distribution during infiltration events. However, dispersion analysis with a multi-layer model is more challenging due to the non-uniqueness of the inversion as indicated by van der Kruk et al. (2010).

In Chapter 3, the application of sequential and coupled inversion approaches to estimate soil hydraulic parameters was discussed. Besides the borehole GPR data used in this study, sequential and coupled inversion approaches can obviously also be applied to other types of GPR measurements. However, until now, no studies utilized either a sequential inversion or a coupled inversion approach to estimate soil hydraulic properties using dispersive surface GPR data. Since the SWC profiles can be reliably estimated from dispersive surface GPR data, it will be interesting to characterize the soil hydraulic properties by using a sequential inversion of vertical SWC profiles obtained by dispersion analysis based on a piece-wise linear model. As a coupled inversion approach can avoid interpretation errors and since the forward modelling of theoretical dispersion curves for a guided wave based on the modal theory does not require high computational costs, the coupled inversion approach of the phase velocities of GPR guided wave is expected to be even more powerful to estimate soil hydraulic parameters from dispersive GPR data.

It would be also interesting to apply CFWI to dispersive surface GPR data for estimating soil hydraulic parameters. In fact, it would be easier to conduct CFWI with surface GPR measurements than for borehole GPR measurements because the effective source wavelet can be determined from multi-offset GPR measurements using the approach of Busch et al. (2012). However, dispersive GPR data can only be employed to characterize soil hydraulic properties of a one-layer soil profile or a multi-layer soil profile that does not show strong vertical changes in saturated water content and porosity. For example, a two-layer soil profile where the saturated water content of the subsoil is considerably larger than that of the topsoil will lead to a leaky waveguide when the subsoil gets saturated during infiltration. In such a case, SWC dynamics in the second layer cannot be obtained from the dispersive GPR data (van der Kruk et al., 2009b). In addition, for a two-layer soil profile where the saturated water content of the subsoil is considerably smaller than that of the topsoil, there will be a sharp decrease of SWC at the layer boundary when the infiltration front has moved into the subsoil. As a result, a large part of the radar energy would be trapped within the topsoil and thus it will be also difficult to obtain information on the SWC dynamics in the subsoil based on dispersive surface GPR measurements.

In this thesis, I highlighted the feasibility of using coupled inversion to estimate soil hydraulic parameters based on horizontal borehole GPR measurements obtained during infiltration events at the field scale. In future studies, it will be interesting to use coupled inversion to estimate soil hydraulic parameters from long-term horizontal borehole GPR measurements under natural rainfall (atmospheric conditions). By doing so, it may also be possible to estimate the residual

water content, since such longer time series of GPR measurements will also contain measurements in dry soil conditions in summer. On the other hand, the soil may not get fully saturated during natural rainfall events, and thus the inversion may not be sensitive to the saturated water content.

Following the pioneering work of Kowalsky et al. (2004), coupled inversion may be also used to estimate the heterogeneous distribution of the saturated hydraulic conductivity using multi-offset horizontal borehole GPR data. In principle, the CFWI might be more suitable than the coupled inversion of GPR travel times since full waveforms contain more information and may thus lead to reduced inversion uncertainty. However, as discussed in Chapter 4, CFWI still is associated with a number of challenges when dealing with measured GPR data. To improve CFWI, a robust approach should be developed to estimate an effective source wavelet from measured data first. The method reported by Busch et al. (2012) based on multi-offset GPR measurements may provide a solution, but this needs to be further tested. To better estimate the electrical conductivity distribution during the infiltration process, a more sophisticated model coupling water flow, solute transport, and a geochemical model can be integrated into the CFWI scheme. However, this will introduce additional unknown parameters and therefore there is no doubt that the difficulty of performing CFWI will increase. Furthermore, although the electrical conductivity is commonly frequency-dependent, the difference of electrical conductivity measured in low and high frequencies is commonly within an order of magnitude for most types of soil (Domenzain et al., 2020). Based on this fact, in Chapter 4, the frequency-dependency of soil electrical conductivity was not considered and the distribution of the electrical conductivity was estimated based on the distribution of SWC only. Moreover, it is reasonable to assume that the conductivity obtained by direct current (DC) resistivity methods is equal to the soil electrical conductivity that affects GPR measurements. Therefore, besides employing a complex hydrological model that couples the water flow and solute transport, the effective electrical conductivity distribution during infiltration required for CFWI can be obtained from DC methods. In addition, as discussed in Chapter 4, the coupled inversion of GPR travel time data is more robust than the CFWI for estimating soil hydraulic parameters for the soil of high electrical conductivity. In Chapter 3, the distribution of the electrical conductivity was not considered for the GPR modelling, because generally the electrical conductivity only has negligible influence on the velocity of radar wave. However, in the situation where the soil electrical conductivity is higher than 0.1 S m^{-1}, the influence of soil electrical conductivity on the velocity of radar wave will be unneglectable (Al Hagrey and Müller, 2000). Therefore, it would be also necessary to estimate an accurate distribution of electrical conductivity with the suggested approaches for the coupled inversion of travel times for cases of

estimating hydraulic parameters for soils of high salinity or clay content.

The work in this thesis showed that it would be beneficial to improve the accuracy and especially the efficiency of current methods for GPR modelling. To more efficiently conduct CFWI, the simultaneous parallelization of the optimization and FDTD algorithm is desirable. Due to the limitation of the computer power, I only analyzed the correlations between layer thickness and different hydraulic parameters for a 2-layer soil profile in Chapter 4. In future studies, it will also necessary to study the correlations between the different hydraulic parameters for a two-layer soil profile by using the response surface. Moreover, a traditional first-order approximation was employed in Chapter 3 and Chapter 4 to quantify the uncertainty of the inverted hydraulic parameters. It is well known that this only works well with linear or nearly linear hydrological models (Vrugt and Dane, 2006). This method obtained promising uncertainty ranges for inverted hydraulic parameters in this thesis, since hydraulic parameters were found to change steadily with changes in the model parameters. Complex banana-shaped relationships between parameters that have previously been reported for soil hydraulic parameter estimation were not observed in the the response surfaces analyzed in this thesis. Nevertheless, this method may have a poor approximation of parameter uncertainty for actual 2D or 3D applications of CFWI. After improving the efficiency of GPR modelling, a more sophisticated approach, such as the differential evolution adaptive metropolis algorithm (DREAM), should be used to better evaluate the uncertainty ranges for inverted hydraulic parameters.

After resolving the remaining issues with CFWI, it can hopefully be employed to estimate 2D or even 3D distributions of soil hydraulic parameters from multi-offset GPR measurements. However, since the FWI of GPR measurements for 2D/3D applications is commonly prone to non-uniqueness (Domenzain et al., 2020), it would also be important to employ other geophysical measurements to constrain the CFWI, e.g., a joint coupled inversion of GPR full waveforms and ERT data.

ACKNOWLEDGEMENTS

Doing a PhD is a process of self-transcendence. This process is really not easy and it is certain that I would have never finished my PhD project without the invaluable help from some great people around me.

First, I would express my special appreciation to my initial supervisor Prof. Dr. Jan van der Kruk. Fortunately, I attended his GPR lectures in Wuhan 6 years ago. I still remember how happy and grateful I was when he offered me an opportunity to join his research group. He is one of the most excellent GPR experts in the world, who is knowledgeable and always coming up with innovative ideas. He was the guide of my academic introduction to hydrogeophysics and gave me many helpful advice and support when I started my PhD project. I am grateful for everything he did for me and hope that he can stay healthy and have a great life in the future. In addition, I would like to thank Dr. Anja Klotzsche, who spent a lot of time on my project. She kindly supported me with experimental GPR data and Matlab code to develop my project. She also shared her experience in field work and programming, from which I benefited a lot.

I need to express my profound gratitude to my two additional supervisors Prof. Dr. J.A. (Sander) Huisman and PD Dr. Lutz Weihermüller, who helped me in my worst hour of need. I dread to think how I could have finished my PhD without their help. Sander is one of the most intelligent geophysicists I have ever met, and he helped me a lot to improve scientific thinking and paper writing. Lutz is one of the best soil scientists and a great tutor in hydrology. He gave me many fruitful suggestions for performing the hydrological modelling. They were the people who always gave me useful solutions when I was stuck with my research. They shared with me not only skills and knowledge but also their rigorous attitude for academic research, which will continue to benefit me in my future career. I am also grateful to Prof. Dr. Harry Vereecken and Prof. Dr. Andreas Kemna, who are my supervisors at Bonn university. They helped me to get the qualification for applying a doctoral degree. In addition, Harry gave me many valuable feedbacks during the discussion of my PhD reports and oral presentations.

It was my pleasure to work with our great group members: Christian, Igor, Jessica, Lena, Manuela, Nasim, Pasha, Peleg, Tao Liu, and Zhen Zhou. I would like to specially thank Jessica, Lena and Nasim. The moments working with them in the Rhizotron facility will be a lifetime memory for me. I also need to thank my warmhearted office mates Cosimo and Magdalena. I really enjoyed the time staying with them in the office. During my time in Jülich, I made many new friends that

I would also like to thank for their support: Gaochao Cai, Cheng Sheng, Shehan, Liming Wang, Dazhi Li, Yi Wang, Yi Zhao, Jie Tian, Ying Xing, Yajie Sun, Jihuan Wang, Yafei Huang, Qian Zhang, Xiaoran Zhou, Satoshi, Haoran Wang, Haojin Zhao, Liyan Zhuang, Xinyue Cao. Of course, I also thank the other colleagues in IBG-3 who kindly helped me in last years. Thanks a million!

Last but not least, I express my thanks to my parents and girlfriend Ziyun Li. Without their support and encouragement, I would not have accomplished my PhD work. Finally, China Scholarship Council (Project No. 201606410058) is acknowledged. In addition, I gratefully acknowledge the computing time granted by the John von Neumann Institute for Computing (NIC) and provided on the supercomputer JURECA (Jülich Supercomputing Centre, 2018) of the Jülich Supercomputing Centre (JSC).

BIBLIOGRAPHY

Abbaspour, K., Kasteel, R., Schulin, R., 2000. Inverse parameter estimation in a layered unsaturated field soil. Soil Sci. 165(2): 109-123.

Al Hagrey, S.A., Müller, C., 2000. GPR study of pore water content and salinity in sand. Geophys. Prospect. 48(1): 63-85. doi:10.1046/j.1365-2478.2000.00180.x.

Algeo, J., Van Dam, R.L., Slater, L., 2016. Early-Time GPR: A method to monitor spatial variations in soil water content during irrigation in clay soils. Vadose Zone J. 15(11): vzj2016.03.0026. doi:10.2136/vzj2016.03.0026.

Allroggen, N., van Schaik, N.L.M.B., Tronicke, J., 2015. 4D ground-penetrating radar during a plot scale dye tracer experiment. J. Appl. Geophy. 118: 139-144. doi:10.1016 /j.jappgeo. 2015.04.016.

Altdorff, D., von Hebel, C., Borchard, N., van der Kruk, J., Bogena, H.R., Vereecken, H., Huisman, J.A., 2017. Potential of catchment-wide soil water content prediction using electromagnetic induction in a forest ecosystem. Environ. Earth Sci. 76(3): 111. doi:10.100 7/s12665-016-6361-3.

Alumbaugh, D., Chang, P.Y., Paprocki, L., Brainard, J.R., Glass, R.J., Rautman, C.A., 2002. Estimating moisture contents in the vadose zone using cross-borehole ground penetrating radar: A study of accuracy and repeatability. Water Resour. Res. 38(12): 45-1-45-12. doi: 10.1029/ 2001WR000754.

Angulo-Jaramillo, R., Gaudet, J.-P., Thony, J.-L., Vauclin, M., 1996. Measurement of hydraulic properties and mobile water content of a field soil. Soil Sci. Soc. Am. J. 60(3): 710-715. doi: 10.2136/sssaj1996.03615995006000030004x.

Angulo-Jaramillo, R., Vandervaere, J.-P., Roulier, S., Thony, J.-L., Gaudet, J.-P., Vauclin, M., 2000. Field measurement of soil surface hydraulic properties by disc and ring infiltrometers: A review and recent developments. Soil Tillage Res. 55(1): 1-29. doi:10.1016/S0167-1987(00) 00098-2.

Archie, G.E., 1942. The electrical resistivity log as an aid in determining some reservoir characteristics. Transactions of the AIME. 146(01): 54-62.

Arcone, S.A., 1984. Field observations of electromagnetic pulse propagation in dielectric slabs. Geophysics. 49(10): 1763-1773. doi:10.1190/1.1441584.

Arcone, S.A., Peapples, P.R., Liu, L., 2003. Propagation of a ground-penetrating radar (GPR) pulse in a thin-surface waveguide. Geophysics. 68(6): 1922-1933. doi:10.1190/1.1635046.

Bagarello, V., Sgroi, A., 2004. Using the single-ring infiltrometer method to detect temporal changes in surface soil field-saturated hydraulic conductivity. Soil Tillage Res. 76(1): 13-24. doi:10.1016/j.still.2003.08.008.

Bear, J., 1972. Dynamics of fluids in porous media. American Elsevier Publishing Company.

Beff, L., Günther, T., Vandoorne, B., Couvreur, V., Javaux, M., 2013. Three-dimensional monitoring of soil water content in a maize field using electrical resistivity tomography. Hydrol. Earth Syst. Sci. 17(2): 595-609. doi:10.5194/hess-17-595-2013.

Berenger, J.P., 1994. A perfectly matched layer for the absorption of electromagnetic waves. J. Comput. Phys. 114(2): 185-200. doi:10.1006/jcph.1994.1159.

Beres Jr., M., Haeni, F.P., 1991. Application of ground-penetrating-radar methods in hydrogeologie studies. Groundwater. 29(3): 375-386. doi:10.1111/j.1745-6584.1991.tb0052 8.x.

Berkhout, A.J., 2012. Combining full wavefield migration and full waveform inversion, a glance into the future of seismic imaging. Geophysics. 77(2): S43-S50. doi:10.1190/geo2011-0148.1.

Bikowski, J., Huisman, J.A., Vrugt, J.A., Vereecken, H., van der Kruk, J., 2012. Integrated analysis of waveguide dispersed GPR pulses using deterministic and Bayesian inversion methods. Near Surf. Geophys. 10(6): 641-652. doi:10.3997/1873-0604.2012041.

Binley, A., Hubbard, S.S., Huisman, J.A., Revil, A., Robinson, D.A., Singha, K., Slater, L.D., 2015. The emergence of hydrogeophysics for improved understanding of subsurface processes over multiple scales. Water Resour. Res. 51(6): 3837-3866. doi:10.1002/2015WR017016.

Binley, A., Winship, P., Middleton, R., Pokar, M., West, J., 2001. High-resolution characterization of vadose zone dynamics using cross-borehole radar. Water Resour. Res. 37(11): 2639-2652. doi:10.1029/2000WR000089.

Blanco-Canqui, H., Lai, R., 2007. Impacts of long-term wheat straw management on soil hydraulic properties under no-tillage. Soil Sci. Soc. Am. J. 71(4): 1166-1173. doi:10.2136/ss saj2006.0411.

Blonquist Jr., J.M., Jones, S.B., Robinson, D.A., 2006. Precise irrigation scheduling for turfgrass using a subsurface electromagnetic soil moisture sensor. Agric. Water Manag. 84(1): 153-165. doi:10.1016/j.agwat.2006.01.014.

Blonquist Jr., J.M., Jones, S.B., Robinson, D.A., 2005. Standardizing characterization of electromagnetic water Content Sensors: Part 2. Evaluation of seven sensing systems. Vadose Zone J. 4(4): 1059-1069. doi:10.2136/vzj2004.0141.

Bogena, H.R., Herbst, M., Huisman, J.A., Rosenbaum, U., Weuthen, A., Vereecken, H., 2010. Potential of wireless sensor networks for measuring soil water content variability. Vadose Zone J. 9(4): 1002-1013. doi:10.2136/vzj2009.0173.

Bogena, H.R., Huisman, J.A., Oberdörster, C., Vereecken, H., 2007. Evaluation of a low-cost soil water content sensor for wireless network applications. J. Hydrol. 344(1): 32-42. doi:10.1016/j.jhydrol.2007.06.032.

Bradford, J.H., Dickins, D.F., Brandvik, P.J., 2010. Assessing the potential to detect oil spills in and under snow using airborne ground-penetrating radar. Geophysics. 75(2): G1-G12. doi:10.1190/1.3312184.

Brossier, R., Operto, S., Virieux, J., 2009. Seismic imaging of complex onshore structures by 2D elastic frequency-domain full-waveform inversion. Geophysics. 74(6): WCC105-WCC118. doi:10.1190/1.3215771.

Brosten, T.R., Day-Lewis, F.D., Schultz, G.M., Curtis, G.P., Lane, J.W., 2011. Inversion of multi-frequency electromagnetic induction data for 3D characterization of hydraulic conductivity. J. Appl. Geophy. 73(4): 323-335. doi:10.1016/j.jappgeo.2011.02.004.

Brunet, P., Clément, R., Bouvier, C., 2010. Monitoring soil water content and deficit using Electrical Resistivity Tomography (ERT) – A case study in the Cevennes area, France. J. Hydrol. 380(1): 146-153. doi:10.1016/j.jhydrol.2009.10.032.

Busch, S., van der Kruk, J., Bikowski, J., Vereecken, H., 2012. Quantitative conductivity and permittivity estimation using full-waveform inversion of on-ground GPR data. Geophysics. 77(6): H79-H91. doi:10.1190/geo2012-0045.1.

Busch, S., Weihermüller, L., Huisman, J.A., Steelman, C.M., Endres, A.L., Vereecken, H., van der Kruk, J., 2013. Coupled hydrogeophysical inversion of time-lapse surface GPR data to estimate hydraulic properties of a layered subsurface. Water Resour. Res. 49(12): 8480-8494. doi:10.1002/2013wr013992.

Busch, S., van der Kruk, J., Vereecken, H., 2014. Improved characterization of fine-texture soils using on-ground GPR full-waveform inversion. IEEE Trans. Geosci. Remote Sens. 52(7): 3947-3958. doi:10.1109/TGRS.2013.2278297.

Cai, G., Vanderborght, J., Couvreur, V., Mboh, C.M., Vereecken, H., 2018a. Parameterization of root water uptake models considering dynamic root distributions and water uptake compensation. Vadose Zone J. 17(1): 160125. doi:10.2136/vzj2016.12.0125.

Cai, G., Vanderborght, J., Klotzsche, A., van der Kruk, J., Neumann, J., Hermes, N., Vereecken, H., 2016. Construction of minirhizotron facilities for investigating root zone processes. Vadose Zone J. 15(9): 1-13. doi:10.2136/vzj2016.05.0043.

Cai, G., Vanderborght, J., Langensiepen, M., Schnepf, A., Hüging, H., Vereecken, H., 2018b. Root growth, water uptake, and sap flow of winter wheat in response to different soil water conditions. Hydrol. Earth Syst. Sci. 22(4): 2449-2470. doi:10.5194/hess-22-2449-2018.

Cao, Q., Song, X., Wu, H., Gao, L., Liu, F., Yang, S., Zhang, G., 2020. Mapping the response of volumetric soil water content to an intense rainfall event at the field scale using GPR. J. Hydrol. 583: 124605. doi:10.1016/j.jhydrol.2020.124605.

Cassiani, G., Giustiniani, M., Ferraris, S., Deiana, R., Strobbia, C., 2009. Time-lapse surface-to-surface GPR measurements to monitor a controlled infiltration experiment. Boll. di Geofis. Teor. 50: 209-226.

Cataldo, A., Tarricone, L., Attivissimo, F., Trotta, A., 2007. A TDR method for real-time monitoring of liquids. IEEE Trans. Instrum. Meas. 56(5): 1616-1625. doi:10.1109/TIM.2007.903596.

Chambers, J.E., Gunn, D.A., Wilkinson, P.B., Meldrum, P.I., Haslam, E., Holyoake, S., Kirkham, M., Kuras, O., Merritt, A., Wragg, J., 2014. 4D electrical resistivity tomography monitoring of soil moisture dynamics in an operational railway embankment. Near Surf. Geophys. 12(1): 61-72. doi:10.3997/1873-0604.2013002.

Chanasyk, D.S., Naeth, M.A., 1996. Field measurement of soil moisture using neutron probes. Can. J. Soil Sci. 76(3): 317-323. doi:10.4141/cjss96-038.

Chen, C., Wagenet, R.J., 1992. Simulation of water and chemicals in macropore soils Part 1. Representation of the equivalent macropore influence and its effect on soilwater flow. J. Hydrol. 130(1): 105-126. doi:10.1016/0022-1694(92)90106-6.

Chen, J., Hubbard, S., Rubin, Y., 2001. Estimating the hydraulic conductivity at the south oyster site from geophysical tomographic data using Bayesian techniques based on the normal linear regression model. Water Resour. Res. 37(6): 1603-1613. doi:10.1029/2000wr900392.

Chen, J., Hubbard, S., Rubin, Y., Murray, C., Roden, E., Majer, E., 2004. Geochemical characterization using geophysical data and Markov Chain Monte Carlo methods: A case study at the South Oyster bacterial transport site in Virginia. Water Resour. Res. 40(12). doi:10.1029/2003wr002883.

Chu, W., Gao, X., Sorooshian, S., 2010. Improving the shuffled complex evolution scheme for optimization of complex nonlinear hydrological systems: Application to the calibration of the Sacramento soil-moisture accounting model. Water Resour. Res. 46(9). doi:10.1029/2010wr009224.

Corwin, D.L., Scudiero, E., 2020. Field-scale apparent soil electrical conductivity. Soil Sci. Soc. Am. J. 84(5): 1405-1441. doi:10.1002/saj2.20153.

Dafflon, B., Irving, J., Barrash, W., 2011. Inversion of multiple intersecting high-resolution crosshole GPR profiles for hydrological characterization at the Boise Hydrogeophysical Research Site. J. Appl. Geophy. 73(4): 305-314. doi:10.1016/j.jappgeo.2011.02.001.

Dal Bo, I., Klotzsche, A., Schaller, M., Ehlers, T.A., Kaufmann, M.S., Fuentes Espoz, J.P., Vereecken, H., van der Kruk, J., 2019. Geophysical imaging of regolith in landscapes along a climate and vegetation gradient in the Chilean coastal cordillera. Catena. 180: 146-159. doi:10.1016/j.catena.2019.04.023.

Dalton, F.N., Herkelrath, W.N., Rawlins, D.S., Rhoades, J.D., 1984. Time-domain reflectometry: simultaneous measurement of soil water content and electrical conductivity with a single probe. Science. 224(4652): 989. doi:10.1126/science.224.4652.989.

Daniels, D.J., 2005, Ground penetrating radar, Encyclopedia of RF and Microwave Engineering. doi:10.1002/0471654507.eme152.

Davis, J.L., Annan, A.P., 1989. Ground-penetrating radar for high-resolution mapping of soil and rock stratigraphy. Geophys. Prospect. 37(5): 531-551. doi:10.1111/j.1365-2478.1989.tb02221.x.

Dean, T.J., Bell, J.P., Baty, A.J.B., 1987. Soil moisture measurement by an improved capacitance technique, Part I. Sensor design and performance. J. Hydrol. 93(1): 67-78. doi:10.1016/0022-1694(87)90194-6.

Di Prima, S., Lassabatere, L., Bagarello, V., Iovino, M., Angulo-Jaramillo, R., 2016. Testing a new automated single ring infiltrometer for Beerkan infiltration experiments. Geoderma. 262: 20-34. doi:10.1016/j.geoderma.2015.08.006.

Dix, C.H., 1955. Seismic velocities from surface measurements. Geophysics. 20(1): 68-86. doi:10.1190/1.1438126.

Doetsch, J., Linde, N., Coscia, I., Greenhalgh, S.A., Green, A.G., 2010. Zonation for 3D aquifer characterization based on joint inversions of multimethod crosshole geophysical data. Geophysics. 75(6): G53-G64. doi:10.1190/1.3496476.

Domenzain, D., Bradford, J., Mead, J., 2020. Joint inversion of full-waveform GPR and ER data enhanced by the envelope transform and cross-gradients, 18th International Conference on Ground Penetrating Radar, Golden, Colorado, 14?19 June 2020. SEG Global Meeting Abstracts. Society of Exploration Geophysicists, pp. 332-335. doi:10.1190/gpr2020-087.110.1190/gpr2020-087.1.

Duan, Q., Sorooshian, S., Gupta, V.K., 1994. Optimal use of the SCE-UA global optimization method for calibrating watershed models. J. Hydrol. 158(3): 265-284. doi:10.1016/0022-1694(94)90057-4.

Duan, Q.Y., Gupta, V.K., Sorooshian, S., 1993. Shuffled complex evolution approach for effective and efficient global minimization. J. Optimiz. Theory App. 76(3): 501-521. doi:10.1s007/BF00939380.

Eaton, J.W., 2012. GNU Octave and reproducible research. J. Process Control. 22(8): 1433-1438. doi:10.1016/j.jprocont.2012.04.006.

Fatehnia, M., Paran, S., Kish, S., Tawfiq, K., 2016. Automating double ring infiltrometer with an Arduino microcontroller. Geoderma. 262: 133-139. doi:10.1016/j.geoderma.2015.08.022.

Fisher, E., McMechan, G.A., Annan, A.P., 1992. Acquisition and processing of wide-aperture ground-penetrating radar data. Geophysics. 57(3): 495-504. doi:10.1190/1.1443265.

Franz, T.E., Zreda, M., Ferre, T.P.A., Rosolem, R., 2013. An assessment of the effect of horizontal soil moisture heterogeneity on the area-average measurement of cosmic-ray neutrons. Water Resour. Res. 49(10): 6450-6458. doi:10.1002/wrcr.20530.

Galagedara, L., Parkin, G., Redman, J., Endres, A., 2002. Temporal and spatial variation of soil water content measured by borehole GPR under irrigation and drainage, Ninth International Conference on Ground Penetrating Radar (GPR2002). SPIE, pp. 180–185. doi:10.1117/12.462253.

Galagedara, L.W., Redman, J.D., Parkin, G.W., Annan, A.P., Endres, A.L., 2005a. Numerical modelling of GPR to determine the direct ground wave sampling depth. Vadose Zone J. 4(4): 1096-1106. doi:10.2136/vzj2004.0143.

Galagedara, L.W., Parkin, G.W., Redman, J.D., 2005b. Measuring and modelling of direct ground wave depth penetration under transient soil moisture conditions. Subsurf. Sens. Technol. Appl. 6(2): 193-205. doi:10.1007/s11220-005-0006-z.

Giannopoulos, A., 2005. Modelling ground penetrating radar by GprMax. Constr. Build Mater. 19(10): 755-762. doi:10.1016/j.conbuildmat.2005.06.007.

Gleick, P.H., 1993. Water in crisis. Pacific Institute for Studies in Dev., Environment & Security. Stockholm Env. Institute, Oxford Univ. Press. 473p. 9: 1051-0761.

Greco, R., 2006. Soil water content inverse profiling from single TDR waveforms. J. Hydrol. 317(3): 325-339. doi:10.1016/j.jhydrol.2005.05.024.

Grote, K., Anger, C., Kelly, B., Hubbard, S., Rubin, Y., 2010. Characterization of soil water content variability and soil texture using GPR groundwave techniques. J. Environ. Eng. Geophys. 15(3): 93-110. doi:10.2113/JEEG15.3.93.

Grote, K., Hubbard, S., Harvey, J., Rubin, Y., 2005. Evaluation of infiltration in layered pavements using surface GPR reflection techniques. J. Appl. Geophy. 57(2): 129-153. doi:10.1016/j.jappgeo.2004.10.002.

Grote, K., Hubbard, S., Rubin, Y., 2003. Field-scale estimation of volumetric water content using ground-penetrating radar ground wave techniques. Water Resour. Res. 39(11). doi:10.1029/2003wr002045.

Gueting, N., Vienken, T., Klotzsche, A., van der Kruk, J., Vanderborght, J., Caers, J., Vereecken, H., Englert, A., 2017. High resolution aquifer characterization using crosshole GPR full-waveform tomography: Comparison with direct-push and tracer test data. Water Resour. Res. 53(1): 49-72. doi:10.1002/2016WR019498.

Hartmann, A., Goldscheider, N., Wagener, T., Lange, J., Weiler, M., 2014. Karst water resources in a changing world: Review of hydrological modelling approaches. Rev. Geophys. 52(3): 218-242. doi:10.1002/2013rg000443.

Hinnell, A.C., Ferré, T.P.A., Vrugt, J.A., Huisman, J.A., Moysey, S., Rings, J., Kowalsky, M.B., 2010. Improved extraction of hydrologic information from geophysical data through coupled hydrogeophysical inversion. Water Resour. Res. 46(4). doi:10.1029/2008wr007060.

Holliger, K., Musil, M., Maurer, H.R., 2001. Ray-based amplitude tomography for crosshole georadar data: a numerical assessment. J. Appl. Geophy. 47(3): 285-298. doi:10.1016/S0926-9851(01)00072-6.

Hsieh, P.A., Tracy, J.V., Neuzil, C.E., Bredehoeft, J.D., Silliman, S.E., 1981. A transient laboratory method for determining the hydraulic properties of 'tight' rocks - I. Theory. International Journal of Rock Mechanics and Mining Sciences & Geomechanics Abstracts. 18(3): 245-252. doi:10.1016/0148-9062(81)90979-7.

Hubbard, S.S., Rubin, Y., 2000. Hydrogeological parameter estimation using geophysical data: a review of selected techniques. J. Contam. Hydrol. 45(1): 3-34. doi:10.1016/S0169-7722(00)00117-0.

Huisman, J.A., Hubbard, S.S., Redman, J.D., Annan, A.P., 2003a. Measuring soil water content with ground penetrating radar: A Review. Vadose Zone J. 2(4): 476-491. doi:10.2136/vzj2003.4760.

Huisman, J.A., Rings, J., Vrugt, J.A., Sorg, J., Vereecken, H., 2010. Hydraulic properties of a model dike from coupled Bayesian and multi-criteria hydrogeophysical inversion. J. Hydrol. 380(1): 62-73. doi:10.1016/j.jhydrol.2009.10.023.

Huisman, J.A., Snepvangers, J.J.J.C., Bouten, W., Heuvelink, G.B.M., 2002. Mapping spatial variation in surface soil water content: comparison of ground-penetrating radar and time domain reflectometry. J. Hydrol. 269(3): 194-207. doi:10.1016/S0022-1694(02)00239-1.

Huisman, J.A., Snepvangers, J.J.J.C., Bouten, W., Heuvelink, G.B.M., 2003b. Monitoring temporal development of spatial soil water content variation: comparison of ground penetrating radar and time domain reflectometry. Vadose Zone J. 2(4): 519-529. doi:10.2136/vzj2003.5190.

Huisman, J.A., Sperl, C., Bouten, W., Verstraten, J.M., 2001. Soil water content measurements at different scales: accuracy of time domain reflectometry and ground-penetrating radar. J. Hydrol. 245(1): 48-58. doi:10.1016/S0022-1694(01)00336-5.

Ihamouten, A., Bosc, F., Guan, B., Le Bastard, C., Fauchard, C., Lambot, S., Dérobert, X., 2018. Full-waveform inversion using a stepped-frequency GPR to characterize the tack coat in hot-mix asphalt (HMA) layers of flexible pavements. NDT E Int. 95: 17-25. doi:10.1016/j.ndteint.2017.12.006.

Irving, J.D., Knoll, M.D., Knight, R.J., 2007. Improving crosshole radar velocity tomograms: A new approach to incorporating high-angle traveltime data. Geophysics. 72(4): J31-J41. doi:10.1190/1.2742813.

Iwasaki, T., Kuroda, S., Saito, H., Tobe, Y., Suzuki, K., Fujimaki, H., Inoue, M., 2016. Monitoring infiltration process seamlessly using array ground penetrating radar. Agric. Ecosyst. Environ. 1(1): 160002. doi:10.2134/ael2016.01.0002.

Jadoon, K.Z., Weihermüller, L., Scharnagl, B., Kowalsky, M.B., Bechtold, M., Hubbard, S.S., Vereecken, H., Lambot, S., 2012. Estimation of soil hydraulic parameters in the field by integrated hydrogeophysical inversion of time-lapse ground-penetrating radar data. Vadose Zone J. 11(4): vzj2011.0177. doi:10.2136/vzj2011.0177.

Jaumann, S., Roth, K., 2018. Soil hydraulic material properties and layered architecture from time-lapse GPR. Hydrol. Earth Syst. Sci. 22(4): 2551-2573. doi:10.5194/hess-22-2551-2018.

Jhorar, R.K., Smit, A.A.M.F.R., Roest, C.W.J., 2009. Assessment of alternative water management options for irrigated agriculture. Agric. Water Manag. 96(6): 975-981. doi:10.1016/j.agwat.2009.01.009.

Jonard, F., Weihermüller, L., Schwank, M., Jadoon, K.Z., Vereecken, H., Lambot, S., 2015. Estimation of hydraulic properties of a sandy soil using ground-based active and passive microwave remote sensing. IEEE Trans. Geosci. Remote Sens. 53(6): 3095-3109. doi:10.1109/TGRS.2014.2368831.

Jonard, F., Weihermüller, L., Vereecken, H., Lambot, S., 2012. Accounting for soil surface roughness in the inversion of ultrawideband off-ground GPR signal for soil moisture retrieval. Geophysics. 77(1): H1-H7. doi:10.1190/geo2011-0054.1.

Jouen, T., Clément, R., Henine, H., Chaumont, C., Vincent, B., Tournebize, J., 2018. Evaluation and localization of an artificial drainage network by 3D time-lapse electrical resistivity tomography. Environ. Sci. Pollut. Res. 25(24): 23502-23514. doi:10.1007/s11356-016-7366-x.

Jülich Supercomputing Centre, 2018. Jureca: Modular supercomputer at Jülich supercomputing centre. J. Large-Scale Res. Fac. 4: 132. doi:10.17815/jlsrf-4-121-1.

Katul, G.G., Wendroth, O., Parlange, M.B., Puente, C.E., Folegatti, M.V., Nielsen, D.R., 1993. Estimation of in situ hydraulic conductivity function from nonlinear filtering theory. Water Resour. Res. 29(4): 1063-1070. doi:10.1029/92wr02593.

Kaufmann, M.S., Klotzsche, A., Vereecken, H., van der Kruk, J., 2020. Simultaneous multichannel multi-offset ground-penetrating radar measurements for soil characterization. Vadose Zone J. 19(1): e20017. doi:10.1002/vzj2.20017.

Kelter, M., Huisman, J.A., Zimmermann, E., Vereecken, H., 2018. Field evaluation of broadband spectral electrical imaging for soil and aquifer characterization. J. Appl. Geophy. 159: 484-496. doi:10.1016/j.jappgeo.2018.09.029.

Kemna, A., Vanderborght, J., Kulessa, B., Vereecken, H., 2002. Imaging and characterisation of subsurface solute transport using electrical resistivity tomography (ERT) and equivalent transport models. J. Hydrol. 267(3): 125-146. doi:10.1016/S0022-1694(02)00145-2.

Klotzsche, A., Jonard, F., Looms, M.C., van der Kruk, J., Huisman, J.A., 2018. Measuring soil water content with ground penetrating radar: A decade of progress. Vadose Zone J. 17(1): 180052. doi:10.2136/vzj2018.03.0052.

Klotzsche, A., van der Kruk, J., He, G., Vereecken, H., 2016. GPR full-waveform inversion of horizontal ZOP borehole data using GprMax, 2016 16th International Conference on Ground Penetrating Radar (GPR), pp. 1-5. doi:10.1109/ICGPR.2016.7572695.

Klotzsche, A., van der Kruk, J., Linde, N., Doetsch, J., Vereecken, H., 2013. 3-D characterization of high-permeability zones in a gravel aquifer using 2-D crosshole GPR full-waveform inversion and waveguide detection. Geophys. J. Int. 195(2): 932-944. doi:10.1093/gji/ggt275.

Klotzsche, A., Lärm, L., Vanderborght, J., Cai, G., Morandage, S., Zörner, M., Vereecken, H., van der Kruk, J., 2019a. Monitoring soil water content using time-lapse horizontal borehole GPR data at the field-plot scale. Vadose Zone J. 18(1): 190044. doi:10.2136/vzj2019.05.0044.

Klotzsche, A., van der Kruk, J., Angelo Meles, G., Doetsch, J., Maurer, H., Linde, N., 2010. Full-waveform inversion of cross-hole ground-penetrating radar data to characterize a gravel aquifer close to the Thur River, Switzerland. Near Surf. Geophys. 8(6): 635-649. doi:10.3997/1873-0604.2010054.

Klotzsche, A., van der Kruk, J., Bradford, J., Vereecken, H., 2014. Detection of spatially limited high-porosity layers using crosshole GPR signal analysis and full-waveform inversion. Water Resour. Res. 50(8): 6966-6985. doi:10.1002/2013WR015177.

Klotzsche, A., Vereecken, H., van der Kruk, J., 2019b. Review of crosshole ground-penetrating radar full-waveform inversion of experimental data: Recent developments, challenges, and pitfalls. Geophysics. 84(6): H13-H28. doi:10.1190/geo2018-0597.1.

Klute, A., Dirksen, C., 1986. Hydraulic conductivity and diffusivity: Laboratory methods. Methods of Soil Analysis: Part 1 Physical and Mineralogical Methods. 5: 687-734.

Knight, R., 2001. Ground penetrating radar for environmental applications. Annu. Rev. Earth Planet Sci. 29: 229-255.

Köhli, M., Schrön, M., Zreda, M., Schmidt, U., Dietrich, P., Zacharias, S., 2015. Footprint characteristics revised for field-scale soil moisture monitoring with cosmic-ray neutrons. Water Resour. Res. 51(7): 5772-5790. doi:10.1002/2015WR017169.

Kool, J.B., Parker, J.C., 1988. Analysis of the inverse problem for transient unsaturated flow. Water Resour. Res. 24(6): 817-830. doi:10.1029/WR024i006p00817.

Kool, J.B., Parker, J.C., van Genuchten, M.T., 1987. Parameter estimation for unsaturated flow and transport models - A review. J. Hydrol. 91(3): 255-293. doi:10.1016/0022-1694(87)902 07-1.

Kowalsky, M.B., Finsterle, S., Peterson, J., Hubbard, S., Rubin, Y., Majer, E., Ward, A., Gee, G., 2005. Estimation of field-scale soil hydraulic and dielectric parameters through joint inversion of GPR and hydrological data. Water Resour. Res. 41(11). doi:10.1029/2005wr004237.

Kuczera, G., Mroczkowski, M., 1998. Assessment of hydrologic parameter uncertainty and the worth of multiresponse data. Water Resour. Res. 34(6): 1481-1489. doi:10.1029/98WR00496.

Kumar, S., Sekhar, M., Reddy, D.V., Mohan Kumar, M.S., 2010. Estimation of soil hydraulic properties and their uncertainty: comparison between laboratory and field experiment. Hydrol. Process. 24(23): 3426-3435. doi:10.1002/hyp.7775.

Lai, J., Ren, L., 2007. Assessing the size dependency of measured hydraulic conductivity using double-ring infiltrometers and numerical simulation. Soil Sci. Soc. Am. J. 71(6): 1667-1675. doi:10.2136/sssaj2006.0227.

Lambot, S., André, F., 2014. Full-wave modelling of near-field radar data for planar layered media reconstruction. IEEE Trans. Geosci. Remote Sens. 52(5): 2295-2303. doi:10.1109/TGR S.2013.2259243.

Lambot, S., Antoine, M., Vanclooster, M., Slob, E.C., 2006a. Effect of soil roughness on the inversion of off-ground monostatic GPR signal for noninvasive quantification of soil properties. Water Resour. Res. 42(3). doi:10.1029/2005wr004416.

Lambot, S., Rhebergen, J., van den Bosch, I., Slob, E.C., Vanclooster, M., 2004. Measuring the soil water content profile of a sandy soil with an off-ground monostatic ground penetrating radar. Vadose Zone J. 3(4): 1063-1071. doi:10.2136/vzj2004.1063.

Lambot, S., Slob, E., Rhebergen, J., Lopera, O., Jadoon, K.Z., Vereecken, H., 2009. Remote estimation of the hydraulic properties of a sand using full-waveform integrated hydrogeophysical inversion of time-Lapse, off-Ground GPR data. Vadose Zone J. 8(3): 743-754. doi:10.2136/vzj2008.0058.

Lambot, S., Slob, E.C., Vanclooster, M., Vereecken, H., 2006b. Closed loop GPR data inversion for soil hydraulic and electric property determination. Geophys. Res. Lett. 33(21). doi:10.1029/2006GL027906.

Leng, Z., Al-Qadi, I.L., 2014. An innovative method for measuring pavement dielectric constant using the extended CMP method with two air-coupled GPR systems. NDT E Int. 66: 90-98. doi:10.1016/j.ndteint.2014.05.002.

Li, D., Xu, K., Harris, J.M., Darve, E., 2020. Coupled time-lapse full-waveform inversion for subsurface flow problems using intrusive automatic differentiation. Water Resour. Res. 56(8): e2019WR027032. doi:10.1029/2019wr027032.

Liu, T., Klotzsche, A., Pondkule, M., Vereecken, H., Su, Y., van der Kruk, J., 2018. Radius estimation of subsurface cylindrical objects from ground-penetrating-radar data using full-waveform inversion. Geophysics. 83(6): H43-H54. doi:10.1190/geo2017-0815.1.

Liu, X., Chen, J., Cui, X., Liu, Q., Cao, X., Chen, X., 2019. Measurement of soil water content using ground-penetrating radar: a review of current methods. Int. J. Digit. Earth 12(1): 95-118. doi:10.1080/17538947.2017.1412520.

Loague, K., Green, R.E., 1991. Statistical and graphical methods for evaluating solute transport models: Overview and application. J. Contam. Hydrol. 7(1): 51-73. doi:10.1016/0169-7722(91)90038-3.

Loeffler, O., Bano, M., 2004. Ground penetrating radar measurements in a controlled vadose Zone: Influence of the water content. Vadose Zone J. 3(4): 1082-1092. doi:10.2136/vzj2004.1082.

Looms, M.C., Binley, A., Jensen, K.H., Nielsen, L., Hansen, T.M., 2008a. Identifying unsaturated hydraulic parameters using an integrated data fusion approach on cross-borehole geophysical data. Vadose Zone J. 7(1): 238-248. doi:10.2136/vzj2007.0087.

Looms, M.C., Jensen, K.H., Binley, A., Nielsen, L., 2008b. Monitoring unsaturated flow and transport using cross-borehole geophysical methods. Vadose Zone J. 7(1): 227-237. doi: 10.2136/vzj2006.0129.

Looms, M.C., Klotzsche, A., van der Kruk, J., Larsen, T.H., Edsen, A., Tuxen, N., Hamburger, N., Keskinen, J., Nielsen, L., 2017. Mapping sand layers in clayey till using crosshole ground-penetrating radar. Geophysics. 83(1): A21-A26. doi:10.1190/geo2017-0297.1.

Lunt, I.A., Hubbard, S.S., Rubin, Y., 2005. Soil moisture content estimation using ground-penetrating radar reflection data. J. Hydrol. 307(1): 254-269. doi:10.1016/j.jhydrol.2004.10.014.

Mahmoudzadeh Ardekani, M.R., 2013. Off- and on-ground GPR techniques for field-scale soil moisture mapping. Geoderma. 200-201: 55-66. doi:10.1016/j.geoderma.2013.02.010.

Mahmoudzadeh Ardekani, M.R., Jacques, D.C., Lambot, S., 2016. A layered vegetation model for GPR full-wave inversion. IEEE J. Sel. Top. Appl. Earth Obs. Remote Sens. 9(1): 18-28. doi:10.1109/JSTARS.2015.2418093.

Malicki, M.A., Plagge, R., Renger, M., Walczak, R.T., 1992. Application of time-domain reflectometry (TDR) soil moisture miniprobe for the determination of unsaturated soil water characteristics from undisturbed soil cores. Irrig. Sci. 13(2): 65-72. doi:10.1007/BF00193982.

Mangel, A.R., Moysey, S.M.J., Bradford, J., 2020. Reflection tomography of time-lapse GPR data for studying dynamic unsaturated flow phenomena. Hydrol. Earth Syst. Sci. 24(1): 159-167. doi:10.5194/hess-24-159-2020.

Mangel, A.R., Moysey, S.M.J., Ryan, J.C., Tarbutton, J.A., 2012. Multi-offset ground-penetrating radar imaging of a lab-scale infiltration test. Hydrol. Earth Syst. Sci. 16(11): 4009-4022. doi:10.5194/hess-16-4009-2012.

Mangel, A.R., Moysey, S.M.J., van der Kruk, J., 2015. Resolving precipitation induced water content profiles by inversion of dispersive GPR data: A numerical study. J. Hydrol. 525: 496-505. doi:10.1016/j.jhydrol.2015.04.011.

Mangel, A.R., Moysey, S.M.J., van der Kruk, J., 2017. Resolving infiltration-induced water content profiles by inversion of dispersive ground-penetrating radar data. Vadose Zone J. 16(10): vzj2017.02.0037. doi:10.2136/vzj2017.02.0037.

Manoli, G., Rossi, M., Pasetto, D., Deiana, R., Ferraris, S., Cassiani, G., Putti, M., 2015. An iterative particle filter approach for coupled hydro-geophysical inversion of a controlled infiltration experiment. J. Comput. Phys. 283: 37-51. doi:10.1016/j.jcp.2014.11.035.

Martínez-Vilalta, J., Piñol, J., Beven, K., 2002. A hydraulic model to predict drought-induced mortality in woody plants: an application to climate change in the Mediterranean. Ecol. Modell. 155(2): 127-147. doi:10.1016/S0304-3800(02)00025-X.

Mboh, C.M., Huisman, J.A., Van Gaelen, N., Rings, J., Vereecken, H., 2012. Coupled hydrogeophysical inversion of electrical resistances and inflow measurements for topsoil hydraulic properties under constant head infiltration. Near Surf. Geophys. 10(5): 413-426. doi:10.3997/1873-0604.2012009.

Mboh, C.M., Huisman, J.A., Vereecken, H., 2011. Feasibility of sequential and coupled inversion of time domain reflectometry data to infer soil hydraulic parameters under falling head infiltration. Soil Sci. Soc. Am. J. 75(3): 775-786. doi:10.2136/sssaj2010.0285.

McDowell, N.G., Allen, C.D., 2015. Darcy's law predicts widespread forest mortality under climate warming. Nat. Clim. Chang. 5(7): 669-672. doi:10.1038/nclimate2641.

Meles, G.A., van der Kruk, J., Greenhalgh, S.A., Ernst, J.R., Maurer, H., Green, A.G., 2010. A new vector waveform inversion algorithm for simultaneous updating of conductivity and permittivity parameters from combination crosshole/borehole-to-surface GPR data. IEEE Trans. Geosci. Remote Sens. 48(9): 3391-3407. doi:10.1109/TGRS.2010.2046670.

Minet, J., Laloy, E., Lambot, S., Vanclooster, M., 2011. Effect of high-resolution spatial soil moisture variability on simulated runoff response using a distributed hydrologic model. Hydrol. Earth Syst. Sci. 15(4): 1323-1338. doi:10.5194/hess-15-1323-2011.

Moghadas, D., Jadoon, K.Z., Vanderborght, J., Lambot, S., Vereecken, H., 2013. Effects of near surface soil moisture profiles during evaporation on far-field ground-penetrating radar data: A numerical study. Vadose Zone J. 12(2): vzj2012.0138. doi:10.2136/vz j2012.0138.

Moghadas, D., Jadoon, K.Z., McCabe, M.F., 2017. Spatiotemporal monitoring of soil water content profiles in an irrigated field using probabilistic inversion of time-lapse EMI data. Adv. Water Resour. 110: 238-248. doi: 10.1016/j.advwatres.2017.10.019.

Moysey, S.M., 2010. Hydrologic trajectories in transient ground-penetrating-radar reflection data. Geophysics. 75(4): WA211-WA219. doi:10.1190/1.3463416.

Mualem, Y., 1976. A new model for predicting the hydraulic conductivity of unsaturated porous media. Water Resour. Res. 12(3): 513-522. doi:10.1029/WR012i003p00513.

Nandagiri, L., Prasad, R., 1996. Field evaluation of unsaturated hydraulic conductivity models and parameter estimation from retention data. J. Hydrol. 179(1): 197-205. doi:10.1016/0022-1694(95)02840-4.

Neuzil, C.E., Cooley, C., Silliman, S.E., Bredehoeft, J.D., Hsieh, P.A., 1981. A transient laboratory method for determining the hydraulic properties of ‘tight’ rocks - II. Application, International Journal of Rock Mechanics and Mining Sciences & Geomechanics Abstracts, pp. 253-258. doi:10.1016/0148-9062(81)90980-3.

Noborio, K., 2001. Measurement of soil water content and electrical conductivity by time domain reflectometry: a review. Comput. Electron. Agric. 31(3): 213-237. doi:10.1016/S0168-1699(00)00184-8.

Oki, T., Kanae, S., 2006. Global hydrological cycles and world water resources. Science. 313(5790): 1068-1072.

Paltineanu, I.C., Starr, J.L., 2000. Preferential water flow through corn canopy and soil water dynamics across rows. Soil Sci. Soc. Am. J. 64(1): 44-54. doi:10.2136/sssaj2000.64144x.

Pan, X., Zhang, J., Huang, P., Roth, K., 2012. Estimating field-scale soil water dynamics at a heterogeneous site using multi-channel GPR. Hydrol. Earth Syst. Sci. 16(11): 4361-4372. doi:10.5194/hess-16-4361-2012.

Park, C.B., Miller, R.D., Xia, J., Imaging dispersion curves of surface waves on multi-channel record, SEG Technical Program Expanded Abstracts 1998, pp. 1377-1380. doi:10.1190/1.1820161.

Peterson, J.E. Jr., 2001. Pre-inversion corrections and analysis of radar tomographic data. J. Environ. Eng. Geophys. 6(1): 1-18. doi:10.4133/JEEG6.1.1.

Pollock, D., Cirpka, O.A., 2010. Fully coupled hydrogeophysical inversion of synthetic salt tracer experiments. Water Resour. Res. 46(7). doi:10.1029/2009wr008575.

Porsani, J.L., Ruy, Y.B., Ramos, F.P., Yamanouth, G.R.B., 2012. GPR applied to mapping utilities along the route of the Line 4 (yellow) subway tunnel construction in São Paulo City, Brazil. J. Appl. Geophy. 80: 25-31. doi:10.1016/j.jappgeo.2012.01.001.

Prieksat, M.A., Ankeny, M.D., Kaspar, T.C., 1992. Design for an automated, self-regulating, single-ring infiltrometer. Soil Sci. Soc. Am. J. 56(5): 1409-1411. doi:10.2136/sssaj1992.03615995005600050013x.

Qu, W., Bogena, H.R., Huisman, J.A., Vereecken, H., 2013. Calibration of a novel low-cost soil water content sensor based on a ring oscillator. Vadose Zone J. 12(2): vzj2012.0139. doi:10.2136/vzj2012.0139.

Redman, D., Parkin, G.W., Annan, A.P., 2000. Borehole GPR measurement of soil water content during an infiltration experiment, Eighth International Conference on Ground Penetrating Radar. International Society for Optics and Photonics, pp. 501-505.

Redman, J.D., Davis, J.L., Galagedara, L.W., Gary, W.P., 2002. Field studies of GPR air launched surface reflectivity measurements of soil water content, Ninth International Conference on Ground Penetrating Radar. Vol. 4758. International Society for Optics and Photonics.

Rejiba, F., Sagnard, F., Schamper, C., Froumentin, M., Guérin, R., 2011. Zero-offset profiling using frequency cross-hole radar in a layered embankment test site: antenna design, simulation and experimental results. Near Surf. Geophys. 9(1): 67-76. doi:10.3997/1873-0604.2010058.

Revil, A., Linde, N., Cerepi, A., Jougnot, D., Matthäi, S., Finsterle, S., 2007. Electrokinetic coupling in unsaturated porous media. J. Colloid Interface Sci. 313(1): 315-327. doi:10.1016/j.jcis.2007.03.037.

Reynolds, W.D., Bowman, B.T., Brunke, R.R., Drury, C.F., Tan, C.S., 2000. Comparison of Tension Infiltrometer, Pressure Infiltrometer, and Soil Core Estimates of Saturated Hydraulic Conductivity. Soil Sci. Soc. Am. J. 64(2): 478-484. doi:10.2136/sssaj2000.642478x.

Reynolds, W.D., Zebchuk, W.D., 1996. Use of contact material in tension infiltrometer measurements. Soil Technol. 9(3): 141-159. doi:10.1016/S0933-3630(96)00009-8.

Rhoades, J.D., Raats, P.A.C., Prather, R.J., 1976. Effects of Liquid-phase Electrical Conductivity, Water Content, and Surface Conductivity on Bulk Soil Electrical Conductivity. Soil Sci. Soc. Am. J. 40(5): 651-655. doi:10.2136/sssaj1976.03615995004000050017x.

Ritter, A., Hupet, F., Muñoz-Carpena, R., Lambot, S., Vanclooster, M., 2003. Using inverse methods for estimating soil hydraulic properties from field data as an alternative to direct methods. Agric. Water Manag. 59(2): 77-96. doi:10.1016/S0378-3774(02)00160-9.

Robinson, D.A., Campbell, C.S., Hopmans, J.W., Hornbuckle, B.K., Jones, S.B., Knight, R., Ogden, F., Selker, J., Wendroth, O., 2008. Soil moisture measurement for ecological and hydrological watershed-scale observatories: A review. Vadose Zone J. 7(1): 358-389. doi:10.2136/vzj2007.0143.

Robinson, D.A., Jones, S.B., Blonquist Jr., J.M., Friedman, S.P., 2005. A physically derived water content/permittivity calibration model for coarse-textured, layered soils. Soil Sci. Soc. Am. J. 69(5): 1372-1378. doi:10.2136/sssaj2004.0366.

Rossi, M., Manoli, G., Pasetto, D., Deiana, R., Ferraris, S., Strobbia, C., Putti, M., Cassiani, G., 2015. Coupled inverse modelling of a controlled irrigation experiment using multiple hydro-geophysical data. Adv. Water Resour. 82: 150-165. doi:10.1016/j.advwatres.2015.03.008.

Roth, K., Schulin, R., Flühler, H., Attinger, W., 1990. Calibration of time domain reflectometry for water content measurement using a composite dielectric approach. Water Resour. Res. 26(10): 2267-2273. doi:10.1029/WR026i010p02267.

Rovey II, C.W., Cherkauer, D.S., 1995. Scale dependency of hydraulic conductivity measurements. Groundwater. 33(5): 769-780. doi:10.1111/j.1745-6584.1995.tb00023.x.

Rucker, D.F., Ferré, T.P.A., 2004a. Correcting water content measurement errors associated with critically refracted first arrivals on zero offset profiling borehole ground penetrating radar profiles. Vadose Zone J. 3(1): 278-287. doi:10.2136/vzj2004.2780.

Rucker, D.F., Ferré, T.P.A., 2004b. Parameter estimation for soil hydraulic properties using zero-offset borehole radar. Soil Sci. Soc. Am. J. 68(5): 1560-1567. doi:10.2136/sssaj2004.1560.

Rutishauser, A., Maurer, H., Bauder, A., 2016. Helicopter-borne ground-penetrating radar investigations on temperate alpine glaciers: A comparison of different systems and their abilities for bedrock mapping. Geophysics. 81(1): WA119-WA129. doi:10.1190/geo2015-0144.1.

Schaap, M.G., Leij, F.J., 2000. Improved prediction of unsaturated hydraulic conductivity with the Mualem - van Genuchten model. Soil Sci. Soc. Am. J. 64(3): 843-851. doi:10.2136/sssaj2000.643843x.

Schmugge, T.J., Jackson, T.J., McKim, H.L., 1980. Survey of methods for soil moisture determination. Water Resour. Res. 16(6): 961-979. doi:10.1029/WR016i006p00961.

Serbin, G., Or, D., 2005. Ground-penetrating radar measurement of crop and surface water content dynamics. Remote Sens. Environ. 96(1): 119-134. doi:10.1016/j.rse.20 05.01.018.

Šimůnek, J., Angulo-Jaramillo, R., Schaap, M.G., Vandervaere, J.-P., van Genuchten, M.T., 1998. Using an inverse method to estimate the hydraulic properties of crusted soils from tension-disc infiltrometer data. Geoderma. 86(1): 61-81. doi:10.1016/S0016-7061(98)00035-4.

Šimůnek, J., van Genuchten, M.T., 1996. Estimating unsaturated soil hydraulic properties from tension disc infiltrometer data by numerical inversion. Water Resour. Res. 32(9): 2683-2696. doi:10.1029/96WR01525.

Šimůnek, J., van Genuchten, M.T., Šejna, M., 2008. Development and applications of the HYDRUS and STANMOD software packages and related codes. Vadose Zone J. 7(2): 587-600. doi:10.2136/vzj2007.0077.

Šimůnek, J., van Genuchten, M.T., Šejna, M., 2016. Recent developments and applications of the HYDRUS computer software packages. Vadose Zone J. 15(7): vzj2016.04.0033. doi:10.2136/vzj2016.04.0033.

Singh, A., 2010. Decision support for on-farm water management and long-term agricultural sustainability in a semi-arid region of India. J. Hydrol. 391(1): 63-76. doi:10.1016/j.jhydrol.2010.07.006.

Singh, A., 2014. Groundwater resources management through the applications of simulation modelling: A review. Sci. Total Environ. 499: 414-423. doi:10.1016/j.scit otenv.2014.05.048.

Slob, E., Sato, M., Olhoeft, G., 2010. Surface and borehole ground-penetrating-radar developments. Geophysics. 75(5): 75A103-75A120. doi:10.1190/1.3480619.

Sonnleitner, M.A., Abbaspour, K.C., Schulin, R., 2003. Hydraulic and transport properties of the plant–soil system estimated by inverse modelling. Eur. J. Soil Sci. 54(1): 127-138. doi:10.1046/j.1365-2389.2002.00491.x.

Steelman, C.M., Endres, A.L., Jones, J.P., 2012. High-resolution ground-penetrating radar monitoring of soil moisture dynamics: Field results, interpretation, and comparison with unsaturated flow model. Water Resour. Res. 48(9). doi:10.1029/2011wr011414.

Steenpass, C., Vanderborght, J., Herbst, M., Šimůnek, J., Vereecken, H., 2010. Estimating soil hydraulic properties from infrared measurements of soil surface temperatures and TDR data. Vadose Zone J. 9(4): 910-924. doi:10.2136/vzj2009.0176.

Strobbia, C., Cassiani, G., 2007. Multilayer ground-penetrating radar guided waves in shallow soil layers for estimating soil water content. Geophysics. 72(4): J17-J29. doi:10.1190/1.2716374.

Tamari, S., Bruckler, L., Halbertsma, J., Chadoeuf, J., 1993. A Simple method for determining soil hydraulic properties in the laboratory. Soil Sci. Soc. Am. J. 57(3): 642-651. doi:10.21 36 /sssaj1993.03615995005700030003x.

Tarantola, A., 1984. Inversion of seismic reflection data in the acoustic approximation. Geophysics. 49(8): 1259-1266. doi:10.1190/1.1441754.

Taylor, R.G., Scanlon, B., Döll, P., Rodell, M., van Beek, R., Wada, Y., Longuevergne, L., Leblanc, M., Famiglietti, J.S., Edmunds, M., Konikow, L., Green, T.R., Chen, J., Taniguchi, M., Bierkens, M.F.P., MacDonald, A., Fan, Y., Maxwell, R.M., Yechieli, Y., Gurdak, J.J., Allen, D.M., Shamsudduha, M., Hiscock, K., Yeh, P.J.F., Holman, I., Treidel, H., 2013. Ground water and climate change. Nat. Clim. Chang. 3(4): 322-329. doi:10.1038/nclimate1744.

Thyer, M., Kuczera, G., Bates, B.C., 1999. Probabilistic optimization for conceptual rainfall-runoff models: A comparison of the shuffled complex evolution and simulated annealing algorithms. Water Resour. Res. 35(3): 767-773. doi:10.1029/1998wr900058.

Toorman, A.F., Wierenga, P.J., Hills, R.G., 1992. Parameter estimation of hydraulic properties from one-step outflow data. Water Resour. Res. 28(11): 3021-3028. doi:10.1029/92wr01272

Topp, G.C., Davis, J.L., 1981. Detecting infiltration of water through soil cracks by time-domain reflectometry. Geoderma. 26(1): 13-23. doi:10.1016/0016-7061(81)90073-2.

Topp, G.C., Davis, J.L., Annan, A.P., 1980. Electromagnetic determination of soil water content: Measurements in coaxial transmission lines. Water Resour. Res. 16(3): 574-582. doi:10.10 29/WR016i003p00574.

Topp, G.C., Ferré, T.P.A., 2005. Time-domain reflectometry, Encyclopedia of Soils in the Environment. Elsevier, Oxford, pp. 174-181. doi:10.1016/B0-12-348530-4/00508-7.

van der Kruk, J., Streich, R., Green, A.G., 2006a. Properties of surface waveguides derived from separate and joint inversion of dispersive TE and TM GPR data. Geophysics. 71(1): K19-K29. doi:10.1190/1.2168011.

van der Kruk, J., 2006b. Properties of surface waveguides derived from inversion of fundamental and higher mode dispersive GPR data. IEEE Trans. Geosci. Remote Sens. 44(10): 2908-2915. doi:10.1109/TGRS.2006.877286.

van der Kruk, J., Jacob, R.W., Vereecken, H., 2010. Properties of precipitation-induced multilayer surface waveguides derived from inversion of dispersive TE and TM GPR data. Geophysics. 75(4): WA263-WA273. doi:10.1190/1.3467444.

van der Kruk, J., Vereecken, H., Jacob, R.W., 2009a. Identifying dispersive GPR signals and inverting for surface wave-guide properties. Lead. Edge. 28(10): 1234-1239. doi:10.1190 /1.3249780.

van der Kruk, J., Steelman, C.M., Endres, A.L., Vereecken, H., 2009b. Dispersion inversion of electromagnetic pulse propagation within freezing and thawing soil waveguides. Geophys. Res. Lett. 36(18). doi:10.1029/2009GL039581.

van Genuchten, M.T., 1980. A Closed-form equation for predicting the hydraulic conductivity of unsaturated soils. Soil Sci. Soc. Am. J. 44(5): 892-898. doi:10.2136/sssaj1980.0361599 5004400050002x.

van Overmeeren, R.A., Sariowan, S.V., Gehrels, J.C., 1997. Ground penetrating radar for determining volumetric soil water content; results of comparative measurements at two test sites. J. Hydrol. 197(1): 316-338. doi:10.1016/S0022-1694(96)03244-1.

Verbist, K., Torfs, S., Cornelis, W.M., Oyarzún, R., Soto, G., Gabriels, D., 2010. Comparison of Single- and Double-Ring Infiltrometer Methods on Stony Soils. Vadose Zone J. 9(2): 462-475. doi:10.2136/vzj2009.0058.

Verbist, K.M.J., Cornelis, W.M., Torfs, S., Gabriels, D., 2013. Comparing methods to determine hydraulic conductivities on stony soils. Soil Sci. Soc. Am. J. 77(1): 25-42. doi:10.2136/sssaj 2012.0025.

Vereecken, H., Huisman, J.A., Bogena, H., Vanderborght, J., Vrugt, J.A., Hopmans, J.W., 2008. On the value of soil moisture measurements in vadose zone hydrology: A review. Water Resour. Res. 44(4). doi:10.1029/2008wr006829.

Vereecken, H., Kasteel, R., Vanderborght, J., Harter, T., 2007. Upscaling hydraulic properties and soil water flow processes in heterogeneous soils: A Review. Vadose Zone J. 6(1): 1-28. doi:10.2136/vzj2006.0055.

Vigh, D., Starr, E.W., 2008. 3D prestack plane-wave, full-waveform inversion. Geophysics. 73(5): VE135-VE144. doi:10.1190/1.2952623.

Virieux, J., Operto, S., 2009. An overview of full-waveform inversion in exploration geophysics. Geophysics. 74(6): WCC1-WCC26. doi:10.1190/1.3238367.

Vrugt, J., Dane, J., 2006. Inverse modelling of Soil hydraulic properties, Encyclopedia of Hydrological Sciences. doi:10.1002/0470848944.hsa079.

Wagner, B.J., 1992. Simultaneous parameter estimation and contaminant source characterization for coupled groundwater flow and contaminant transport modelling. J. Hydrol. 135(1): 275-303. doi:10.1016/0022-1694(92)90092-A.

Warnick, K.F., 2005. An intuitive error analysis for FDTD and comparison to MoM. IEEE Antennas Propag. Mag. 47(6): 111-115. doi:10.1109/MAP.2005.1608751.

Warren, C., Giannopoulos, A., Giannakis, I., 2016. gprMax: Open source software to simulate electromagnetic wave propagation for Ground Penetrating Radar. Comput. Phys. Commun. 209: 163-170. doi:10.1016/j.cpc.2016.08.020.

Wehrhan, A., Kasteel, R., Simunek, J., Groeneweg, J., Vereecken, H., 2007. Transport of sulfadiazine in soil columns - Experiments and modelling approaches. J. Contam. Hydrol. 89(1): 107-135. doi:10.1016/j.jconhyd.2006.08.002.

Weihermüller, L., Huisman, J.A., Hermes, N., Pickel, S., Vereecken, H., 2013. A new TDR multiplexing system for reliable electrical conductivity and soil water content measurements. Vadose Zone J. 12(2): vzj2012.0194. doi:10.2136/vzj2012.0194.

Weihermüller, L., Huisman, J.A., Lambot, S., Herbst, M., Vereecken, H., 2007. Mapping the spatial variation of soil water content at the field scale with different ground penetrating radar techniques. J. Hydrol. 340(3): 205-216. doi:10.1016/j.jhydrol.2007.04.013.

Wessel-Bothe, S., Weihermüller, L., 2020. Field measurement methods in Soil Science. Gebruder Borntraeger Verlagsbuchhandlung, Science Publishers.

Wiwatrojanagul, P., Sahamitmongkol, R., Tangtermsirikul, S., Khamsemanan, N., 2017. A new method to determine locations of rebars and estimate cover thickness of RC structures using GPR data. Constr. Build Mater. 140: 257-273. doi:10.1016/j.conbuildmat.2017.02.126.

Wollschläger, U., Pfaff, T., Roth, K., 2009. Field-scale apparent hydraulic parameterisation obtained from TDR time series and inverse modelling. Hydrol. Earth Syst. Sci. 13(10): 1953-1966. doi:10.5194/hess-13-1953-2009.

Wu, K., Rodriguez, G.A., Zajc, M., Jacquemin, E., Clément, M., De Coster, A., Lambot, S., 2019. A new drone-borne GPR for soil moisture mapping. Remote Sens. Environ. 235: 111456. doi:10.1016/j.rse.2019.111456.

Yang, X., Klotzsche, A., Meles, G., Vereecken, H., van der Kruk, J., 2013. Improvements in crosshole GPR full-waveform inversion and application on data measured at the Boise Hydrogeophysics Research Site. J. Appl. Geophy. 99: 114-124. doi:10.1016/j.japp geo.2013.08.007.

Yilmaz, Ö., 2001. Seismic data analysis: Processing, inversion, and interpretation of seismic data. Society of exploration geophysicists.

Yolcubal, I., Brusseau, M.L., Artiola, J.F., Wierenga, P., Wilson, L.G., 2004. Environmental physical properties and processes. Environmental Monitoring and Characterization. Academic Press, Burlington, pp. 207-239. doi:10.1016/B978-012064477-3/50014-X.

Youngs, E.G., 1987. Estimating hydraulic conductivity values from ring infiltrometer measurements. J. Soil Sci. 38(4): 623-632. doi:10.1111/j.1365-2389.1987.tb021 59.x.

Yu, X., Drnevich V. P., 2004. Soil water content and dry density by time domain reflectometry. J. Geotech. Geoenviron. 130(9): 922-934. doi:10.1061/(ASCE)1090-0241(2004)130:9(922).

Yu, Y., Klotzsche, A., Weihermüller, L., Huisman, J.A., Vanderborght, J., Vereecken, H., van der Kruk, J., 2020. Measuring vertical soil water content profiles by combining horizontal borehole and dispersive surface ground penetrating radar data. Near Surf. Geophys. 18(3): 275-294. doi:10.1002/nsg.12099.

Yu, Y., Weihermüller, L., Klotzsche, A., Lärm, L., Vereecken, H., Huisman, J.A., 2021. Sequential and coupled inversion of horizontal borehole ground penetrating radar data to estimate soil hydraulic properties at the field scale. J. Hydrol. 596: 126010. doi:10.1016/j.j hydrol.2021.126010.

Zegelin, S.J., White, I., Jenkins, D.R., 1989. Improved field probes for soil water content and electrical conductivity measurement using time domain reflectometry. Water Resour. Res. 25(11): 2367-2376. doi:10.1029/WR025i011p02367.

Zhang, Z.F., Ward, A.L., Gee, G.W., 2003. Estimating soil hydraulic parameters of a field drainage experiment using inverse techniques. Vadose Zone J. 2(2): 201-211. doi:10.2136/v zj2003.2010.

Zhu, J., Mohanty, B.P., 2003. Effective hydraulic parameters for steady state vertical flow in heterogeneous soils. Water Resour. Res. 39(8). doi:10.1029/2002wr001831.

Zhu, Y., Shi, L., Yang, J., Wu, J., Mao, D., 2013. Coupling methodology and application of a fully integrated model for contaminant transport in the subsurface system. J. Hydrol. 501: 56-72. doi:10.1016/j.jhydrol.2013.07.038.

Zreda, M., Desilets, D., Ferré, T.P.A., Scott, R.L., 2008. Measuring soil moisture content non-invasively at intermediate spatial scale using cosmic-ray neutrons. Geophys. Res. Lett. 35(21). doi:10.1029/2008GL035655.

Zreda, M., Shuttleworth, W.J., Zeng, X., Zweck, C., Desilets, D., Franz, T., Rosolem, R., 2012. COSMOS: the cosmic-ray soil moisture observing system. Hydrol. Earth Syst. Sci. 16(11): 4079-4099. doi:10.5194/hess-16-4079-2012.

Zurmühl, T., 1994. Validierung konvektiv-dispersiver Modelle zur Berechnung des instationären Stofftransports in ungestörten Bodensäulen. Lehrstuhl für Bodenkunde und Bodengeographie der Univ. Bayreuth.

PUBLICATIONS LIST

1. **Yu, Y.,** Weihermüller, L., Klotzsche, A., Lärm, L., Vereecken, H., Huisman, J.A., 2021. Sequential and coupled inversion of horizontal borehole ground penetrating radar data to estimate soil hydraulic properties at the field scale. J. Hydrol. 126010. doi: 10.1016/j.jhydrol.2021.126010.

2. **Yu, Y.,** Klotzsche, A., Weihermüller, L., Huisman, J.A., Vanderborght, J., Vereecken, H., van der Kruk, J., 2020. Measuring vertical soil water content profiles by combining horizontal borehole and dispersive surface ground penetrating radar data. Near Surf. Geophys. 18(3): 275-294. doi:10.1002/nsg.12099.

3. **Yu, Y.,** Huisman, J.A., Klotzsche, A., Vereecken, H., Weihermüller, L., 2021, Coupled full waveform inversion of horizontal borehole ground penetrating radar data to estimate soil hydraulic parameters: a synthetic study, in preparation.

4. **Yu, Y.**, Klotzsche, A., Weihermüller, L., Huisman, J., Vanderborght, J., Vereecken, H., van der Kruk, J., 2019. Monitoring soil water content dynamics in a field-scale infiltration experiment by combining horizontal borehole and surface GPR, AGU Fall Meeting Abstracts, pp. NS21C-0833.

5. **Yu, Y.**, Xia, J., Cheng, F., 2016. A Synthetic study of dispersive GPR data due to multilayer waveguides, 7th International Conference on Environment and Engineering Geophysics & Summit Forum of Chinese Academy of Engineering on Engineering Science and Technology. Atlantis Press.